

**INVESTIGATING SELF-ASSEMBLY AND ANCHORING OF
SURFACTANTS AND NANOPARTICLES ON LIQUID CRYSTAL
NANODROPLETS BY MULTISCALE SIMULATIONS**

by

ZEYNEP SUMER

*A thesis submitted
in partial fulfilment of the requirements
for the degree of
DOCTOR OF PHILOSOPHY
in
CHEMICAL ENGINEERING*

UNIVERSITY COLLEGE LONDON

November 2020

I, Zeynep Sumer, confirm that the work presented in this thesis is my own. Where information has been derived from other sources, I confirm that this has been indicated in the thesis.

ACKNOWLEDGMENTS

I would like to start by expressing my gratitude to my supervisor Prof Alberto Striolo for his guidance. Without research group discussions and the opportunity to attend various conferences to share my research, this work would not be possible. I am thankful to Dr Stefan Guldin, particularly for his help in understanding of experimental phenomena and for the detailed answers to my questions whenever I had any.

The research shared in this thesis has moved to the next level with the help of contributors from different fields. For this reason, I am grateful to Prof Sally Day and Dr F. Anibal Fernandez from Electronic and Electrical Engineering Department at UCL. Additional thanks to Prof Cliff Jones from University of Leeds, and Dr Martin Lisal from for the Czech Academy of Sciences for fruitful discussions. I thank University College London Research Computing Platforms Support (Grace, Myriad, Legion) and the National Energy Resources Supercomputer Center (NERSC) for the generous allocations of computing time.

The current members, also alumni and visitors, of Molecular Thermodynamics group in UCL made the hard conditions of research much eased for me: special thanks to my colleagues Abeer Khedr, Anh Phan, Tai Bui, Tran Le, Maria Apostolopoulou, Sakiru Badmos, Francois Sicard, Dian Fan, Olivera Drecun, Azeezat Ali, Sakariya Hersi and Rossella Parisi. It was a pleasure to be a part of this group. I would also like to thank Dezhi Shen for discussions related with continuum mechanics calculations.

I thank Berna Sezgin Oztok, Deniz Kaya, Dilara Gulcin Caglayan, Elif Kocaman Tan, and Merve Tufan for being there for me, although I was far away most of the time for the last three years. Finally, many thanks to my family; I am indebted for their continuous support and care.

ABSTRACT

Liquid crystals (LCs) continue to receive significant attention due to their tunable order-disorder transitions. They are the foundation of many technological advancements such as displays, sensors, and other devices. Applications in which LCs are utilized build on the ability of controlling the orientation of mesogens with respect to a direction vector. To advance applications such as sensing and displays, it is required to detect and control, respectively, changes in LCs order due to external stimuli. To control LCs' order, it is possible to add amphiphiles to systems in which LC – solvent interfaces are present. One example of the latter approach is provided by the interface between thermotropic LCs and immiscible aqueous phases. Many researchers investigated how to tune the LC phases via external stimuli which take advantage of said interfaces, for example via the introduction of block copolymers or nanoparticles (NP) to LC-containing systems. Although the results are promising, many molecular-level mechanisms remain to be completely understood, including the anchoring strength, and effects due to confinement and temperature. The aim of this thesis is to computationally investigate how adsorption of different compounds such as surfactants and nanoparticles can be used to control LCs droplets' orientational order. For that purpose, coarse-grained molecular simulations were used. Firstly, in part for computational reasons, cylindrical LC assemblies were investigated. Then, to secure a stronger connection with practical devices, spherical LC droplets were considered. To overcome the limitations of coarse-grained simulation approaches, and to validate the results obtained at the nanometre-scale, the continuum-level Q-tensor approach was used. The latter has been shown to reproduce many experimental observables for bulk systems, and it allowed us to quantitatively analyse the defect structures inside LC droplets. The multiscale approach developed and implemented here, which allows us to investigate the properties of molecular aggregates at the shorter length scale, to macroscopic assemblies at the larger length scale, could provide a computational platform for future LC-based applications such as advanced biosensors that detect e.g., traces of viruses, bacteria, or air contaminants.

IMPACT STATEMENT

In this thesis the interactions of Liquid Crystal (LC) droplets with surfactants and nanoparticles (NP); and their emergent behaviour were investigated. A comprehensive multi-scale analysis of LC droplets that combines coarse-grained molecular simulations with continuum representations of the LC order through Q-tensor theory is conducted.

LCs have been used for the development of high-resolution visualization devices due to their unique optical properties. Their temperature-dependent orientational and positional order led to various applications, including liquid crystal displayer (LCD) screens, and biosensors. Because LCs preserve a crystalline order although they are in liquid phase under certain temperature, they are often called as *mesogens*, which are compounds in mesophase. Either in bulk, or geometrically confined, mesogens exhibit interesting chemical and physical properties that could lead to several innovations in product and processes. For future developments, it is observed that controlling the LCs confinement in the form of droplets is one of the major challenges. Due to the nature of the spherical confinement, LC droplets and nanodroplets should be treated differently than their bulk counterparts. Conclusions achieved by investigating LC mesogens in bulk, most probably will not apply in a spherical geometry. In addition, the smaller the droplets, the fuzzier the distinction between surface and bulk region within the droplets. This is the challenge faced by the development of applications such as polymer dispersed liquid crystals (PDLC), as well as others. LC droplets can be controlled and manipulated via electromagnetic, thermal, and chemical stimuli. Quantifying how LC droplets and nanodroplets respond to other chemicals is the fundamental mechanism responsible for highly sensitive biosensors.

Considering that PDLC and LC sensor applications typically employ LCs droplets, special attention is necessary to study LC mesogens under spherical confinement. Various experimental studies have identified the sensitivity level for different biological and chemical compounds, which is typically quantified in terms of nematic-to-isotropic transition, or vice versa. The small changes in LC droplets' internal structures, including the appearance of defects, remain inaccessible experimentally; such features can only be captured by computational studies for nm-size systems. However, atomistic and coarse-grained simulations, which are expected to provide

reliable information at all length scales, quickly become computationally prohibitive when the LC droplet size increases above 40 – 50 nm. At much larger length scales, calculations based on continuum mechanics yield results which positively correlate with experiments. The mesoscale region in between remains difficult to explore computationally, although a phenomenological correspondence between coarse-grained simulations and continuum studies has been demonstrated in this thesis, which could prove useful to develop accurate multiscale studies of LC droplets.

Pioneers of LC modelling have produced signature works using both molecular simulations and continuum mechanics. Almost exclusively, these works either qualitatively support selected experimental findings via Q-tensor theory, or provide molecular insights related to experimental observations via the implementation of atomistic simulations (Monte Carlo or molecular dynamics) or Gay – Berne coarse-grained potentials. The few available reports that use both Q-tensor and molecular simulations, focus on bulk behaviour or, at most, cylindrical confinement. The aim of this thesis is to fill the knowledge gap between nano and mesoscales, so that to provide an initial roadmap for the interpretation of experimental data obtained for LC droplets and nanodroplets.

ACHIEVEMENTS

PUBLICATIONS

1. Zeynep Sumer, F. Anibal Fernandez and Alberto Striolo. *Engineered liquid crystal nano droplets: insights from multi-scale simulations*. *Nanoscale*, 2020, 12, 20211-20219.
2. Zeynep Sumer and Alberto Striolo. *Nanoparticles shape-specific emergent behaviour on liquid crystal droplets*. *Molecular Systems Design & Engineering*, 2020, 5, 449-460. Our artwork was accepted as **main cover** after a successful review process for the February 2020 issue of the journal. This paper was also been selected for the MSDE **Recent HOT Articles 2020**.
3. Zeynep Sumer and Alberto Striolo. *Effects of droplet size and surfactants on anchoring in liquid crystal nanodroplets*. *Soft Matter*, 2019, 15, 3914-3922.
4. Zeynep Sumer and Alberto Striolo. *Manipulating molecular order in nematic liquid crystal capillary bridges via surfactant adsorption: guiding principles from dissipative particle dynamics simulations*. *Physical Chemistry Chemical Physics*, 2018, 20, 30514-30524.

PRESENTATIONS (*Highlights*)

1. Soft Matter Physics Seminar, University of Leeds, UK, 21 Oct 2020 (virtual). **Invited speaker**. Title: *Investigating Liquid Crystal Nano Droplets from a Molecular Perspective*.
2. 2019 AIChE Annual Meeting, Orlando, FL, US, 10-15 Nov 19. Title: *Modelling External Stimuli on Liquid Crystal Assemblies by Surfactants and Nanoparticles at Nanoscale*.
3. International Conference on Properties and Phase Equilibria for Product and Process Design, Vancouver, Canada, 12-16 May 2019. Title: *Manipulating Liquid Crystals Using Surfactants: A Molecular Perspective*. (poster)
4. British Liquid Crystal Society 2019 Annual Conference, Leeds, UK, 15-17 Apr 2019. Title: *Manipulating Liquid Crystals Using Surfactants: A Molecular Perspective*.
5. CECAM Workshop, Collective Behavior of Soft and Active Matter Under Confinement, Mainz, Germany, 24-26 Sep 2018. Title: *Surfactant Adsorption and Manipulating Liquid Crystal Droplets: A Dissipative Particle Dynamics Study*.

TABLE OF CONTENTS

Abstract	4
Impact Statement	5
Achievements	7
Chapter 1 – Introduction	13
Chapter 2 – Literature Review	19
Chapter 3 – Computational Methods and Algorithms	25
3.1 Dissipative Particle Dynamics (DPD).....	25
3.2 Molecular Modelling.....	27
3.3 Calculation of Orientational Order.....	30
3.4 Q-Tensor Simulations and Defects	32
Chapter 4 – Cylindrical Formations of LCs and Their Interactions with Surfactants .	36
4.1 Bulk Liquid Crystals	39
4.2 LC Bridges in Water.....	40
4.3 Surfactant Adsorption and Orientational Order.....	41
4.4 Effect of Surfactant Surface Density.....	43
4.5 Effect of LC – Surfactant Interactions	45
4.6 Orientation of LCs with respect to Surfactant Density and Radius.....	47
Chapter 5 – Spherical Confinement of LCs and Their Interactions with Surfactants	52
5.1 Nematicity in LC Droplets	52
5.2 Surfactants’ Adsorption on LC Droplets.....	56
5.3 Effect of Surfactant Concentration	59
5.4 Coalescence of Multiple Surfactant-Covered Droplets	60
Chapter 6 – Nanoparticle Self-Assembly on LC Droplets	63
6.1 Self-Assembly of Small Nanoparticles	65
6.1.1 Spheroid Nanoparticles	67
6.1.2 Spherical Nanoparticles.....	68
6.1.3 Nanoparticles with Facets	69
6.1.4 Branched Nanoparticles	71
6.2 NPs’ Effects on LC Mesogens’ Self-Assembly.....	72
6.3 Effect of NP Size.....	75
6.3.1 Spheroids and Spheres	77
6.3.2 Cylinders and Cubes	79

6.3.3	Branched NPs	80
	Chapter 7 – LC Droplets Under Extreme Confinement.....	81
7.1	Orientational Order Analysis	85
7.2	Total Energy and Energy Density	90
7.3	Effect of Droplet Size in Q-Tensor Calculations.....	92
	Chapter 8 – Summary and Future Work	95
8.1	Summary of Achievements	95
8.2	Future Work	98
	Appendices.....	101
	Appendix A – Supplementary for Nanodroplet Simulations	101
	Appendix B – Supplementary for Nanoparticle Simulations.....	102
	Appendix C – Supplementary for Q-Tensor Simulations	105
	C.I. Thermotropic Parameter Change.....	105
	C.II. Supplementary for Chapter 7.1	107
	Bibliography.....	111

LIST OF FIGURES AND TABLES

Figure 1.1. Liquid Crystal (LC) phases	14
Figure 3.2.1. Atomistic and coarse-grained models of a common LC molecule (5CB).	28
Figure 3.2.2. (a) Molecular models of water, liquid crystal, and surfactants. Representations of (b) a water bead and (c) surfactants with head to tail ratio, $S_{\text{head}}/S_{\text{tail}} = 7/3, 5/5$ and $3/7$, respectively.	29
Figure 3.2.3. Sizes and volumes of the small nanoparticles (NPs) modelled in this work. Left to right: disc, ellipse, sphere, rod, cube and star shaped NPs.	30
Figure 3.4.1. Defect structures, defect cores (blue) and their strength (m).	34
Figure 4.1. Volume change of the system that was simulated for additional $0.14 \mu\text{s}$ in NPT ensemble.	37
Figure 4.1.1. Orientational order parameter (S) of bulk LC vs. scaled temperature and snapshots of LCs in crystalline (C), nematic (N) and isotropic (I) phases. Line between data points is guide to eye.	39
Figure 4.2.1. (a) Orientation of LC molecules in water without any surfactant added at $0.7 k_{\text{B}}\text{T}$ ($S = 0.70$) and (b) LCs with water beads removed. (c) and (d) Schematic representation of LCs that are located at the core ($r \leq 5 r_{\text{c}}$) and outer ($r > 5 r_{\text{c}}$) region of cylinder.	40
Figure 4.3.1. Configurations of LC and 1000 surfactant molecules with (a) 3 bead (b) 5 bead and (c) 7 bead-long tail-groups at $0.7 k_{\text{B}}\text{T}$ The change in orientation in LCs is due to interactions with surfactants with (d) 3 bead (e) 5 bead and (f) 7 bead-long tail. LCs that are located in the core of cylindrical radius ($r \leq 5 r_{\text{c}}$) are shown in pink, the rest in yellow. Water beads are not shown for clarity.	42
Figure 4.4.1. Configurations of LC and 1500 surfactant molecules with (a) 3 bead, (b) 5 bead, and (c) 7 bead-long tail-groups at $0.7 k_{\text{B}}\text{T}$. Orientation change in LCs due to interactions with surfactants with (d) 3 bead, (e) 5 bead, and (f) 7 bead-long tail-groups. LCs located in the core of cylindrical radius ($r \leq 5 r_{\text{c}}$) are shown in pink, the rest in yellow. Water beads are not shown for clarity.	44
Figure 4.5.1. Configurations of LCs and 1000 surfactant molecules with (a) 3 beads, (b) 5 beads, and (c) 7 bead-long tail-groups at $0.7 k_{\text{B}}\text{T}$ with to $\alpha_{\text{LC-Stail}} = 20$. Orientation change in LCs due to interactions with surfactants with (d) 3 beads, (e) 5 beads, and (f) 7 bead-long tail-groups. LCs located in the core of cylindrical radius ($r \leq 5 r_{\text{c}}$) are shown in pink, the rest in yellow. Water beads are not shown for clarity.	46
Figure 4.6.1. Number of LC molecules vs. their order parameter with (a) 1000 surfactant molecules where $\alpha_{\text{LC-Stail}} = 25$; (b) 1500 surfactant molecules where $\alpha_{\text{LC-Stail}} = 25$; and (c) 1000 surfactant molecules where $\alpha_{\text{LC-Stail}} = 20$. The legend is the same for (a), (b) and (c).	48
Figure 4.6.2. Orientational order of LCs (lines with symbols) and surfactant density (dashed lines) with respect to their distance to cylindrical axis ($r = 0$) with (a) 1000 surfactant molecules where $\alpha_{\text{LC-Stail}} = 25$; (b) 1500 surfactant molecules where $\alpha_{\text{LC-Stail}} = 25$; and (c) 1000 surfactant molecules where $\alpha_{\text{LC-Stail}} = 20$. The legend is the same for (a), (b) and (c).	49
Figure 4.6.3. (Left) Configurations of LC and 1000 surfactant molecules with $S_{\text{head}}/S_{\text{tail}} =$ (a) $3/5$ (b) $7/5$ and (c) $5/7$ at $0.7 k_{\text{B}}\text{T}$. The change in orientation in LCs is due to interactions with surfactants with $S_{\text{head}}/S_{\text{tail}} =$ (d) $3/5$, (e) $7/5$, and (f) $5/7$. LCs that are located in the core of cylindrical radius ($r \leq 5 r_{\text{c}}$) are shown in pink, the rest in yellow. (Right) Orientational order as a function of position.	50
Figure 5.1.1. LC droplets with radii of (a) 4.75, (b) 7.43, (c) 10.42, (d) 12.95, and (e) 16.08 nm, respectively, dispersed in water at $0.6 k_{\text{B}}\text{T}$. Water beads are not shown for clarity. Rods are colour-coded by their order parameter, calculated with respect to the directional axis.	54
Figure 5.1.2. (a) Orientational order parameters (S) of spherical LC droplets with respect to temperature. (b) Asphericity of LC droplets with respect to temperature. Error bars are obtained as one standard deviation from the average of values derived from 100 frames for each data point. Legend is the same for both (a) and (b).	55
Figure 5.2.1. (Left) Equilibrated simulation snapshots for LC nanodroplets of radius $13.6 r_{\text{c}}$ (10.42 nm) covered with low concentration of surfactants. From left to right, the surfactants have tail-groups of 3, 5, and 7 beads, respectively. The simulations are conducted at $T = 0.62 k_{\text{B}}\text{T}$. In all cases, water beads are not shown for clarity. In the top panels, only LC mesogens are shown, also for clarity. (Right) Orientational order of LC molecules shown with respect to their distance to the core of the droplet for every $3 r_{\text{c}}$	57
Figure 5.3.1. (a) LC nanodroplet of radius $13.6 r_{\text{c}}$ (10.42 nm) covered with high concentration of surfactants whose tail-group is of 7 beads. No water beads are shown for clarity. (b) Same as (a), but	

without surfactants, for clarity. LC molecules are colour-coded with respect to their order parameter. The simulations were conducted at 0.62 k _B T.	59
Figure 5.4.1. Eight LC nanodroplets, each covered with (a)1000 and (b)1500 surfactant molecules with 7 bead-long tails at (left) 0 μs and (right) 0.745 μs. On the far right, an enlargement of the cross-section of largest droplet obtained, (a)~24 r _C radius and (b)~19 r _C radius.	61
Figure 6.1. NPs simulated in this work. Homogeneous NPs are described by beads of a single type (type I NPs, top row), while Janus NPs are composed of two bead types. For several NPs it is possible to generate Janus NPs of two different structures (type II and type III, respectively, in middle and bottom row Refer to the text for details regarding the DPD interaction parameters implemented.	64
Figure 6.1.1. Left: Density profiles of NP beads with respect to distance from the droplet core. Lines in graph indicate the interface, located at radial distances in the range between 13.6 – 15.6 r _C . Right: Corresponding snapshots of LC droplets. Coordinates for the various systems summarised in this figure were provided in Appendix B.	66
Figure 6.2.1. Probability distributions of LC mesogens with respect to their locations and order parameters, for pristine LC droplets and for LC droplets that were exposed to group I NPs, as shown in Figure 6.1.1. Similar results for group II and III NPs are provided in Appendix B.	74
Figure 6.2.2. (a) Orientational orders (purple) and asphericity (orange) and (b) map of LCs on droplets colour-coded by their order parameter that were exposed to Group I nanoparticles. Group II and III are provided in Appendix B.	75
Figure 6.3.1. Schematic representation of the algorithm implemented to test whether the DPD simulations discussed below for large NPs adsorbed on LC droplets had reached equilibrium. LC molecules are colour-coded by their order parameter. Further details are provided in the Appendix B.	76
Figure 6.3.2. Simulation snapshots of droplets with large particles, colour-coded LC molecules with respect to order parameters. Each panel title represents the corresponding NP in the notation shown in Figure 6.1. Legend is the same with Figure 6.3.1 for order parameters.	77
Figure 7.1. Homeotropic and planar degenerate anchoring surface distributions for (a) Homeotropic Centre (HC), (b) Planar Centre (PC) and (c) Two-Sided (TS) droplets. The percent ratios represent the amount of surface on which strong planar degenerate anchoring is enforced on the simulated LC droplets.	82
Figure 7.2. (a) Initial configuration of DPD simulations, cut through to visualise the LC mesogens inside the spherical shell. Red, yellow and light grey beads represent the inert beads, tip and body of LC molecules, respectively. (b) Schematic representation of mesh structure used in Q-tensor simulations. Both panels are for PC type droplet with 40% planar degenerate anchoring on the surface, chosen as an example. (c) DPD parameters used in this chapter.	83
Figure 7.3. (Top) Three droplet shells with different anchoring surfaces, homeotropic (blue) and planar degenerate (orange). (Middle) Colour-coded LC molecules with respect to S _R (up) and S _U (down). (Bottom) Snapshots of simulations performed by the finite-element method with emphasis on defect structures, the images show surfaces of constant order for a low value of S (see Chapter 3 for details).	84
Figure 7.1.1. Orientational order as quantified by DPD simulations (S _U and S _R) and Q-tensor calculations for (a) HC (homeotropic centre), (b) PC (planar centre), and (c) TS (two-sided) type droplets. (d) Comparison of total energy (full line with square) and total enthalpy (dashed line with circle) of all droplets for DPD results; SH and SP represent fully strong homeotropic and fully strong planar degenerate anchoring, respectively.	88
Figure 7.2.1. (a) Elastic and (b) thermotropic energy densities of droplets from Q-tensor calculations for HC (homeotropic centre), PC (planar centre) and TS (two-sided) type droplets. SH and SP represents fully strong homeotropic and fully strong planar degenerate anchoring, respectively. Legend is the same for all graphs. (c) Comparison of energy densities in Q-tensor and DPD calculations. Dashed line is the reference for y = x.	91
Figure 7.3.1. (a) Total energy densities for 60% HC, PC and TS type droplets with respect to droplet size. (b) 60% HC, (c) 60% PC and (d) 60% TS type droplets with defect regions highlighted (left) and color-coded by order parameter (right). For (b), (c) & (d), top rows represent 0.1 μm droplets and bottom rows represent 1.0 μm droplets. Legend in (b) is the same for (c) and (d).	92

Figure A. 1. Snapshot of the simulation conducted at 1.0 $k_B T$ where repulsion coefficient between water/LC beads was $50 k_B T/r$. Orientational order (S) was calculated as 0.01 ± 0.01	101
Figure A. 2. Snapshot of the simulation conducted at 0.62 $k_B T$ where repulsion coefficient between water/LC beads was $30 k_B T/r$	101
Figure B. 1. Left: Density profiles of NP beads with respect to distance from the oil droplet core. Lines in graph indicate the area between 13.6 – 15.6 r_c radii. Right: Corresponding snapshots of oil droplets.	102
Figure B. 2. Probability distributions of LC mesogens with respect to their locations and second order tensors, for droplets that were exposed to Group II and Group III nanoparticles that were described in Chapter 6.	103
Figure B. 3. (top) Orientational orders (purple) and asphericity (orange) and (bottom) map of LCs on droplets color-coded by their order parameter that were exposed to Group II and Group III nanoparticles.	104
Figure B. 4. Temperature oscillation during the manipulation of the particles. Graph contains all 10 Janus particles.	104
Figure C. 1. (a) Droplets selected for thermotropic coefficient analysis. Orientational order parameters (S) for all droplets simulated based on parameters in (b) Table C.1 and (c) Table 3.4.1. For the colour-coding see main content.....	106
Figure C. 2. Snapshots of simulations by finite-element method with emphasis on defect structures, the images show surfaces of constant order for a low value of S . (top) Calculations with thermotropic parameter $A = 0$, (bottom) $A = -1.27 \times 10^6$	106
Table 3.4.1. Parameters for the Q-tensor calculations.	33
Table 4.1. Repulsion coefficients (α_{ij}) used in the simulations in $k_B T/r_c$ units.....	37
Table 4.2. Compositions of simulated systems with (a) 1000 surfactant molecules where $\alpha_{LC-Stail} = 25$; (b) 1500 surfactant molecules where $\alpha_{LC-Stail} = 25$; and (c) 1000 surfactant molecules where $\alpha_{LC-Stail} = 20$	38
Table C. 1. Parameters for the Q-tensor calculations implemented in Appendix C.	105
Table C. 2. Simulation results obtained for the total energy densities of the droplets. Results shown here were divided into droplet volume.....	107
Table C. 3. Droplets with homeotropic-centre (HC), with respect to their surface anchoring conditions, defects obtained by Q-tensor calculations (0.1 μm diameter), and colour-coded LC molecules by DPD simulations with respect to S_U and S_R type orientational orders (30 nm diameter). For the colour-coding see main text.....	108
Table C. 4. Droplets with planar-centre (PC), with respect to their surface anchoring conditions, defects obtained by Q-tensor calculations (0.1 μm diameter), and colour-coded LC molecules by DPD simulations with respect to S_U and S_R type orientational orders (30 nm diameter). For the colour-coding see main text.....	109
Table C. 5. Droplets with two-sided surfaces (TS), with respect to their surface anchoring conditions, defects obtained by Q-tensor calculations (0.1 μm diameter), and colour-coded LC molecules by DPD simulations with respect to S_U and S_R type orientational orders (30 nm diameter). For the colour-coding see main text.....	110

CHAPTER 1

INTRODUCTION

The spontaneous organization of matter has yet to be fully understood, despite the fact that controlling the assembly of materials that vary in size and shape over multiple length scales could enable advancements in science and technology. Among other self-assembling structures, nanoparticles and liquid crystals could be used, e.g., in optical devices, catalysts and pharmaceuticals.^{1, 2} In these and other futuristic applications, such nano-sized elements could provide the building blocks for supra-molecular engineered materials.³

Liquid crystals (LCs) continue to receive significant attention due to their unique optical properties and tunable orientational order. Since the 19th century, there has been a tremendous effort to understand LC behaviour.^{4, 5} Liquid crystalline state is a mesophase, between crystalline solids and isotropic liquids. In general terms, LCs are classified in two categories: lyotropic and thermotropic. At high temperatures, thermotropic LCs exhibit isotropic liquid phases, with no positional or orientational order. As the temperature decreases, the phase changes from isotropic to nematic. Schematic representation of LC phases are provided in Figure 1.1. As their phase shifts from isotropic to nematic, their optical signature as observed via, e.g., polarized microscopes, changes.^{6, 7} The nematic phase is the most common phase of LCs, in which LCs exhibit an orientational order. As the temperature is lowered further, LCs yield smectic phases with both orientational and positional ordering; the solid crystalline phase is obtained at very low temperatures.^{7, 8} They are utilized in many technological advancements due to their phase transition and optical properties such as displays, sensors, and other devices.^{8, 9} Applications in which LCs are utilized build on the ability of controlling the orientation of mesogens with respect to a direction

vector. To advance applications such as sensing and displays, it is required to detect and control, respectively, changes in LCs order due to external stimuli.

To further develop advanced applications, it is desirable to understand how defects propagate or emerge in LC structures as a function of the mesogens anchoring, which could be altered using surfactants, polymer encapsulation, or other techniques, as well as of the degree of confinement (e.g., size of the LC droplet). Anchoring identifies the interactions on the interface between confined LC molecules and the surrounding species. Homeotropic anchoring refers to LCs that are aligned perpendicular to the interface, and planar anchoring refers to LCs that are aligned parallel to the interface. Type and strength of the anchoring has a cumulative effect on droplets from surface to the core, LCs located in the bulk of a droplet also change orientation with respect to the neighbouring LC molecules. If all the LCs within the droplet align perpendicular to the surface, in homeotropic anchoring conditions, radial droplet will occur, with a point defect in the core. For planar degenerate anchoring (degenerate due to spherical boundaries), a bipolar droplet will be obtained with the two point defects located in two opposite sides of the droplet.

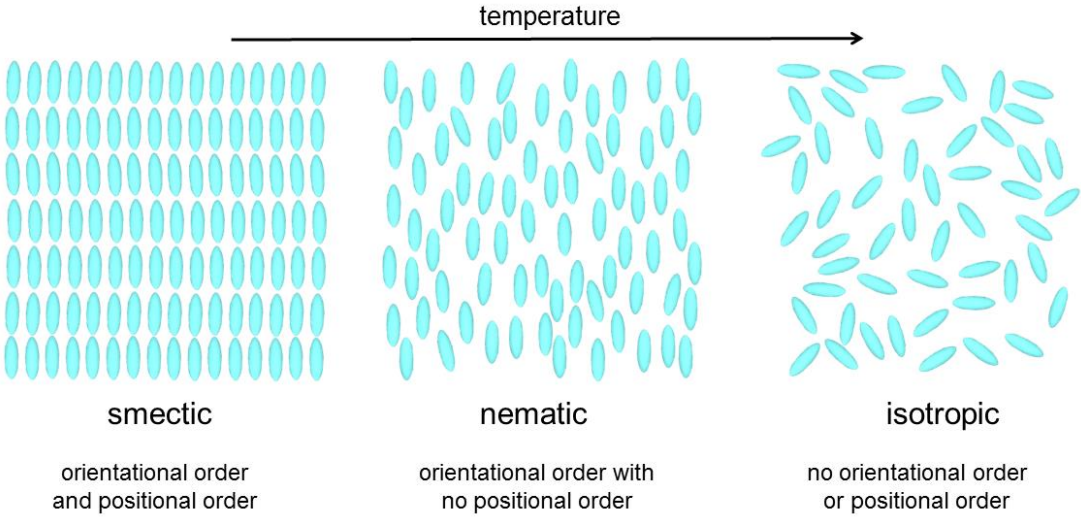


Figure 1.1. Liquid Crystal (LC) phases

Devices have in fact been developed using encapsulated LC droplets, where the encapsulating shell is capable of changing the alignment in LC surface anchoring, e.g., responding to reactions with different substances.¹⁰⁻¹² To control LCs' order it is

possible to use light,¹³⁻¹⁵ temperature,¹⁶ electric¹⁷ or magnetic¹⁸ fields, or adding amphiphiles to systems in which LC – solvent interfaces are present.^{19, 20} One example of the latter approach is provided by the interface between thermotropic LCs and immiscible aqueous phases.²¹ Many researchers investigated how to tune the LC phases via external stimuli; such as and the introduction of, e.g., block copolymers²² or nanoparticles²³ to LC-containing systems.

So far, LC technology is mostly guided by experimental results, leading to a gap in proper optimization processes. The hurdle is due, in part, to incommensurate observations between experiments, which probe length scales of several hundred micrometres, and molecular simulations, which probe events that occur at the nanometre scale. Although not equally mature as experiments, theoretical modelling and calculations have been extremely helpful to understand the relevant phenomena.²⁴ The cumulative effect due to system changes, such as the imposition of electric fields or changes in temperature, is generally tractable using computational approaches. On the other hand, a reliable model able to describe the localized effect due to an external substance is currently missing, in part because LC confinement occurs at length scales that are smaller than those probed by continuum models, and larger than those typically probed by molecular and coarse-grained simulations. It would therefore be desirable to connect molecular or coarse-grained simulations, seamlessly, to Q-tensor results to develop accurate models across multiple length scales. Yet, many molecular-level mechanisms remain to be completely understood, especially the interactions between LCs and chemicals, the anchoring strength, and how these properties are affected by changes in temperature. Confinement could potentially yield an additional tuning handle to complement changes in thermodynamics conditions.^{25, 26} For such systems, one fundamental question of wide interest concerns how mesogens anchor at the LC – water interface, in the presence or absence of stabilizing chemicals.

Among other theoretical approaches, the Landau – de Gennes continuum theory,^{27, 28} which describes the behaviour of the LC through an order tensor and considers order variations, is often employed to study LC structures because it can deal with larger length scales than molecular simulations. Although the chemical features of the LC mesogens are sometimes overlooked in the continuum models, as they are only considered through the macroscopic material properties, the approach describes, for example, how the energy densities associated to different elastic

distortions change as the anchoring conditions change. Good agreement with macroscopic experiments are often reported.²⁹⁻³¹ When the degree of confinement is high, for example in LC droplets of nanometre scale diameter, it is however expected that the chemical features of the mesogens play an important role. To assess such features, complementary molecular simulations are necessary.

Previous molecular simulation studies were useful to elucidate the mechanism of supramolecular ordering with respect to change in size or anchoring on the surface of LC droplets,^{26, 32} or in bulk nematic phases.³³⁻³⁶ Other studies focused on the molecular orientation as a function of temperature and changes in the interaction with homogeneous shells surrounding the LC droplets.^{37, 38} Despite these advancements, the length scale in between molecular simulations and continuum models remains little explored by available computational approaches, although future technologies are likely to require underpinning understanding at the mesoscale. For LC droplets of 200 – 500 nm radius, continuum calculations yield very detailed insights for the mesogens collective properties.³⁹ However, it lacks the information on the behaviour of individual molecules and they cannot be overlooked particularly at nm length scales. Effect of inter- and intra-molecular interactions on surface anchoring and elastic energy can be elucidated by simulations that take molecular identity into account.

Because surfactants are often used to stabilise dispersions, implementation of methods in this thesis started with the investigation of surfactant – LC interactions. Simulation boxes composed of LC molecules in a cylindrical confinement were built, and the effect of surfactants' molecular structure to the response of LCs were investigated. The results showed that varying the number of hydrophilic coils and hydrophobic rods in such a model surfactant can largely affect LCs' anchoring alongside surfactant tail – LC interactions. Those results depend on the internal elasticity, which tends to preferentially align the cumulative direction of LCs along the axis of the cylinder. Thus, it is expected that the results on a cylindrical bridge are significantly different than those on a spherical LC droplet. LC molecules assembled in spherical nanodroplets were systematically studied. The effect of temperature and surfactants on the alignment of the LC molecules was quantified.

The study continued with investigating the coalescence of LC droplets immersed in water, in the presence of surfactants. Surfactants were not effective at

stabilising LC droplet emulsions. This is due to the tendency of the surfactants to accumulate at the droplet *boojums*. Boojums are the surface defects that are observed at the two *poles* of spherical droplets, for a strong planar degenerate anchoring condition that endorses tangential boundary.⁴⁰ Instead of uniformly covering the LC droplets, surfactants prefer to be positioned in these low free energy spots.⁴¹ However, large enough densities of surfactants can in some cases delay LC droplets coalescence.

Once the results of surfactant interactions were obtained, nanoparticles self-assembly on LC nanodroplets was investigated. A systematic study was conducted on LC nanodroplets on which NPs of different size, shape and chemistry are adsorbed, with particular emphasis on self-assembly. To interpret the results in light of literature observations, it is beneficial to classify colloidal particles based on anisotropy. Thus, NPs are categorically identified as spheroids (discs and ellipses), spheres, rods, faceted polyhedra, branched structures and colloidal molecules; patterned or not.⁴² Other criteria can be used to classify nanomaterials, e.g., anisotropy dimensions, patch size, curvature radius and so forth.⁴³ Six shapes were considered: discs, ellipses, spheres, cylinders, cubes, and stars. For each NP shape, both homogeneous and Janus particles were simulated,⁴⁴ given the increasing importance of patterned particles in the field.

Particles' self-assembly on oil nanodroplets is also considered for comparison. Results revealed that the mesogens can direct the assembly of the NPs. Due to their molecular structure, LCs act as a template for NPs. This allows NPs to self-assemble and create ordered structures on the droplet surface, although form of those structures strongly depend on other parameters such as the size and shape of NPs. In some cases, strong evidence of emergent behaviour is observed, depending on entropic forces that arise because of shape and patchiness of the nanoparticles. Quantification of the orientational order within the LC nanodroplets suggests that the self-assembly of the LC mesogens does not significantly change upon nanoparticles adsorption. These simulations clearly suggest an interplay between nanoparticles size, shape, and chemical composition upon their self-assembly on LC nanodroplets.

The LC ordered structure is strongly dependent on the molecular environment: how neighbouring molecules are aligned, or how the interfacial conditions change. The

anchoring strength at interfaces is known to dominate the behaviour of LC molecules. In a LC droplet with, for example, homeotropic anchoring with respect to the surroundings, adsorption of an analyte that promotes planar degenerate anchoring could create a surface defect, which could propagate through the droplet. To learn how pronounced these defects are, LC droplets confined within patchy shells were investigated. Two different surfaces were defined to promote strong homeotropic anchoring and strong planar degenerate anchoring, respectively. The LC behaviour within the nanoscale droplets was identified using a multi-scale simulation approach. Results for the largest droplet are consistent with those available in the literature, suggesting that the extension to smaller droplets presented here is likely realistic, and therefore can be helpful for innovations in which device intensification could be achieved using LC nanodroplets. The results could be helpful for the design of new sensors and for the directed self-assembly of advanced materials.

CHAPTER 2

LITERATURE REVIEW

Anchoring between LCs and other molecules in aqueous media can be used to manipulate the direction profile of liquid crystals (LC). LCs provide the foundation for mature electronics applications,⁴⁵ as well as for putative applications as gas sensing,⁴⁶ ⁴⁷ optical detection of protein binding,⁴⁸ bacteria and viruses.⁴⁹ and so forth.^{50, 51} Both experimental and computational studies investigated how the transition from planar to homeotropic orientation takes place by adding surfactants and other chemicals.

Haseloh et al. conducted dispersion polymerization experiments and found that surface anchoring is strongly dependent on the type of the mesogens and stabilizers.⁵² Amundson and Srinivasarao reported that the appropriate choice of polymer side groups in polymer-dispersed liquid crystal (PDLC) films enables to control anchoring without using additives.⁵³ Their results also show that the anchoring transition temperature decreases as the chain length decreases.

LCs' aggregates such as spherical droplets^{32, 49, 54-59}, flat surfaces^{21, 48, 53, 60-63} or cylindrical formations (capillaries and bridges)⁶⁴⁻⁶⁸ have been investigated. Kim et al. quantified optical, structural and topological features of tetrapodes assembled in flat layers, round capillaries and spherical droplets; the results for round capillaries revealed different textures depending on the inner diameter and system temperature.⁶⁶ In the experimental observations, two tubes having 50 μm and 150 μm inner diameter were used; it was reported that LCs within narrow capillary exhibit defects below their transition temperature, whereas LCs within the wider capillary preserve smooth texture. Williams et al., investigated capillary tubes filled with nematic LCs to study topological singularities, and reported that orientation of LC molecules is sensitive to

surface conditions.⁶⁹ The same group also demonstrated how to tune nematic director fields using surface-alignment agents in cylindrical capillary tubes.⁷⁰ It was found that the minimum energy corresponds to a nematic phase with perpendicular anchoring, with the LCs at the core of the cylindrical structure showing orientation parallel to the cylinder axis.⁷¹ Using experiments⁷² and theoretical calculations,⁷³ Meyer showed that external stimuli can affect the topological singularity. Of note, theoretical calculations such as those reported by Meyer are based on continuum mechanics and are effective in identifying macroscopic properties of matter; on the other hand, molecular simulations can provide complimentary information, as they allow investigators to probe how the structure and dynamics of individual molecules depend on their interactions with the surroundings.

Busch et al. concluded that a thermal-history independent phase behaviour of ferroelectric LC 2MBOCBC can be achieved by using polymer coated walls in cylindrical nanopores.⁷⁴ The pioneering studies concerning nematic LC alignment in cylindrical structures focused on homeotropic anchoring, and defined the escaped radial structure (ER).⁷⁵ ER is the shift of direction vector from parallel to perpendicular with respect to the cylindrical axis due to presence of external structures, such as a cylindrical confining wall or surface agents.⁷⁰ Ondris-Crawford et al. showed that the strength of interactions, i.e., surface coupling, between the cavity wall and the LC molecules increases with the length of LC molecules.⁷⁵ Ellis et al. investigated topological defects on waist-like and barrel-like bridges with respect to their aspect ratios.⁶⁵ They concluded that the aspect ratio determines ring and point defects. Their observations elucidated the role of shape and elasticity in dictating the LC structure in confined homeotropic nematic phases.

Alino et al. used polyethylene imine-coated LCs to detect proteins such as immunoglobulin G (IgG) and human serum albumin (HSA).⁵⁴ The proteins were detected by a transition of LC order in droplets from radial to bipolar. These groups reported that to detect smaller proteins it was necessary to reach higher protein concentrations compared to those at which larger proteins were detected. Specifically, because HSA is smaller than IgG, the radial-to-bipolar LCs transition was observed at 100 $\mu\text{g}/\text{mL}$ for HSA, but only at 50 $\mu\text{g}/\text{mL}$ for IgG. Wang et al. studied the configuration of LC droplets in inhomogeneous interfacial environments,⁵⁹ as they created Janus-like LC droplets by sedimentation at the aqueous-glycerol interface. In a previous study, the same

group reported on the effect of surfactants on the orientations of TL205 LCs (a mixture composed of cyclohexane-fluorinated biphenyls and fluorinated terphenyls) and 5CB LCs (4-pentyl-4'-cyanobiphenyl). The surfactants used included sodium dodecyl sulfate (SDS), linear dodecanesulfonate (LDS), linear dodecylbenzenesulfonate (L-DBS), and branched dodecylbenzenesulfonate (BR-DBS).²¹ While SDS, LDS and L-DBS triggered a planar-to-homeotropic transition for TL205, BR-DBS did not affect LCs orientation, and planar anchoring was reported at all BR-DBS concentrations. Wang et al. concluded that the molecular structure of the surfactants affects the anchoring of LCs, with interactions between surfactant tails and LCs dictating the orientational order. Wang et al. also reported that increasing LDS concentration leads to tail-mesogen interactions that favour homeotropic anchoring of both TL205 and 5CB due to an increase in interfacial surfactant density.

Sivakumar and coworkers⁴⁹ quantified the ability of LC droplets to detect three bacteria (*Escherichia coli*, *Bacillus subtilis*, and *Micrococcus luteus*) and two viruses (M13 helper phage and A/NWS/Tokyo/67). Detection depended on the ability of bacteria or viruses to change the order within LC droplets. Bera and Fang documented bipolar-to-radial configuration changes in 5CB LC droplets due to charged macromolecules, namely poly(amidoamine) PAMAM dendrimers and poly(styrenesulfonate) PSS. The bipolar-to-radial transition was affected by the macromolecules concentration, and also by size and number of LC droplets.⁷⁶ Miller and Abbott also reported on the size-dependency of LC ordering transitions using bacterial lipopolysaccharide endotoxin.⁷⁷

Researchers have also focused on identifying the molecular mechanisms responsible for changes in LCs order, in an effort to quantify the properties of LC-nanoparticle preparations.⁷⁸ Many have documented how nanoparticles (NPs) can show various degrees of self-assembly, depending on the particles morphology and on the system thermodynamic conditions.^{43, 79-85} Bulk NPs self-assembly has been investigated,⁸⁶⁻⁸⁸ as well as NPs self-assembly onto interfaces.⁸⁹⁻⁹³ Kumacheva and co-workers investigated the morphogenesis of LC droplets at increasing particle content within cholesteric (Ch) LC droplets doped with cellulose nanocrystals (CNC).⁹⁴ The results suggested that Ch-CNC droplets affect the particle alignment, and vice-versa. The size dependency of the results was also discussed.⁹⁵ De Pablo and co-workers reported that small NPs do not manifest a preferred adsorption site on LC

droplets, while large NPs prefer boojums, and therefore act as attractive wells for the NPs.⁹⁶ Defects are inevitable on LC droplets, and, because such defects could yield natural templates for smaller molecules or crystals such as copolymers or particles to adsorb on, they might be useful for developing future technological applications. Others considered LC-in-LC colloids by utilizing droplets of cholesteric CNC phases,⁹⁷ or hybrid colloidal fluids of biaxial phases.⁹⁸

In experimental works, LC droplets vary in size: while emulsion studies focus on LC droplets of 4 – 8 μm size,^{26, 49, 57} or as large as 40 – 60 μm ,^{54, 59, 99} polymer-dispersed LC (PDLC) droplets can have size as low as 250 – 650 nm,¹⁰⁰ and in some cases even 20 nm.¹⁰¹ It is known that different size droplets could yield different LC ordering under similar conditions.¹⁰² Gupta and co-workers stated that as the droplet size decreases from 3 μm to 700 nm, droplet order changes from bipolar to radial, respectively, and characterization was not possible for smaller droplets.¹⁰² Simulations could perhaps help predict order in such nm-size LC droplets, knowing that there already exists some qualitative correlation between experiments and simulations in nm scale as briefly discussed in Introduction.

Our understanding of LCs structures builds from continuum theoretical calculations,^{73, 103} which can identify driving forces and general guiding principles. Complementarily to such analysis, computational modelling and simulations, at the molecular scale, offer the opportunity of revealing how the details of the molecular compounds in LC-containing systems could affect macroscopic observables. Most computational studies in the literature focus on bulk LCs properties,^{104, 105} LC – solvent flat interfaces,¹⁰⁶ LCs self-assembled aggregates,¹⁰⁷ or mixtures of LCs and other compounds forced to maintain spherical shapes.³⁸ In a work where size and temperature dependency of LC molecules and surfactants trapped inside a spherical cavity were investigated, It is reported that phase transition temperature depends on the droplet size.¹⁰⁸ Several simulation studies performed by the de Pablo group quantified the size and/or temperature dependency of surface anchoring, which leads to isotropic-to-radial transitions.^{38, 39, 96}

Coarse-grained simulation methods have attracted interest in the investigation of LC anchoring due to relatively large time and length scales that they can probe. Zhang and co-workers¹⁰⁹ developed different coarse-grained models representing 5CB

molecules. Using these models, Zhang and co-workers were able to obtain isotropic-nematic transitions as well as diffusion coefficients. One of their models successfully reproduced experimental results for the nematic phase of 5CB at 300 K and 1 atm. The simulated density was 1.003 g/cm^3 , orientational order was calculated as 0.48, and the nematic-to-isotropic transition temperature was obtained at 305 – 310 K. The correspondent experimental data are 1.02 g/cm^3 , 0.54, and 306.7 – 308 K, respectively. Although the simulated diffusion coefficients were larger than experimental values, they provided a better match than atomistic simulations. In another coarse-grained study, the structural properties of self-assembled surfactant aggregates were investigated at the LC/water interface. Depending on the LC-surfactant tail affinity, it was possible to detect *condensed amphiphiles monolayers*, and, above a critical surfactant coverage, LCs homeotropic anchoring was induced, in agreement experiments.⁶²

One coarse-grained simulation method that is attracting vast interest in materials modelling and simulation is that of Dissipative Particle Dynamics (DPD).^{110, 111} DPD has been extensively used for studying soft materials, such as copolymers,¹¹²⁻¹¹⁴ nanoparticles,¹¹⁵⁻¹¹⁷ surfactants,¹¹⁸⁻¹²² and liquid crystals^{37, 63, 123}. The results of these simulations are in general consistent with experiments, and sometimes explain phenomena that are hard to observe with experimental techniques alone. For example, Al Sunaidi et al.¹²³ used DPD to study the phase transitions encountered by rod-like molecules, and described the conditions at which isotropic, nematic, smectic A and crystalline phases are stable. Zhang and Guo⁶³ studied the interactions between LCs and amphiphilic rod-coil polymers in an aqueous environment. Their parametric study showed the effect of soft potential coefficients to the anchoring of LCs. Inokuchi and Arai³⁷ studied LCs, water, and surfactants confined in a spherical geometry. They studied the self-assembly with respect to temperature and surfactant concentration. In all the DPD studies just summarized, the parameters that were systematically changed during the investigation were either temperature or soft repulsion coefficients, and the target of the investigations was the anchoring between LCs and amphiphilic polymers.

This brief overview demonstrates the importance of understanding LCs anchoring. In short, molecules at the LC/solvent interface contribute to orient the mesogens, starting from the interface, but also within inner regions, and eventually across the whole LC structure system. In this thesis, the interactions of LC/surfactant

and LC/NP were investigated in water medium. Once the LC behaviour and surface anchoring are identified, the study moved towards the understanding of structural defects within the LC droplets. For such calculations, larger scale simulations were employed. A link was created between nanoscale molecular simulations and microscale continuum mechanics simulations, proposing that these two approaches could be integrated and used in parallel for the understanding of LC-based advanced applications.

CHAPTER 3

COMPUTATIONAL METHODS AND ALGORITHMS

3.1 DISSIPATIVE PARTICLE DYNAMICS (DPD)

DPD is a coarse-grained simulation technique that allows longer time and larger length scales than the atomistic molecular simulations provide, in some cases approaching experimentally-relevant conditions.^{112, 124} DPD simulation methodology was first introduced by Hoogerbrugge and Koelman,^{110, 111} developed by Espanol and Warren^{124, 125}, and modified by Groot and Warren.¹²⁶ Due to computational efficiency, it was challenging to consider previously developed methods (such as molecular dynamics, MD) as a tool for complex fluids in 3D systems. The main reason for the introduction of DPD was the fact that it was able to predict hydrodynamic behaviour of molecules in a much faster way than molecular dynamics simulations (MD).¹¹⁰

In the DPD algorithm, the positions and momenta (\vec{r} and \vec{p} , respectively) of N number of beads (each with mass m) present within a simulation box are updated along a series of discrete time steps:¹²⁶

$$\vec{r} = (\vec{r}_1, \vec{r}_2, \vec{r}_3 \dots \vec{r}_N) \quad (3.1)$$

$$\vec{p} = (\vec{p}_1, \vec{p}_2, \vec{p}_3 \dots \vec{p}_N) \quad (3.2)$$

$$\frac{d\vec{p}_i}{dt} = \frac{d^2(\vec{r}_i)}{dt^2} m = \vec{F}_i \quad (3.3)$$

The time evolution of position and momenta is calculated via Newton's second law of motion (Eqn. 3.3), for which there is no analytical solution. Therefore, numerical

solutions are required, that will iteratively solve this equation, e.g. velocity-Verlet algorithm.¹²⁷ In the velocity-Verlet algorithm, position and velocity are updated in every iteration, and force acting on a particle is assumed to be independent from velocity, which is not the case in DPD algorithm. For that reason, DPD uses a modified version of the velocity-Verlet algorithm, where there is a mid-step for *predicted* velocity that is used for calculation of the force in each time step.¹²⁶ Particles in DPD simulations are named as *beads*, and for simplicity they are all assumed to have mass equal to 1, in reduced DPD units. The force is divided into three parts, namely conservative, dissipative, and random forces, and calculated within a cut-off distance that is at the same time the unit of length, r_c :

$$\vec{F}_i = \sum_{j \neq i} (\vec{F}_{ij}^C + \vec{F}_{ij}^D + \vec{F}_{ij}^R) \quad (3.4)$$

where \vec{F}_{ij}^C is the conservative force exerted by particle j on particle i , acting along the line of centres of two particles and it is calculated as follows:

$$\vec{F}_{ij}^C = \begin{cases} \alpha_{ij}(1 - r_{ij})\hat{r}_{ij} & (r_{ij} < 1) \\ 0 & (r_{ij} \geq 1) \end{cases} \quad (3.5)$$

Where α_{ij} is a maximum repulsion that determines the strength of the conservative force between particle i and j , $\vec{r}_{ij} = \vec{r}_i - \vec{r}_j$, $r_{ij} = |\vec{r}_{ij}|$ and $\hat{r}_{ij} = \vec{r}_{ij}/r_{ij}$. An important feature of DPD is that the bead – bead interaction potentials are *soft*, which allows researchers to probe length and time scales that are approaching experimental ones.¹²⁴ The outcome of DPD simulations depend strongly on the parameterization, and in particular on self-repulsion (among same type of species) and inter-species repulsion coefficients (α_{ij}). The particles in DPD (beads) were not regarded as molecules but lumps of molecules that serve as fluid particles, which was convenient for calculating hydrodynamics in polymer physics.

The two remaining forces are dissipative (drag) force, \vec{F}_{ij}^D , and random force, \vec{F}_{ij}^R , given as follows respectively:¹²⁶

$$\vec{F}_{ij}^D = -\gamma\omega^D(r_{ij})(\hat{r}_{ij} \cdot \vec{v}_{ij})\hat{r}_{ij} \quad (3.6)$$

$$\overrightarrow{F}_{ij}^R = \sigma \omega^R(r_{ij}) \zeta_{ij} \Delta t^{-\frac{1}{2}} \hat{r}_{ij} \quad (3.7)$$

where ω^D and ω^R are r -dependent weight functions, ζ_{ij} is a Gaussian random number with zero mean and chosen independently for each pair of interacting particles, at each timestep, Δt .¹²⁶ Due to the canonical ensemble, it is proven that dissipative force and random force should have a certain temperature-based relation with relative amplitudes.¹²⁵ This was covered with the relations below:

$$\omega^D(r_{ij}) = [\omega^R(r_{ij})]^2 \quad , \quad \sigma^2 = 2\gamma k_B T \quad (3.8)$$

$$\omega^D(r_{ij}) = [\omega^R(r_{ij})]^2 = \begin{cases} (1 - r_{ij})^2 & (r_{ij} < 1) \\ 0 & (r_{ij} \geq 1) \end{cases} \quad (3.9)$$

The friction coefficient and the random force were taken as $\gamma = 4.5$ and $\sigma = 3$, respectively.¹²⁶ Unitless length (r_c) and time (τ) parameters of DPD simulations are converted to angstrom (\AA) and microsecond (μs) units by applying the protocol defined by Groot and Rabone.¹¹⁹ Simulation conditions, duration and parametrization were separately explained in each chapter. For all DPD simulations the LAMMPS software package was utilized.¹²⁸ In DPD, the dissipative and random forces serve as a thermostat. In an NVT or NPT ensemble, one would thermostat the system twice. Standard NVT type DPD can be invoked in LAMMPS by an NVE ensemble. Although some calculations were conducted with NVT or NPT ensemble in this thesis, analysis showed that the results were not particularly affected due to the double thermostat on those simulations. For visualization of results, Ovito¹²⁹ and VMD¹³⁰ software were used.

3.2 MOLECULAR MODELLING

As stated previously, coarse-grained modelling is implemented for DPD calculations. In coarse-graining certain intermolecular and intramolecular interactions are overlooked, and molecules are represented as chunks of atoms, namely beads. Such simplification creates an advantage for large time (length) scales because simulations can be conducted up to microseconds (micrometres) without being computationally more demanding than atomistic simulations. In this thesis, 5 water molecules are

represented by a single DPD bead. All beads are equal in size. Degree of coarse graining, N_m , is defined as the arbitrarily chosen number of water molecules in a single DPD bead. Therefore, corresponding DPD bead size is equal to volume of 5 water molecules, 150 Å³. Simulated bead density, ρ , was chosen as 3, which indicates that in r_c^3 there are three beads, therefore number of beads in a simulation box was set once the box size was selected. Selection of N_m and density was made based on a similar study conducted by Fan and Striolo.¹³¹ Consequently, r_c becomes:

$$r_c = \sqrt[3]{150\text{\AA}^3 \times 3} = 7.66 \text{\AA} \quad (3.10)$$

In order to obtain the time parameter in microsecond units, self-diffusion coefficient of water beads must be calculated and used in the following equation:

$$\tau = \frac{N_m \times D_{sim}}{D_w} \quad (3.11)$$

where D_{sim} is the simulated and D_w is the experimentally obtained value for self-diffusion coefficient of water, and D_w is taken as $2.43 \times 10^{-5} \text{ cm}^2/\text{s}$.¹¹⁹ The simulated coefficient $D_{sim} = 0.0123 r_c^2/\tau$, was multiplied by the degree of coarse graining because mean square displacement of water beads represents $1/N_m$ that of water molecules.¹¹⁹

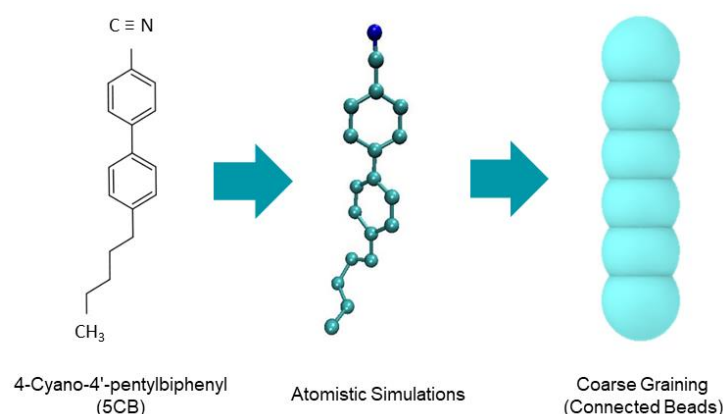


Figure 3.2.1. Atomistic and coarse-grained models of a common LC molecule (5CB).

The liquid crystal molecules (LCs) considered here are composed of 6 beads connected in a rod-like arrangement. Consecutive beads are connected with a harmonic spring defined for both surfactant and LC molecules. Bond length potential

$E_{\text{bond}} = k_{\text{bond}} \times (r_{ij} - r_0)^2$ and angle bending potential $E_{\text{angle}} = k_{\text{angle}} \times (\theta_{ijk} - \theta_0)^2$ are used, where r_0 is $0.6 r_c$ and θ_0 is 180° . In LAMMPS the angle θ_0 is specified in degrees although it is converted to radians for simulations, therefore k_{angle} stands for energy per radian². In Figure 3.2.1, an example molecule of 5CB (4-cyano-4'pentylbiphenyl) was shown, and its molecular models are represented for both atomistic modelling and coarse-grained modelling for DPD simulations. Unless otherwise stated in the chapter, this LC model was used throughout the thesis.

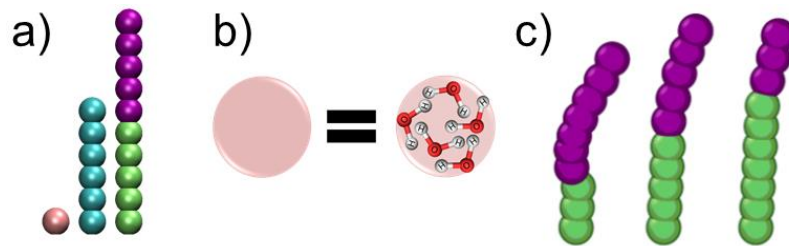


Figure 3.2.2. (a) Molecular models of water, liquid crystal, and surfactants. Representations of (b) a water bead and (c) surfactants with head to tail ratio, $S_{\text{head}}/S_{\text{tail}} = 7/3, 5/5$ and $3/7$, respectively.

Three amphiphiles (surfactants) were considered. Each surfactant molecule (S) was composed of 10 beads, connected to form a chain; the head-group represents the coil block, and the tail-group represents the rod block of each surfactant. Hydrophilic surfactant heads are indicated as S_{head} , whereas hydrophobic surfactant tails are identified as S_{tail} . While all surfactants considered are composed of 10 beads, the number of beads assigned to head- and tail-groups distinguishes the various surfactants. The three surfactants are characterized by: $S_{\text{head}}/S_{\text{tail}} = 7/3, 5/5$ and $3/7$ as can be seen in Figure 3.2.2(c). To preserve the rigidity of rod-like LCs and surfactant tails, k_{bond} and k_{angle} are defined as $100 k_B T/r_c^2$ and $100 k_B T$ respectively, between consecutive beads. For the surfactant head groups, which are flexible, k_{bond} and k_{angle} are set at $50 k_B T/r_c^2$ and $30 k_B T$, respectively.

Although beads in DPD simulations are *soft*, colloid models could be developed by forming rigid particles composed of many beads,^{124, 132} Nanoparticles were considered in six different shapes, and for each NP shape, two NP sizes were simulated: named as small and large NPs. Schematic representations for shapes and sizes of the *small* NPs were presented in Figure 3.2.3. The NPs considered are

spheroids (i.e., oblate and prolate ellipsoids), spheres, cylindrical rods, cubes, and star shaped. The volume of each small NPs ranges between 4.0 and $5.5 r_C^3$. Each NP was composed of different number of beads: rod-shaped NPs contain 112 beads, star-shaped NPs 154 beads, and each of the other NPs contain 125 beads. The density of beads within the volume of the NPs is in the range $23.1 - 33.0$ beads/ r_C^3 .

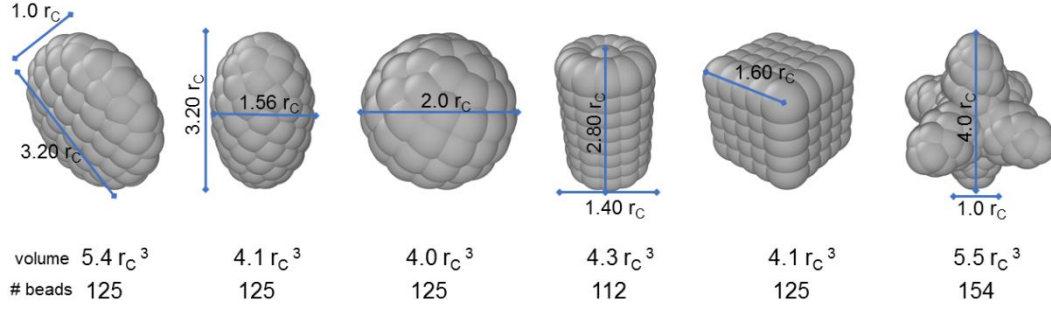


Figure 3.2.3. Sizes and volumes of the small nanoparticles (NPs) modelled in this work. Left to right: disc, ellipse, sphere, rod, cube and star shaped NPs.

To test the effect of particle size, also *large* NPs were considered. In these simulations, because of computing power limitations only one NP was simulated on one LC droplet. To generate the *large* NPs, the dimensions shown in Figure 3.2.3 were increased three-fold. Different than the small NPs, the large NPs were hollow. Using hollow nanoparticles decreased the relative pressure of the system and the overall density of the simulation box but did not change the LC – NP interactions because the interactions beyond cut-off distance (r_C) were already eliminated. Surface bead density and roughness were maintained constant among the large NPs, by applying *rigid* command in LAMMPS to preserve the NP structure throughout the simulations.

3.3 CALCULATION OF ORIENTATIONAL ORDER

Orientational order parameter is a quantitative alignment indicator that characterizes the distribution of the LC molecules of the simulated volume.¹³³ Scalar order parameter, S , the global average of molecular order within the system:

$$S = \sum_{i=1}^N (3 \cos^2 \theta_i - 1) \times \frac{1}{2N} \quad (3.12)$$

In Eq. (3.12), θ represents the angle between molecular axis of LC and the direction vector. When θ is equal to 90° , order parameter becomes -0.5 , indicating that

the LC considered is perpendicular to the direction vector; when θ is 0° , order parameter becomes 1, indicating that the LC is aligned parallel to the direction vector. By definition, $S = 0$ represents a completely isotropic phase and $S = 1$ indicates a nematic phase, with perfect alignment of mesogens.¹³⁴ For a nematic bulk phase of LCs, S is defined to be 0.4 for high temperatures and 0.6 for low temperatures.¹³³ In this thesis, for the study of cylindrical confinement, the direction vector was chosen as the long axis of the cylinder formed by LC molecules (Chapter 4). For the droplet studies where anchoring with surfactants and nanoparticles were investigated (Chapter 5 and Chapter 6), the direction vector was defined to pass through the poles of the droplets. To find the location of these poles post-processing was required. Firstly, average direction of all molecules in the droplet were obtained for every frame that was considered for calculation of orientational order. Rod-shaped LC molecules were treated like unit vectors for those calculations, and an average direction vector was obtained. Then, the global order was calculated by using Eqn 3.12, where the angle (θ) is between the average direction vector and all molecules. The poles were formed by the planar alignment of LC molecules, and they created two surface defects (namely boojums) on those tips. Calculating order in that particular way was useful to identify the changes on pristine droplet, when another chemical was incorporated.

For the droplet study where the surface anchoring and defect structures were investigated by encapsulating LC molecules within a rigid shell (Chapter 7), a different approach than a predefined direction vector was adopted. Instead of measuring the angle with respect to the direction vector for each molecule in the system, the orientational order of nematic liquid crystals is described by an order tensor which in the uniaxial form takes the shape:^{27, 28}

$$Q = \frac{S}{2}(3\hat{n} \otimes \hat{n} - I) \quad (3.13)$$

where \hat{n} is the liquid crystal director. This is a symmetric, traceless tensor and its dominant eigenvalue is S , the scalar or uniaxial order parameter. This order tensor representation is also the backbone of continuum mechanics calculations, which is explained in Chapter 3.4. Adapted to DPD calculations that yield an ensemble of molecular positions and orientations, a global counterpart of Eqn. 3.13 can be written as:³⁸

$$Q_d = \frac{1}{N} \sum_{i=1}^N \left[\hat{u}_i \otimes \hat{u}_i - \frac{I}{3} \right] \quad (3.14)$$

where N is the number of mesogens in the ensemble and \hat{u}_i is the unit vector representing the molecule's direction. The cumulative uniaxial order parameter, which in this work I define as S_U , can be extracted from the dominant eigenvalue, λ_1 , of Q_d as:

$$S_U = \frac{3}{2} \lambda_1 \quad (3.15)$$

When mesogens are aligned parallel to each other, e.g. in a droplet with a planar anchoring to the surrounding liquid, the value of S_U is expected to be high. However, when there is a radial distribution of mesogens in the droplet, i.e., homeotropic anchoring, S_U will be low, although there is a certain order within the system. Previously, de Pablo and co-workers discussed also a global order parameter S_R , the radial order parameter to quantify the degree of satisfaction of a perfect radial order inside an LC droplet:³⁸

$$S_R = \frac{1}{2N} \sum_{i=1}^N [3(\hat{u}_i \cdot \hat{r}_i)^2 - 1] \quad (3.16)$$

where \hat{r}_i is the unit vector represents the position of molecule i in the droplet.

For analysis of orientational order of the systems considered in this thesis, usually last 0.149 μ s was divided into 100 frames, if a different procedure was applied, this was indicated. Orientational order was calculated in each of 100 frames, and average was reported along the uncertainty which is the first standard deviation of 100 results.

3.4 Q-TENSOR SIMULATIONS AND DEFECTS

Liquid crystals change their phase from isotropic to nematic with the decreasing temperature. During such transition there is an associated increase in the order of the molecules. To be able to quantify the change in the order, the Q-tensor theory has been developed.²⁸ In this approach, the tensor order parameter Q , is not dependent on angle with respect to the direction vector but it is a symmetric traceless three by three matrix, as explained in the previous section. The three eigenvalues of Q provide

the nematic order in the orthogonal directions.¹³⁵ Calculations utilizing this theory ignore the chemical identity of LC molecules, and represent them as unit vectors without a sign in a continuum domain. Therefore, order analysis for a volume close to experimentally accessible sizes is computationally much more affordable than using molecular simulations.

The Q-tensor simulations were conducted using the model and computer programs developed by Fernandez and co-workers¹³⁵⁻¹³⁷ based on the Landau – de Gennes theory.²⁷ The reference work describes the Q-tensor statistics and algorithm of the software in detail.^{135, 136} The method consists of finding the Q-tensor distribution over the complete volume, that minimizes the total free energy of the system, which is composed of the thermotropic (bulk) energy (F_B), the elastic distortion energy (F_D), the surface energy (F_S), and when an external electric or magnetic field is in consideration, the electromagnetic energy (F_E).^{27, 28, 135}

The bulk energy is related to the phase of the material and the distortion energy represents structural deformations; they are both dependent on the intensive variables.¹³⁸ For F_B and F_D calculations, the chosen parameters correspond to very common 5CB molecule.¹³⁹ For F_S calculations, two surfaces were defined that impose strong planar degenerate or strong homeotropic anchoring in this thesis.¹³⁷

Table 3.4.1. Parameters for the Q-tensor calculations.

Calculation	Parameter	Units	Value
F _B	A	N/m ²	-1.27×10 ⁶
	B		-2.26×10 ⁶
	C		1.73×10 ⁶
F _D	K ₁₁	pN	6.2
	K ₂₂		3.9
	K ₃₃		8.2
F _S	homeotropic	-	strong
	planar degenerate		strong

The coefficients A , B , and C in the bulk energy are used to determine the state of liquid crystal, e.g., uniaxial, biaxial, or isotropic. A is temperature dependent whereas B and C are assumed to be not.¹³⁸ When the interest is limited to the characterisation

of the general behaviour, the thermotropic parameter A in Table 3.4.1 would normally be taken to be zero, which would correspond to a case equivalent to $T = T^*$, i.e., the temperature is assumed to be equal to isotropic-to-nematic transition temperature (T^*).^{140, 141} In the cases covered in this thesis, $A < 0$, corresponding to a temperature $< T^*$ was used; the results from additional calculations with $A = 0$ are provided in Appendix C.

The coefficients K_{11} , K_{22} and K_{33} are defined to be Frank elastic constants that represent splay, twist, and bend elastic constants, respectively.¹⁴² Strong anchoring is defined as boundary condition for both surface types and does not contribute directly to the free energy. Weak anchoring of any type is defined by their direction and strength and lead to a calculation of a surface anchoring energy as part of the total free energy. All parameters used in this study can be found in Table 3.4.1.

A mesh structure composed of tetrahedral elements for a spherical droplet of the $0.1 \mu\text{m}$ size was built. The code performs adaptive meshing, namely meshes can be reformed and concentrated around the disclinations as the calculations evolve. Such property enables the user to obtain a clear defect structure. In this work, I iterated the calculations until the largest change in Q-tensor value was below five significant digits. After identifying the final results, simulations were repeated, and mesh reforming occurred every 20 steps for elements within which the Q-tensor change exceeds 0.3. For example, the number of nodes was increased from approximately 2500 to 9000 or more, from the initial to the final mesh, respectively, to refine the analysis of the defect regions.¹³⁵

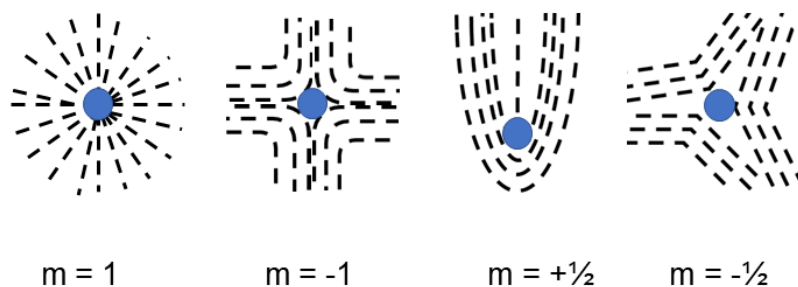


Figure 3.4.1. Defect structures, defect cores (blue) and their strength (m).

Although nematic phase of LC molecules is expected to be highly ordered, there might be certain spots on the simulated volume where there is a discontinuous

behaviour, which is named as the *defect*. The defect structures are essential part of sensing devices, and they might change with respect to the confinement that the LC molecules are in.²⁷ In the event of a continuous field, such as in Q-tensor calculations, defects are categorized with respect to their strength. Strength is defined as the quantitative value corresponding to the 2π rotation of director field around the defect core.¹⁴³ In Figure 3.4.1, some of the common defects are shown.

The DPD simulation technique described in 3.1 was used throughout the thesis. Molecular modelling defined in 3.2 was utilized for all Chapters from 4 to 7, and when an additional molecule was implemented, or changes were made, this was noted. At least one method for calculating orientational order, defined in 3.3 was used in each Chapter. For confinement studies where addition of different chemicals (such as surfactants and nanoparticles) was investigated, order was calculated through a pre-defined direction vector. Those results are presented in Chapters 4 – 6. For the investigation of bulk LC behaviour and defects within droplets, Q-tensor method was used for order, alongside the continuum mechanics approach (see 3.4) and presented in Chapter 7.

CHAPTER 4

CYLINDRICAL FORMATIONS OF LCS AND THEIR INTERACTIONS WITH SURFACTANTS*

The present chapter implements DPD to study cylindrical LCs formations dispersed in water, in the presence of surfactants. Because of periodic boundary conditions the cylindrical structures considered are effectively infinitely long. Consequently, the results probe regions away from the basal terminations of the LC cylinders. In most cylindrical formations studied, LCs are injected to capillary tubes with the addition of amphiphiles such as lecithin^{64, 66} and N,N-dimethyl-N-octadecyl-3-aminopropyl-trimethoxysilyl chloride (DMOAP)⁶⁷ to induce homeotropic anchoring of LC molecules with tube walls. The system modelled here allows us to systematically investigate the effect of surfactant morphology on LC anchoring on a curved interface, without the presence of a capillary tube or any other container.

Three different rod-coil amphiphiles are modelled, which are explained in Chapter 3.2. These amphiphiles have the same length, but they have different hydrophobic tail lengths: short, moderate, and long, respectively. The results show that varying the number of hydrophilic coils and hydrophobic rods in this simple surfactant model can largely affect LCs' anchoring. When the surfactant density at the interface is high enough, phase segregation of surfactants causes the mesogens to shift from planar to homeotropic anchoring. Such transition is effective only in a small region in most of the systems considered here. However, the parametric analysis showed that a small decrease in the repulsion parameter that describes surfactant tail – LCs

*The results given in this chapter were published in Physical Chemistry Chemical Physics with following reference: Z. Sumer and A. Striolo, " Manipulating molecular order in nematic liquid crystal capillary bridges via surfactant adsorption: guiding principles from dissipative particle dynamics simulations", Phys. Chem. Chem. Phys., 2018, 20, 30514-30524. The original manuscript has been rearranged to conform to the format requirements of the dissertation.

interactions is sufficient to cause changes in mesogens orientation throughout the tube, which is in general agreement with literature results obtained at flat LC – solvent interfaces.

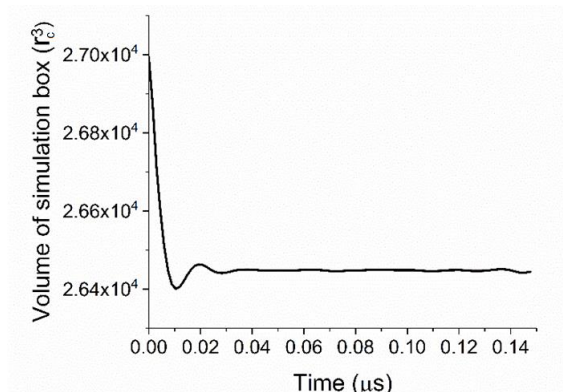


Figure 4.1. Volume change of the system that was simulated for additional 0.14 μs in NPT ensemble.

All simulations are run for 3×10^6 steps, with integration time Δt defined as 0.01τ in DPD units. Each system was simulated for $0.447 \mu\text{s}$, with the last $0.149 \mu\text{s}$ used for data analysis. To ensure reproducibility each system was simulated twice, with different initial configurations. Test simulations were conducted in the NPT ensemble. For these simulations the system with lower pressure (95% of that observed in the system containing only water, $23.0 \text{ k}_B\text{T}/r_c^3$, at the same temperature and density, $3 \text{ beads}/r_c^3$) obtained at the end of NVT simulations was chosen. NPT simulations were conducted for $0.14 \mu\text{s}$, during which time the simulation box size changed from $30 \times 30 \times 30 r_c^3$ to $29.78 \times 29.78 \times 29.78 r_c^3$ (the correspondent density increased from 3 to $3.07 \text{ beads}/r_c^3$), as shown in Figure 4.1. This change in box size was considered negligible, and all subsequent simulations were conducted in the NVT ensemble.

Table 4.1. Repulsion coefficients (α_{ij}) used in the simulations in $\text{k}_B\text{T}/r_c$ units.

	Water	LC	Shead	Stail
Water	25	50	25	50
LC		25	50	20, 25
Shead			25	50
Stail				25

To determine conservative force parameters, the protocol proposed by Groot and Warren was followed.¹²⁶ They concluded that $\alpha_{ij} = 25 k_B T / r_c$ was representative of soft interactions among the same type of beads in an aqueous environment. Because the density chosen here was 3, α_{ij} was defined to be 25 among same beads. Table 4.1 shows the parameters used in this chapter.

Initial configurations of simulation boxes were prepared by simulating the system at reduced temperature 1.0 $k_B T$ and with repulsion coefficient set to 25.0 between LC and surfactant tail, as schematically shown in previous chapter, Figure 3.2.2(c). Pure LC simulations are run in a $20 \times 20 \times 20 r_c^3$ simulation box, whereas simulations for LC – surfactant interaction are run in a $30 \times 30 \times 30 r_c^3$ simulation box. Periodic boundary conditions were applied in all directions. In each simulation, 3000 LC molecules were used. Within systems and conditions investigated in this work, 3000 mesogens were sufficient to yield a cylindrical form that spans the length of the simulation box. In the initial configurations, the LC molecules were arranged in a cylindrical bridge that spans the entire length of the simulation box along the x-axis. Because the periodic boundary conditions are applied in 3 dimensions, the LC cylinder is effectively infinitely long. So, investigation of the effect of surfactants on LC anchoring within a curved interface was possible. The cylindrical formation allowed a relatively easy analysis of results such as density profiles on that curved interface, while removing the constraints of spherical form on both mesogens and surfactant aggregates. The basal terminations of the LC cylinders are not included in this study.

Table 4.2. Compositions of simulated systems with (a) 1000 surfactant molecules where $\alpha_{LC-Stail} = 25$; (b) 1500 surfactant molecules where $\alpha_{LC-Stail} = 25$; and (c) 1000 surfactant molecules where $\alpha_{LC-Stail} = 20$.

	Water	LC	Surfactant
a	65.43%	22.22%	12.35%
b	59.26%	22.22%	18.52%
c	65.43%	22.22%	12.35%

It is envisioned that surfactants could be used to stabilize aqueous dispersions of LCs. Different amounts of surfactant molecules are used to investigate the effect of surface coverage. 1000 surfactant molecules (55% coverage) were used as a start,

and then increased to 1500 (80% coverage). Compositions can also be found in Table 4.2. Surface coverage is calculated by estimating amount of beads required to cover the surface of a cylinder with radius $10 r_c$ and length $30 r_c$, based on similar studies in the literature.^{62, 63} Mahajan and co-workers noted that LC bridges in a nematic phase act as an ordinary Newtonian liquid bridge, which might collapse above a certain length-to-diameter ratio.¹⁴⁴ In these simulations this collapse is prevented by using a very low ratio of length-to-diameter, by the fact that gravity is not considered, and by the fact that periodic boundary conditions effectively stabilise the bridges.

4.1 BULK LIQUID CRYSTALS

Since the purpose of this work is to investigate the dependency of LC anchoring to the length of hydrophobic rods in model surfactants, the first required step is to determine the simulation temperature at which bulk LCs undergo the isotropic-to-nematic phase transition. Bulk simulations were conducted at different temperatures in the range $0.1 - 1.0 k_B T$. At each temperature, the scalar order parameter was computed with respect to the x, y and z axis and highest value was reported. The results are shown in Figure 4.1.1. The results clearly show that in the temperature range $0.8 - 1.0 k_B T$, the LCs are in an isotropic phase, as expected because of the high temperature. At these conditions, the S parameter varies within the range $0.00 - 0.02$.

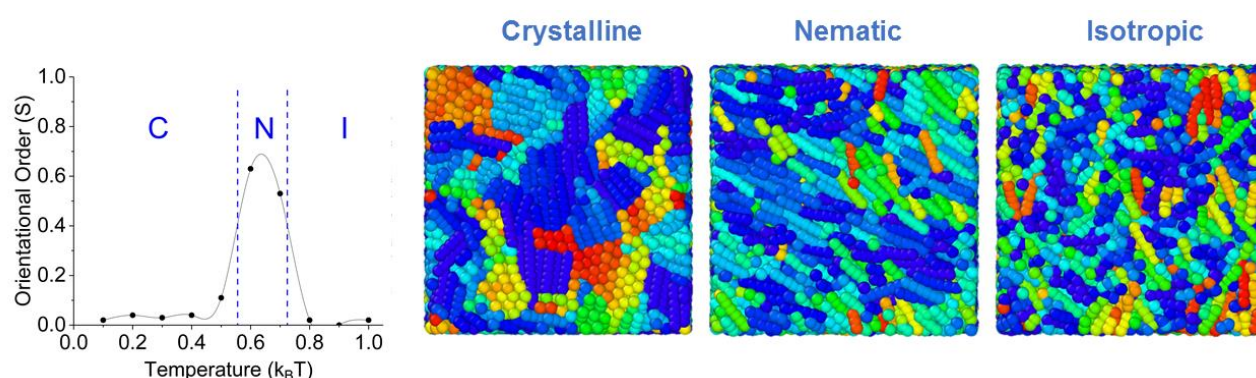


Figure 4.1.1. Orientational order parameter (S) of bulk LC vs. scaled temperature and snapshots of LCs in crystalline (C), nematic (N) and isotropic (I) phases. Line between data points is guide to eye.

As the simulated temperature is decreased, the results show an increase in the order parameter S in the temperature range $0.6 - 0.7 k_B T$, where S becomes 0.63 and 0.53, respectively. These results indicate that the LCs are in the nematic phase at

these conditions. When the temperature is reduced further, below $0.6 \text{ k}_B\text{T}$, a solid phase is observed. The results in Figure 4.1.1 show low values for the order parameter S (between $0.02 - 0.11$). However, analysis of simulation snapshots indicates that the LC molecules in the bulk yield small grains that are locally aligned but misaligned with respect to each other. The relative disorder between different grains yields the overall low S .

The results from the bulk simulations show that in the temperature range $0.6 - 0.7 \text{ k}_B\text{T}$ the LCs were in the nematic phase. The highest of these temperatures was selected for the subsequent simulations, so that the LCs can possess certain orientational order and still be in the liquid phase.

4.2 LC BRIDGES IN WATER

Model for a cylindrical LC bridge immersed in water was prepared, and simulations at $0.7 \text{ k}_B\text{T}$ were conducted. The goal of these simulations was to ensure that the model is suitable to replicate the experimental predictions, as well as to prepare the reference system for assessing quantitatively the effect of surfactants adsorption on LC order. One representative simulation snapshot for the LC – water system (no surfactant present) is shown in Figure 4.2.1(a). The simulation results show that the mesogens are aligned parallel to the cylindrical axis, exhibiting an orientational order (S) equal to 0.70 . The LC cylinder is shown in Figure 4.2.1(b). In summary, the control simulations at $0.7 \text{ k}_B\text{T}$ showed that (i) LC molecules exhibit nematic phase within the mesogen cylindrical formation dispersed in water (no other species is present), (ii) planar anchoring is observed at the interface between the LCs and water. All subsequent simulations are conducted at $0.7 \text{ k}_B\text{T}$.

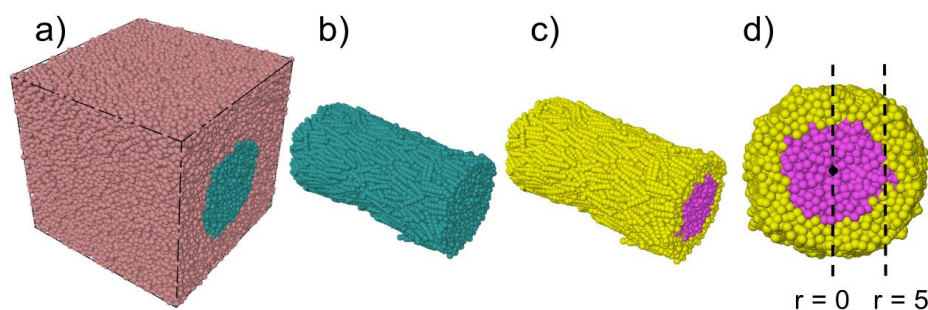


Figure 4.2.1. (a) Orientation of LC molecules in water without any surfactant added at $0.7 \text{ k}_B\text{T}$ ($S = 0.70$) and (b) LCs with water beads removed. (c) and (d) Schematic representation of LCs that are located at the core ($r \leq 5 r_c$) and outer ($r > 5 r_c$) region of cylinder.

To quantify changes in LC order within the cylinder, the cylindrical LC was arbitrarily divided into two regions, shown with different colours in Figure 4.2.1(c) and (d). The *core* region is composed of mesogens within a radius of $5 r_c$ from the centre of the cylinder; the *shell* region comprises those mesogens found within a radius from 5 up to $12 r_c$ from the centre. Note that the outer radius changes for the various simulations because as different surfactants are introduced, the shell region can expand slightly up to $12 r_c$.

4.3 SURFACTANT ADSORPTION AND ORIENTATIONAL ORDER

Starting from the base case discussed in Figure 4.2.1, the effect of surfactants adsorption on the LC anchoring was systematically investigated. Unless otherwise noted, the interaction between LC and surfactant molecules is described by $\alpha_{\text{LC-S}_{\text{tail}}} = 25$, and the repulsion parameter is chosen identical to the self-repulsion parameter, $\alpha_{\text{self}} = 25$. The surfactants considered have different tail lengths, as shown in Figure 3.2.2. The number of S_{tail} beads is increased from 3, to 5 and to 7, respectively. Note that the total number of beads per surfactant molecule is always 10, thus the number of beads in the head-groups reduce from 7, to 5, and to 3, respectively, for the three surfactants simulated. The results obtained when the three surfactants were adsorbed at the LC – water interface are shown in Figure 4.3.1. In these simulations, the number of surfactant molecules were 1000, which yields an overall surface coverage of ~55%.

In Figure 4.3.1(a) the results shown for the surfactants with 3 beads in the tail-groups are shown. Visual inspection of multiple simulation snapshots (~100 per simulation run, separated from each other by 10^4 time steps) reveals that the surfactants are aligned homeotropically (perpendicularly to the interface). The surfactant tail lengths are too short to penetrate the LCs. The order parameter of LCs is calculated as 0.63 ± 0.02 , which is slightly lower than S found in the control simulation of Figure 4.2.1(a) (0.70). In the core of the LC cylinder, orange in Figure 4.3.1(d), LCs exhibit $S = 0.64 \pm 0.03$, whereas in the shell region $S = 0.63 \pm 0.02$. These results show that the addition of the surfactants with 3 beads in their tail-groups does not affect the orientation of the LCs. In addition, LC molecules are found to preserve planar anchoring.

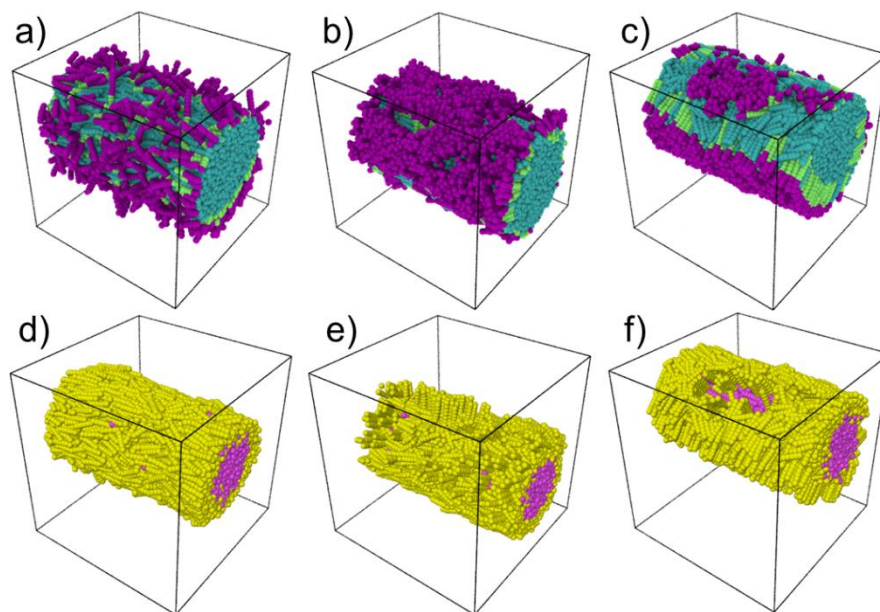


Figure 4.3.1. Configurations of LC and 1000 surfactant molecules with (a) 3 bead (b) 5 bead and (c) 7 bead-long tail-groups at 0.7 k_BT. The change in orientation in LCs is due to interactions with surfactants with (d) 3 bead (e) 5 bead and (f) 7 bead-long tail. LCs that are located in the core of cylindrical radius ($r \leq 5 r_c$) are shown in pink, the rest in yellow. Water beads are not shown for clarity.

As the number of beads in the tail-groups of the surfactants is increased from 3 to 5, the orientation of the mesogens at the shell region starts to shift from planar to homeotropic, as can be seen in Figure 4.3.1(b and e). Although the surfactant tails are shorter than the LC molecules, they interpenetrate the mesogens and affect their orientation. Within the bridge, the overall S decreased to 0.49 ± 0.03 . Analysis of the order within the fragment in Figure 4.3.1(e), shows that, at the core, S equals 0.57 ± 0.05 , suggesting that the LCs within a radius of $5 r_c$ are not affected by the surfactant molecules. At the shell region, S decreases to 0.43 ± 0.03 .

Similar results are observed in Figure 4.3.1(c and f) when the surfactants have 7 bead-long tails, in which case the overall order parameter decreases to 0.38 ± 0.04 . Although in this case the surfactant tail-groups are longer than the LCs, the mesogens at the core are not affected by surfactant adsorption at the surface. The results show that while at the core S remains 0.53 ± 0.05 , in the shell it sharply decreases to 0.27 ± 0.04 (see Figure 4.3.1(f)). These data suggest that, compared to results obtained for shorter LCs, either more LCs shift from planar to homeotropic, or the same number of LCs shift orientation, but orient in perfectly perpendicular direction with respect to the cylindrical axis.

Analysis of the simulation snapshots reveals a perhaps unexpected observation: the surfactants, adsorbed at the LC – water interface, are not homogeneously distributed on the surface. Instead, they segregate. Consequently, the LCs near the surfactants are perpendicular to the interface, while the LCs near the water beads remain parallel to the interface. Such distribution of the surfactants is attributed to lateral phase separation of the amphiphiles at the LC – water interface. When LCs are in a nematic phase, they yield elastic properties that have been shown to be able to affect the properties of interfaces, in some cases leading to new phases and phase separations.^{61, 145} Results suggest that perhaps LCs in nematic phase cause the surfactants to undergo a lateral phase separation. In other words, surfactants and LCs phase separated in order to preserve the high orientational order of LCs on the surface. In addition, Moreno-Razo et al.³² showed that packing of LC molecules at the interface is affected by nearby surface accumulation of other agents. Changes in surfactant density at the interface are also expected to yield changes in energetically favourable sites, and as a result it is possible that LCs are packed differently due to the local surfactant concentration. These results, combined with those in the literature, suggest that cooperative phenomena take place at the LC – water interface in the presence of surfactants: nematic LC phases trigger lateral phase separation of amphiphiles, while amphiphiles, at a large enough local concentration, trigger the radial alignment of LC molecules near the interface.

4.4 EFFECT OF SURFACTANT SURFACE DENSITY

To quantify the effect of surfactant surface density on LCs anchoring, simulations similar to those described in Chapter 4.3 were conducted, but the number of the surfactant molecules were increased to 1500. This yields a surface coverage of ~80%. The results are summarized in Figure 4.4.1. As the surfactant concentration is increased compared to the simulations discussed in Chapter 4.3, lateral phase separation is also observed. As a result, the morphology of the cylindrical LC appears to be slightly deformed, simply because of the un-even surfactants distribution.

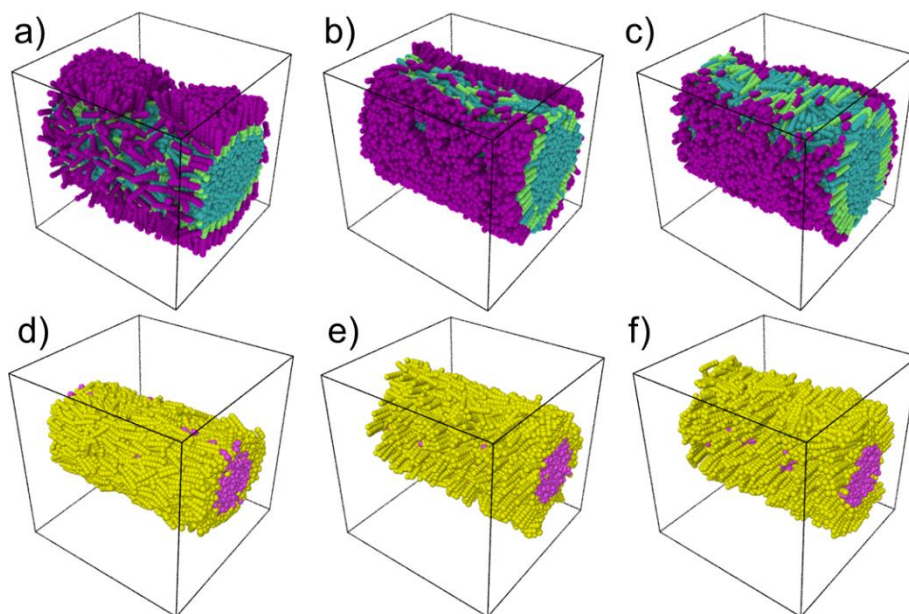


Figure 4.4.1. Configurations of LC and 1500 surfactant molecules with (a) 3 bead, (b) 5 bead, and (c) 7 bead-long tail-groups at $0.7 k_B T$. Orientation change in LCs due to interactions with surfactants with (d) 3 bead, (e) 5 bead, and (f) 7 bead-long tail-groups. LCs located in the core of cylindrical radius ($r \leq 5 r_c$) are shown in pink, the rest in yellow. Water beads are not shown for clarity.

One similarity with the systems described above is that LC molecules located at the core are not affected by the interactions with surfactant molecules. Therefore, it was concluded that, within this model, the surfactant effect on mesogen was strictly dependent on the location of LC molecules, and has no impact for LCs that are located in distances that are longer than the surfactant tails.

In Figure 4.4.1(a and d), the results are shown for surfactants with short tail-groups (3 beads). Overall, S is found to be 0.59 ± 0.03 , and it appears to be similar in the core and shell regions (0.62 ± 0.03 and 0.58 ± 0.03 , respectively). These results show that the surfactants with short tails considered here do not affect the order of the mesogens even though their concentration is rather high. This observation changes when the surfactants with longer tail-groups are considered. In Figure 4.4.1(b and e), simulation snapshots are shown for the LCs at contact with surfactants with tail-groups of 5 beads.

Visual inspection reveals that LC orientation is affected by the surfactant. The global order parameter S decreases to 0.43 ± 0.04 . As seen in Figure 4.4.1(e), while LCs at the core preserve high order with $S = 0.60 \pm 0.04$, LCs at the shell region show

$S = 0.32 \pm 0.06$. The effect is more pronounced when the surfactants with tail-groups of 7 beads are considered. The results are visualized in Figure 4.4.1(c and f). At this 80% surfactant coverage, the overall order parameter S decreases to 0.25 ± 0.03 . Note that S in the shell region becomes 0.05 ± 0.03 , while the order in the core region is preserved ($S = 0.57 \pm 0.04$). The results for the order parameter, corroborated by visual inspection, show that at this surface coverage, the surfactants with tail-groups of 7 beads cause almost all LC molecules in the shell region to assume homeotropic alignment.

4.5 EFFECT OF LC – SURFACTANT INTERACTIONS

As discussed above, the simulation results obtained here, as well as the results in the literature, suggest that there is a cooperative effect between surfactants and LC molecules, which determines both the distribution of the surfactants on the LC bridge and the anchoring of the mesogens. Because it is possible that the lateral phase separation between surfactant aggregates affects LC anchoring, a parametric study was conducted in which the repulsion between mesogens and surfactant tails were reduced. The correspondent repulsion parameter is decreased to $\alpha_{\text{LC-Stail}} = 20$. Decrease in repulsion to a value lower than the self-repulsion parameter (25) could be representative of coarse-grained models used to describe the self-assembly of ionic LCs and their interactions with ionic surfactants.^{146,147}

Although Coulombic interactions are not taken into consideration explicitly in these simulations, the effective attraction between surfactant tails and LCs is meant to reproduce, qualitatively, the combined effect of multiple interactions. Once $\alpha_{\text{LC-Stail}} = 20$, it is expected that the surface segregation evident from the snapshots shown in Figure 4.3.1 and Figure 4.4.1 is weakened. For this parametrization, only systems with 1000 surfactants were considered. The results are summarized in Figure 4.5.1. For all surfactants considered, the results show a homogeneous distribution on the LCs. The simulation snapshots also reveal that once the repulsion between LCs and surfactant tail-groups has been reduced, the change in mesogens order becomes longer ranged. In fact, the LCs at the core shift their orientation, which becomes isotropic. Now the discussion is on the results for each of the three architectures considered for the surfactants.

In Figure 4.5.1(a and d), the results are shown for the surfactants with tail-groups of 3 beads. The order parameter S is found to be -0.03 ± 0.03 . This negative order means that the mesogen molecules are oriented almost perpendicularly with respect to cylindrical axis, as explained in Eq. (3.12). The mesogens within the core yield $S = -0.06 \pm 0.04$, while those in the shell $S = 0.00 \pm 0.03$.

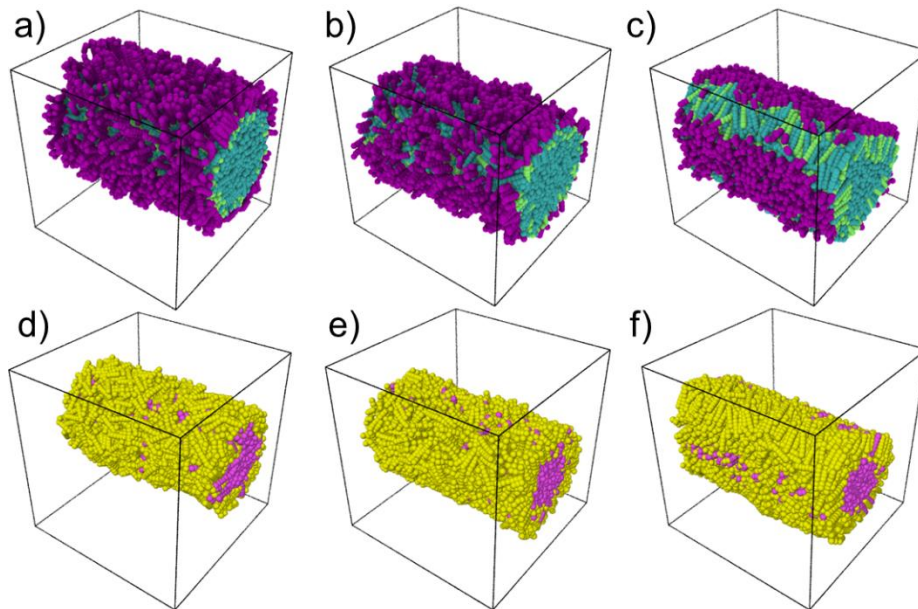


Figure 4.5.1. Configurations of LCs and 1000 surfactant molecules with (a) 3 beads, (b) 5 beads, and (c) 7 bead-long tail-groups at $0.7 \text{ k}_B\text{T}$ with $\alpha_{\text{LC-Shell}} = 20$. Orientation change in LCs due to interactions with surfactants with (d) 3 beads, (e) 5 beads, and (f) 7 bead-long tail-groups. LCs located in the core of cylindrical radius ($r \leq 5 r_c$) are shown in pink, the rest in yellow. Water beads are not shown for clarity.

A similar trend was observed for the surfactants with 5 beads in their tail-groups (Figure 4.5.1 (b and e)): overall S is -0.14 ± 0.02 . Orientational order in Figure 4.5.1(b) has a slightly lower value than in Figure 4.5.1(a), due to relatively longer surfactants tail-groups. For this surfactant the results show that the order for the mesogens in the core ($S = -0.12 \pm 0.04$) is similar to that for the mesogens in the shell ($S = -0.16 \pm 0.01$), which suggests that the range of interaction between the surfactants adsorbed on the LC bridge and the mesogens is large enough to affect equally all mesogens within the cylinder.

In Figure 4.5.1(c and f), the results obtained for the surfactants with 7 beads in their tail-groups are shown. The results show that, in addition to affecting the order of the mesogens, the surfactants also affect the shape of the droplet. The overall, core

and shell order parameters are -0.18 ± 0.03 , 0.04 ± 0.05 , and -0.31 ± 0.02 , respectively. Due to length and rigidity of surfactant tail-groups, and because the surfactants cause homeotropic order for the LCs, the original cylinder is deformed into a triangular prism by the adsorption of the surfactants. Presumably, the deformation of the droplet shape prevented us from observing long-range interactions between surfactants and LCs at the inner region of cylinder.

Parametric studies such as those discussed in Figure 4.5.1 could be extended to consider various surfactant – LC interactions, and also the effect of branching in the surfactant molecule. While this is beyond the scope of the present chapter, I would like to point out that previous studies show that branching affects the orientation of LC molecules.^{19, 21}

4.6 ORIENTATION OF LCS WITH RESPECT TO SURFACTANT DENSITY AND RADIUS

To further quantify the mesogens order as a function of surfactants architecture and density, order of each mesogen with respect to direction vector within the LC bridge was analysed. The results are shown in Figure 4.6.1, where LCs based on their orientations were distinguished: mesogens with an order parameter in the range of $-0.5 - 0.0$ are defined *homeotropically aligned*; $0.5 - 1.0$ as *in planar alignment*; $0.0 - 0.5$ as *tilted*. When there is no surfactant in the system, the order distribution is shown as black bars: 5% of the mesogens are homeotropically aligned, 17% are tilted, and the vast majority, 78%, are in planar alignment.

When 1000 surfactants are present, the results (Figure 4.6.1(a)) are shown in blue, green and purple bars for surfactants with 3, 5, and 7 beads in their tail-groups, respectively. As the tail length increases, the amount of mesogens in planar alignment decreases (69%, 58% and 49%, respectively), that of homeotropically aligned LCs increases (10%, 21% and 29%), and that of tilted LCs remain approximately constant $\sim 20 - 22\%$. These results show that as the surfactant tail length increases, anchoring becomes more and more homeotropic. Two reasons explain why many LCs preserve their planar orientation: (a) the LCs in the core region are not affected by surfactants, as explained above; (b) only 55% of the surface is covered by surfactants, with the LCs in the remaining surface maintaining planar anchoring.

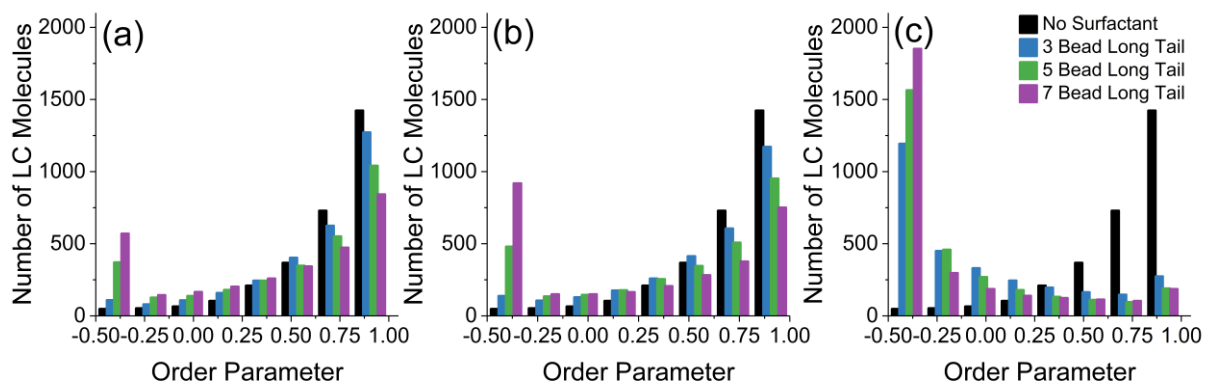


Figure 4.6.1. Number of LC molecules vs. their order parameter with (a) 1000 surfactant molecules where $\alpha_{\text{LC-Stail}} = 25$; (b) 1500 surfactant molecules where $\alpha_{\text{LC-Stail}} = 25$; and (c) 1000 surfactant molecules where $\alpha_{\text{LC-Stail}} = 20$. The legend is the same for (a), (b) and (c).

When 1500 surfactants are present (Figure 4.6.1(b)), the results are similar. As the tail length increases the amount of mesogens in planar alignment decreases (65%, 54% and 42%, respectively), that of mesogens homeotropically aligned increases (12%, 25% and 40%, respectively), and that of tilted LCs decreases (23%, 21% and 18%, respectively). The results are qualitatively consistent with experimental results, which show that when surfactants with short alkyl chain lengths are introduced, LC molecules remain anchored parallel to the interface until the surfactant concentration is so large that the mesogens are dispersed by the surfactants.¹⁹ In addition, these simulation results suggest that when the surfactants have a sufficiently long tail-group, they can promote homeotropic anchoring of the mesogens, and that the effect increases with the surfactant density at the LC – water interface.

The results obtained when the LC – tail repulsion is decreased ($\alpha_{\text{LC-Stail}} = 20$) and 1000 surfactants are on the surface, are shown in Figure 4.6.1(c). As the tail length increases the amount of mesogens in planar alignment decreases (16%, 12% and 12%, respectively), that of mesogens homeotropically aligned increases (65%, 75% and 77%, respectively), and that of tilted LCs decreases (19%, 13% and 11%). These results show that when the repulsion between LCs and surfactant tails is decreased below the self-repulsion parameter, LCs align with the surfactant molecules, which strongly increases the amount of mesogens with homeotropic anchoring.

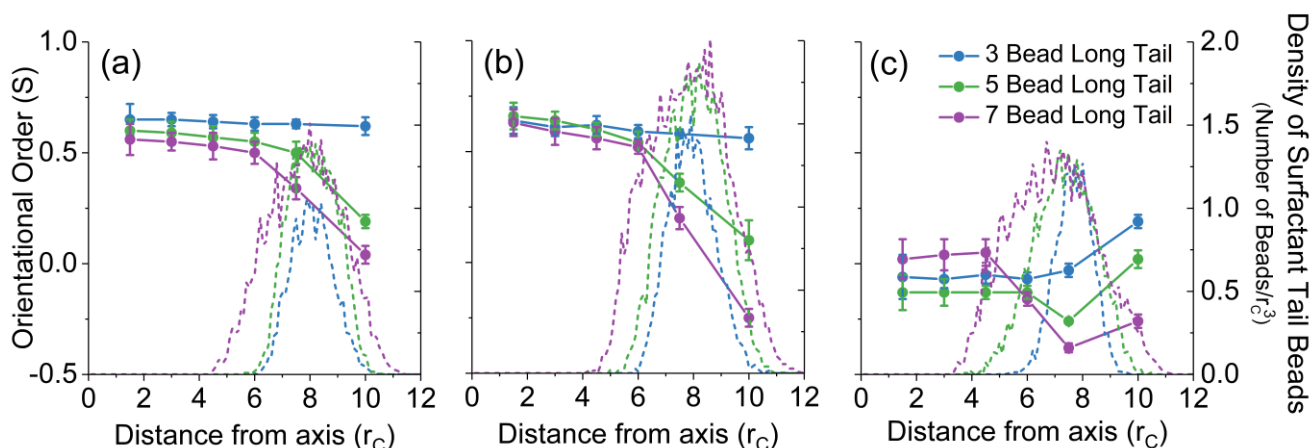


Figure 4.6.2. Orientational order of LCs (lines with symbols) and surfactant density (dashed lines) with respect to their distance to cylindrical axis ($r = 0$) with (a) 1000 surfactant molecules where $\alpha_{\text{LC-Stail}} = 25$; (b) 1500 surfactant molecules where $\alpha_{\text{LC-Stail}} = 25$; and (c) 1000 surfactant molecules where $\alpha_{\text{LC-Stail}} = 20$. The legend is the same for (a), (b) and (c).

Lastly, structural information regarding the LC bridges were provided. In Figure 4.6.2 the order parameter S as a function of the distance from the cylindrical diameter centre was displayed, coupled with the radial density profiles obtained for the surfactant tail-groups. To calculate the density of the tail-groups, each bead in the surfactant tail-group were considered. In Figure 4.6.2(a) the result relative to those discussed in Figure 4.3.1 were displayed. The results show that LCs possess planar orientation at $r \leq 5r$. At larger distances, surfactants interact with LC molecules, and S decreases. In general, the results in Figure 4.6.2(a) corroborate two findings: (i) short tails do not affect the LC orientation at any part of the cylinder; and (ii) as surfactant tail length increases, LCs at the outer surface align homeotropically. The latter observation is due to the physical interaction between surfactant tail-groups and LCs molecules, as suggested by the density profiles of the surfactant tail-groups.

Results relative to those discussed in Figure 4.4.1 are shown in Figure 4.6.2(b). They corroborate to the previous comments, according to which increasing the density of the surfactants is effective in changing LCs anchoring only for those surfactants with long tails. The results shown in Figure 4.6.2(a) and (b) are consistent with the experimental observations reported by Williams et al., who found that for LCs confined in a cylindrical geometry it is possible that the minimum energy configuration corresponds to homeotropic anchoring coupled with LCs oriented parallel to the

cylinder axis near the centre for the cylinder.⁷⁰ Results relative to those discussed in Figure 4.5.1 are shown in Figure 4.6.2(c). These results clearly show the penetration of the change in mesogen orientation due to the surfactants from the interface towards its centre. The LCs order in the core region is isotropic for all surfactants considered, highlighting the importance of LC – surfactant tail interactions in controlling the behaviour of the mesogens.

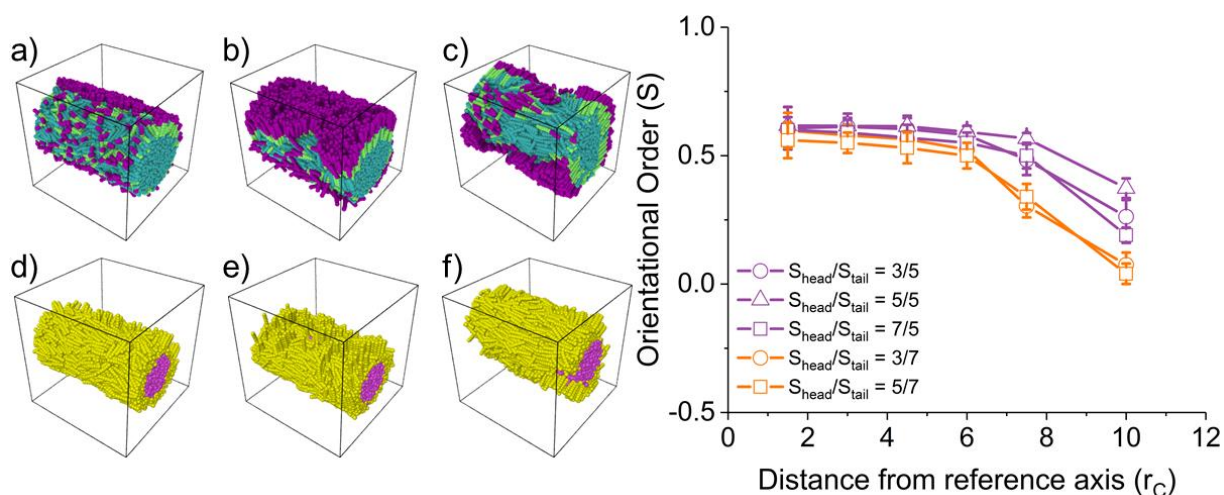


Figure 4.6.3. (Left) Configurations of LC and 1000 surfactant molecules with $S_{\text{head}}/S_{\text{tail}}$ = (a) 3/5 (b)7/5 and (c) 5/7 at 0.7 k_BT. The change in orientation in LCs is due to interactions with surfactants with $S_{\text{head}}/S_{\text{tail}}$ = (d) 3/5, (e) 7/5, and (f) 5/7. LCs that are located in the core of cylindrical radius ($r \leq 5 r_c$) are shown in pink, the rest in yellow. (Right) Orientational order as a function of position.

One final note would be on the effect of the surfactant head length. It has been reported previously that the length of the surfactant head-group does not measurably affect the overall orientation of LCs.¹⁹ The simulations in this thesis show that the overall length of the surfactants affect the time required for achieving lateral phase separation among the surfactants adsorbed at the LC – water interface, but that the head-group length does not significantly affect LCs orientation. To test whether this was the case in these systems, I simulated three systems with 1000 surfactant molecules, in which the surfactant $S_{\text{head}}/S_{\text{tail}}$ beads are 3/5, 7/5 and 5/7, respectively as shown in Figure 4.6.3.

It was found that the surfactant models with same tail length gave similar results, despite of differences in head-group length, as shown in Figure 4.6.3. Therefore, throughout this work the focus was given to changes in anchoring with respect to tail-

length by keeping the overall surfactant length at 10 beads. In the next chapter, I utilized same surfactant models to identify their behaviour on LC droplets. It was anticipated that due to the elastic energy stored in LC molecules in spherical confinement, results would be different than the cylindrical formation of LCs.

CHAPTER 5

SPHERICAL CONFINEMENT OF LCS AND THEIR INTERACTIONS WITH SURFACTANTS*

This chapter provides an understanding for LC behaviour confined in a nanodroplet and their interactions with other chemicals such as surfactants. Molecular simulations are used to quantify the LC order as a function of droplet size. DPD approach is implemented to observe the properties of LC systems at length- and time-scales larger and longer, respectively, than those accessible via atomistic simulations, although smaller than those accessible to continuum theory calculations. The length scale of the study fits in between the two extremes identified by Tomar and co-workers,³⁹ who showed that when a certain anchoring strength is applied to mesogens at the surface of a LC droplet, ordering (radial or bipolar) depends on the droplet size. A droplet can be large enough for the total ordering driving force to be bulk-induced, or small enough for it to be surface-induced. In these systems, it is expected that surface effects are dominant; such effects could be manipulated by the presence of surfactants that preferentially adsorb at the LC droplet – water interface.

5.1 NEMATICITY IN LC DROPLETS

It is known that LC nanodroplets dispersed in a medium will eventually coalesce.¹⁰⁷ To study the properties of LC nanodroplets of different sizes, individual droplets were prepared as initial configurations dispersed in model water. Prior simulations for the LC model considered here showed that, in the bulk, the reduced temperature of 0.7 $k_B T$ was sufficiently low to provide nematic order, and high enough to allow for molecular motion.

*The results given in this chapter were published in Soft Matter with following reference: Z. Sumer and A. Striolo, "Effects of droplet size and surfactants on anchoring in liquid crystal nanodroplets", Soft Matter, 2019, 15, 3914-3922. The original manuscript has been rearranged to conform to the format requirements of the dissertation.

All simulations were performed in the NVT ensemble, and one integration time corresponds to 14.9 ps. Configurations were recorded for 10^6 steps (last 0.149 μ s of the simulations) after droplets were stabilized. Within these 10^6 steps of simulation production, data are collected in every 10^4 steps and averages of 100 frames are used for quantitative analysis. To ensure that the simulations were properly equilibrated, a minimum of 2×10^6 steps were used to equilibrate the systems containing single droplets. The number of steps was determined based on similar studies in literature;^{148, 149} it was confirmed that equilibration had been achieved by noting that once equilibration was completed, the system pressure and energy did not vary, nor did the orientational order. To ensure reproducibility, each system was simulated three times, starting from different initial configurations. Initial configurations were prepared by random distribution of water molecules within the simulation box, and random distribution of LC molecules in a spherical region. Confining LC molecules within a spherical region initially, provided a faster droplet formation and avoided possible cylindrical or flat arrangements caused by periodic boundary conditions.

During the parametrization it was desired to achieve conditions at which mutual solubility between LCs and the water medium was low. As shown in Appendix A, simulations confirmed that (i) at 1.0 $k_B T$ the LC molecules in droplets are not dissolved in water and remain isotropic; and (ii) when the repulsion parameter between water and LC beads was reduced from 50 to 30, dissolution occurred at 0.62 $k_B T$. Therefore, the conclusion was that setting the repulsion parameter at 50 described limited mutual solubility at the conditions chosen for this study, and the rest of the repulsion parameters are the same with the ones provided in Table 4.1, with $\alpha_{LC\text{-}Stail} = 25$ only.

Once the LCs are organised in nanodroplets, it is not known how the nematic-to-isotropic transition temperature changes with droplet size. To quantify this, 5 LC droplets of different sizes were modelled. Representative snapshots for these droplets are shown in Figure 5.1.1(a-e). Each droplet contains a different number of mesogens. The radius of each LC droplet was determined by calculating its radius of gyration (r_{gy}).¹¹⁶ The radii of the 5 nanodroplets were calculated as (a) 6.2 r_c , (b) 9.7 r_c , (c) 13.6 r_c , (d) 16.9 r_c , and (e) 21 r_c , respectively, which correspond to \sim (a) 4.75, (b) 7.43, (c) 10.42, (d) 12.95, and (e) 16.08 nm, respectively. These droplets are composed of (a) 500, (b) 2000, (c) 6000, (d) 13000 and (e) 23000 LC molecules, respectively. The snapshots in Figure 5.1.1 were obtained at the reduced temperature of 0.6 $k_B T$. In

these simulations, only LC mesogens and water beads were simulated. The simulation box size varies from $30 \times 30 \times 30$ to $50 \times 50 \times 50 r_c^3$, depending on the nanodroplet size. To identify the transition temperature, these five systems were simulated within the temperature interval of $0.6 - 0.7 k_B T$, every $0.02 k_B T$, for a total of 30 simulations (each validated 3 times).

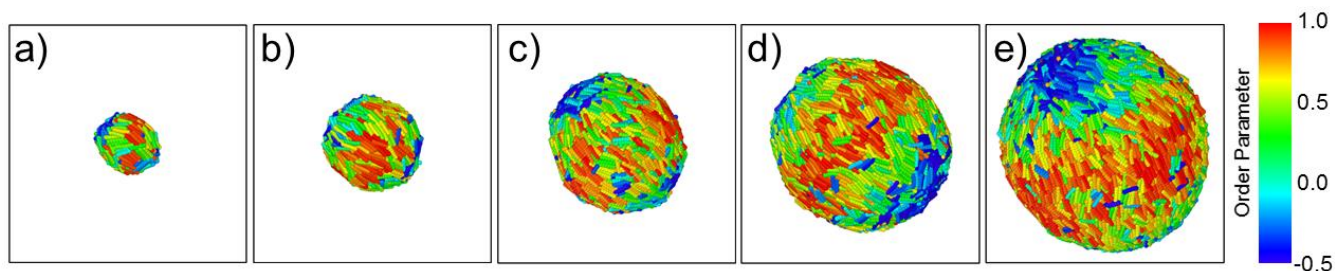


Figure 5.1.1. LC droplets with radii of (a) 4.75, (b) 7.43, (c) 10.42, (d) 12.95, and (e) 16.08 nm, respectively, dispersed in water at $0.6 k_B T$. Water beads are not shown for clarity. Rods are colour-coded by their order parameter, calculated with respect to the directional axis.

The simulation results were used to generate the orientational phase diagram shown in Figure 5.1.2(a). The results show that the transition temperature from nematic to isotropic phase changes as the nanodroplet radius varies. It is important to note that as the size of droplet decreases, molecular aggregates are eventually obtained. In a previous simulation study, it was considered that 1720 mesogens yield a nanodroplet.¹⁰⁷ Using this number as a threshold, all the systems considered here, except the one in Figure 6.1(a), is a nanodroplet. Results obtained when 500 mesogens aggregate are nevertheless useful to provide a complete overview of the systems considered here, although they are affected by relatively large uncertainties.

At $0.6 k_B T$, all droplets simulated here show nematic phase, with S between $0.50 - 0.63$. For the droplets of radii 6.2 and $9.7 r_c$, transition to isotropic phase is observed above $0.64 - 0.66 k_B T$. At $0.7 k_B T$ these droplets possess a fully formed isotropic phase, with $S = 0.22 \pm 0.06$ and 0.33 ± 0.05 , respectively. For larger spherical droplets, the nematic – isotropic transition is observed at temperatures higher than $0.66 - 0.68 k_B T$. To put these results in perspective, it should be remembered that, due to the scale of the simulations, LC orientation in the systems considered here is driven by the surface energy. This implies that the mesogens anchor planarly to water molecules at the interface. It is also helpful to relate the results just discussed to those

obtained for LCs in cylindrical structures. Prior results for such systems show that, although temperature and density are the same, cylindrical LC structures yield higher orientational order than spherical nanodroplets, regardless of the radius. For instance, at 0.7 k_BT, in cylindrical LC structures, $S \sim 0.53$,¹⁵⁰ while in the spherical droplets considered in Figure 5.1.1, S is at most 0.38 ± 0.02 . This is a consequence of the director alignment preference along the axis of the cylinder.

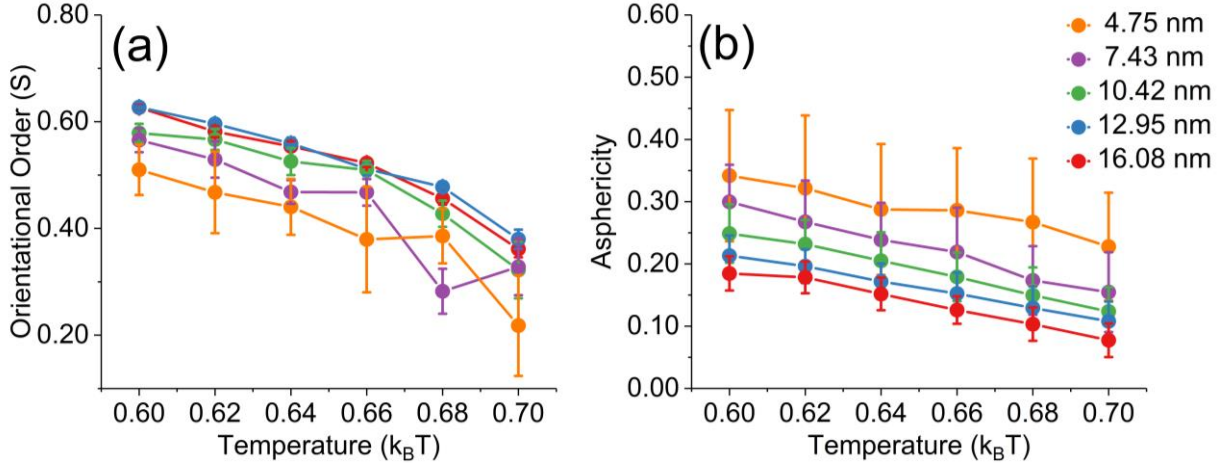


Figure 5.1.2. (a) Orientational order parameters (S) of spherical LC droplets with respect to temperature. (b) Asphericity of LC droplets with respect to temperature. Error bars are obtained as one standard deviation from the average of values derived from 100 frames for each data point. Legend is the same for both (a) and (b).

Visual analysis of the LC nanodroplets suggests that their shape is not spherical, but rather elongated. To quantify the deviation from spherical shape I measured the asphericity¹⁵¹ of each droplet as a function of temperature. When the asphericity is 0, the shape of a droplet is spherical. The maximum value asphericity can assume is 1, in which case the droplet is extended in one dimension.¹⁵² The asphericity was calculated by principal moments of the diagonalized gyration tensor:¹¹⁶

$$\tau_{gyration} = \frac{1}{N_{bead}} \begin{bmatrix} \sum x_i^2 & \sum x_i y_i & \sum x_i z_i \\ \sum x_i y_i & \sum y_i^2 & \sum y_i z_i \\ \sum x_i z_i & \sum y_i z_i & \sum z_i^2 \end{bmatrix} \quad (5.1)$$

$$\tau_{gyration}^{diag} = \begin{bmatrix} \lambda_1^2 & 0 & 0 \\ 0 & \lambda_2^2 & 0 \\ 0 & 0 & \lambda_3^2 \end{bmatrix} \quad (5.2)$$

$$Asphericity = \lambda_1 - \frac{1}{2}(\lambda_2 + \lambda_3) \quad (5.3)$$

where N_{bead} represents number of beads in the droplet, x_i , y_i , and z_i represent the Cartesian coordinates of the bead i with respect to the centre of droplet, and $\lambda_1^2 \leq \lambda_2^2 \leq \lambda_3^2$. Note that all beads have the same size and mass in DPD simulations. The asphericity ranges between 0.08 – 0.34 for all the systems considered in Figure 5.1.2(a), which means that the nanodroplets are only approximately spherical, unless the temperature increases [see Figure 5.1.2(b)]. It is likely that increasing temperature reduces the interfacial tension and increases the flexibility of the mesogens, resulting in more spherical droplets. The results in Figure 5.1.2(b) also show a decrease in asphericity as the radius of the droplet increases. This was expected when size ratio between a single LC molecule and the droplet decreases. Indeed, it would be challenging for few LC molecules within a molecular aggregate (i.e., a few hundred mesogens) to form a perfectly spherical droplet due to their rod-like morphology, which was due to low molecular flexibility. Once the droplet radius was 21 r_c , the droplets tend to be spherical. Increase in droplet radius also contributed to lower values in standard deviation because there were more molecules collectively improving the sphere formation, as a result the error bars became smaller in Figure 5.1.2(b).

The results in Figure 5.1.2 were helpful to select the conditions at which to quantify the effect of surfactants on the properties of the LC nanodroplets. Specifically, a droplet chosen for subsequent studies must be in nematic phase and it must be large enough to distinctly separate core and surface of the droplet. For the following analysis, the nanodroplets considered contain 6000 mesogens, so that the conditions are well above the threshold at which molecular aggregates would form, rather than nanodroplets.

5.2 SURFACTANTS' ADSORPTION ON LC DROPLETS

On the nanodroplet of radius 13.6 r_c (10.42 nm), the effect of surfactants adsorption were investigated. This droplet is large enough to differentiate core and surface. The simulations were conducted at 0.62 $k_B T$. The temperature is low enough to obtain nematic order within the droplet, low enough to ensure low mutual solubility between LCs and water, and high enough to allow for molecular mobility. In the DPD formalism implemented, random forces are included to mimic Brownian dynamics, achieved by

adding a Gaussian white noise to the forces.¹²⁶ It is expected that, because of this random force, the system can escape from local minima in the free energy landscape. Because it was previously noted that the absence of random forces would eventually stop the motion within the simulation box.¹⁵³ To ensure reliability of the results, each system is simulated at least three times. Molecular models were explained in detail in Chapter 3.2 of this thesis. In all cases considered here, 1000 surfactant molecules were added to the 6000 LC molecules, yielding 14 mole %. Representative equilibrated simulation snapshots are shown in Figure 5.2.1.

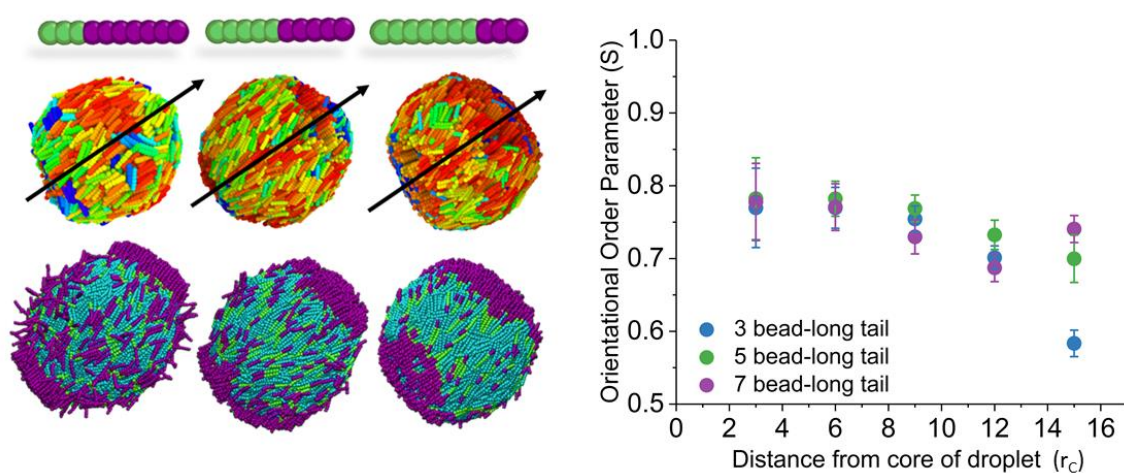


Figure 5.2.1. (Left) Equilibrated simulation snapshots for LC nanodroplets of radius $13.6 r_c$ (10.42 nm) covered with low concentration of surfactants. From left to right, the surfactants have tail-groups of 3, 5, and 7 beads, respectively. The simulations are conducted at $T = 0.62 k_B T$. In all cases, water beads are not shown for clarity. In the top panels, only LC mesogens are shown, also for clarity. (Right) Orientational order of LC molecules shown with respect to their distance to the core of the droplet for every $3 r_c$.

Simulation snapshots show that the surfactants self-assemble at the droplets boojums, regardless of the tail length. At the tips there is a larger concentration of LC – water interfacial defects (boojums), which increases locally the interfacial tension.¹⁵⁴ The surfactants clearly adsorb in these locations to reduce the total system energy. The adsorption of the surfactants caused a change in orientation of the LC mesogens located at boojums of the droplets, which became oriented perpendicularly to the interface due to homeotropic anchoring, and as a consequence the droplets became uniaxial. This is reflected in the overall orientational order parameter of these droplets. Without surfactants, the nanodroplets with radius $13.6 r_c$ (10.42 nm) were characterised by an order parameter $S = 0.57 \pm 0.02$. In the presence of 1000

surfactants, S increased to 0.65 ± 0.02 , 0.73 ± 0.03 and 0.72 ± 0.01 , for surfactants 3-, 5-, and 7-bead-long tails, respectively.

To quantify the range of interactions due to surfactant adsorption, the order within LC molecules was studied within core and outer regions. The core was considered within a radius of $7 r_c$ from the centre, the outer region at distances larger than $12 r_c$. The core region was considered as a droplet and not a small aggregate, as discussed for Figure 5.1.2, it was large enough for order quantification. It is expected that surfactants would directly affect the outer region, close to the interface. In fact, after the surfactants adsorb the droplet size increases from 13.6 to $15 r_c$. LC molecules located (based on their centre of mass) further than $12 r_c$ are considered to be part of the outer region. A transitional region could be defined between $7 - 12 r_c$ from the droplet centre. The order of LC molecules, shown in Figure 5.2.1, was also quantified with respect to their distance to the core of the droplet. The radial configuration was never achieved, probably because of the high orientational order maintained within the core region.

Figure 5.2.1 shows that the surfactants have a stronger effect in the LC orientation within the outer region. When no surfactants are present, $S = 0.40 \pm 0.02$ in this region. When the surfactants are present, especially for surfactants with long hydrophobic tail groups, more LC mesogens at the boojums became parallel to the direction vector. The S parameter in the outer region became 0.55 ± 0.02 , 0.69 ± 0.04 , and 0.74 ± 0.02 , for surfactants with 3-, 5-, and 7-bead-long tails, respectively. S in the core regions was not affected much by the surfactants. For all cases, with or without surfactants, $S = 0.77 \pm 0.02$ in the core of the nanodroplet. As already mentioned, due to the size of the droplets considered here, LC orientation is surface driven. In other words, interactions between water molecules and LC droplet surface yield a surface force larger than the elastic forces within LC molecules, yielding planar anchoring of LC mesogens with the surroundings. The surfactants affect the interfacial energy, reducing the appearance of boojums, but this contribution is always local.

To quantify changes in nanodroplet shape, the droplet asphericity was calculated. Only the LC mesogens were considered for this calculation. Adding surfactants with 3- or 5-bead-long tails decreased the asphericity from 0.23 ± 0.04 to 0.08 ± 0.03 and 0.09 ± 0.04 , respectively. On the other hand, adding surfactants with

7 bead-long tails did not affect asphericity, which remained $\sim 0.20 \pm 0.04$. This is due to the deformation at the droplets boojums described above.

5.3 EFFECT OF SURFACTANT CONCENTRATION

Because only the surfactants with 7-bead-long tail-groups were able to deform the LC nanodroplets upon adsorption at the droplets boojums, these surfactants were chosen to investigate the effect of surfactant concentration. Their number within the simulation box was increased from 1000 to 1500 for the 6000 LC molecules, which yields a concentration of 20 mole %. The snapshots of the equilibrated structures are shown in Figure 5.3.1. Visual inspection suggests that the LC nanodroplet surface is almost fully covered by surfactants, the droplet is clearly deformed at the surface, and the surfactants seem to form ordered domains that yields the droplet shape from being spherical to be faceted. Quantification of order shows that S decreased to 0.27 ± 0.04 . Perhaps more interesting is to point out that in the droplet outer region S decays to zero, because the LC mesogens in this region assume almost every orientation with respect to the direction vector. The mesogens at the nanodroplet core show the same overall orientation as those in the droplet with no surfactants.

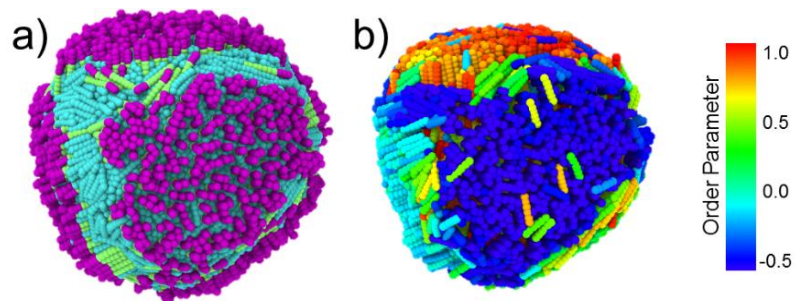


Figure 5.3.1. (a) LC nanodroplet of radius $13.6 r_c$ (10.42 nm) covered with high concentration of surfactants whose tail-group is of 7 beads. No water beads are shown for clarity. (b) Same as (a), but without surfactants, for clarity. LC molecules are colour-coded with respect to their order parameter. The simulations were conducted at $0.62 k_B T$.

Comparing the results in Figure 5.3.1 to those in Figure 5.2.1, when few surfactants are present, they self-assemble at the droplet boojums regardless of their molecular features. When the surfactant concentration increases, the entire droplet surface can be covered by surfactants, at the expense of a deformation of the droplet. In this event, the LC mesogens at the outer region become perpendicular to the

interface, whereas those in the core remain parallel to the direction vector. Although it is difficult to suggest a direction in this particular droplet, the direction vector was obtained by the same protocol as other droplets: getting the average direction of molecules by post-processing the simulation results, for every frame that was considered.

These observations constitute deviations from predictions from the continuum theory, according to which, due to predefined boundaries and interactions at the interface, droplet shape deformation cannot be predicted. These differences are due to the ability of simulations to account for individual mobility of the LC molecules, as well as for their elastic properties, such as rigidity and their interaction with water beads under certain thermodynamic conditions (a direct consequence of the model implemented). While at contact with water the LCs assume a parallel orientation, the presence of surfactants can change this orientation to perpendicular. However, the effect is local, as the LC orientation near the droplet centre remains planar. Quantifying how these observations affect practical applications is the subject of future research.

5.4 COALESCENCE OF MULTIPLE SURFACTANT-COVERED DROPLETS

Apart from surfactants causing homeotropic anchoring, it is important to analyse whether the surfactants are able to stabilize LC nanodroplets in water. For this analysis surfactants with 7-bead-long tails were considered. Two simulations were conducted: (i) droplets covered with 1000 surfactants, and (ii) droplets covered with 1500 surfactants. In both cases, eight LC droplets were simulated in water. The initial configurations are shown in Figure 5.2.1(e) and Figure 5.3.1(a), respectively, and they were replicated within a larger simulation box: each having the size of $80 \times 80 \times 80 \text{ r}_c^3$ which corresponds to $61.3 \times 61.3 \times 61.3 \text{ nm}^3$. The simulations were then conducted for 5×10^6 steps, which correspond to $0.745 \mu\text{s}$. The results are shown in Figure 5.4.1, where the initial configurations (left) and the snapshots after $0.745 \mu\text{s}$ (right) were identified.

1000 surfactant molecules were not enough to cover the entire LC droplet surface, and instead the surfactants agglomerated at the droplet boojums. The simulations confirmed that for this system agglomeration was inevitable: in $0.745 \mu\text{s}$, the 8 initial droplets yield 4, two of which maintained their initial size and shape, two of which the result of 2 initial droplets coalescing, and 1 of which the results of 4 initial

droplets coalescing. As two LC droplets merge, they yield larger and more spherical droplets, in qualitative agreement with results in Figure 5.2.1. Perhaps interestingly, as the droplets become wider, the surfactants are found to distribute more evenly on the droplet surface. This is because as the droplet size increases, the surface to volume ratio decreases, and the surface density of the surfactants anchored to the surface increases.

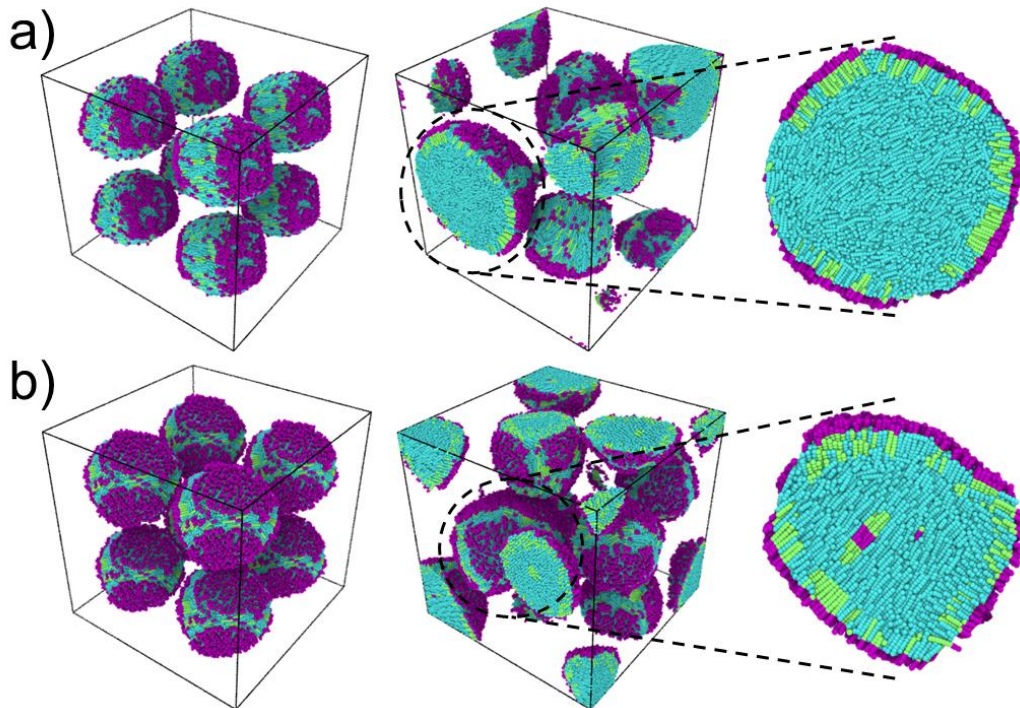


Figure 5.4.1. Eight LC nanodroplets, each covered with (a)1000 and (b)1500 surfactant molecules with 7 bead-long tails at (left) 0 μ s and (right) 0.745 μ s. On the far right, an enlargement of the cross-section of largest droplet obtained, (a) \sim 24 r_c radius and (b) \sim 19 r_c radius.

When the number of surfactants is increased to 1500, droplets agglomeration occurs more slowly. After 0.745 μ s of simulations only two pairs of droplets merged, yielding 6 LC droplets. The surfactants are found to be more effective at delaying droplet agglomeration because they cover the entire LC droplets surface. It might be interesting to point out that when two LC droplets merge in this situation, the resultant droplet remains deformed. As can be seen from the cross section in Figure 5.4.1(b), the resultant droplet is not spherical, and some of the surfactants remain trapped inside it after agglomeration.

Because of computer power limitations, it is hard to confirm whether the final snapshots shown in Figure 5.4.1 correspond to the equilibrated system. Analysis of energy profiles suggest that the systems have reached metastable conditions at which long-lived structures have been achieved (they did not change for 0.298 μs), but it is indeed possible that further agglomeration will occur. As the droplet size increases and the surface to volume ratio decreases, the surfactants will cover more and more of the droplet surface, and perhaps will be able to stabilise LC droplets. Experimentally, small LC droplets are used in PDLC applications, where they are trapped within polymer matrix where agglomeration is more difficult than in emulsions.^{100, 101}

The shape of the LC droplets depends on the surfactant coverage, but also on the droplet size. When the surface to volume ratio is high, and the surfactant surface density low, surfactants accumulate at the boojums. For such droplets, as the surfactant concentration increases, the droplet is deformed. However, when the surface to volume ratio is low (i.e., large droplets), it is possible that increasing surfactants concentration will not result in deformations of the droplet. In the next chapter, I investigated how nanoparticles (NPs) manipulate LC ordering in droplets, instead of surfactants. For the following analysis, a single size of droplet (13.6 r_c) was chosen. The chapter describes whether NP self-assembly deformed the shape and orientation of LC droplets, suggests a way forward with respect to the size, shape, and chemical functionality of NPs for e.g., utilization of LC droplets as NP templates.

CHAPTER 6

NANOPARTICLE SELF-ASSEMBLY ON LC DROPLETS*

In this chapter, the collective self-assembly of nanoparticles (NPs) adsorbed on nanodroplets were investigated. Both LC and oil nanodroplets are considered, although the discussion focuses on LC droplets. The LC nanodroplets act as templating agents, on which homogeneous and Janus NPs of various geometrical features are adsorbed. The quantitative analysis reveals that the cumulative orientational order of LC nanodroplets does not significantly change. Bipolar droplets preserve the planar anchoring with the surrounding water beads. Yet, there is a strong evidence for LC droplets acting as templates and dominate the positional and orientational preference of nanoparticles with respect to their size, shape, and chemical composition upon their self-assembly.

In the first part of the work 100 small NPs of the same type are added to a water – LC droplet system for each simulation, for which the results are provided in Chapters 6.1 and 6.2. The LC droplet to NP volume ratio is ~2500 for these calculations. After investigating the collective effect of multiple nanoparticles on a LC droplet surface, the analysis was conducted with single large particles in Chapter 6.3. The LC droplet to NP volume ratio is ~90 for the systems discussed in Chapter 6.3. Because of computing power limitations, only 1 NP adsorbed on one LC nanodroplet was studied. Focusing on a single NP offers the added benefit of more clearly identifying size-dependent properties for NP – droplet self-assembly, as emergent phenomena such as those highlighted for small NPs, which might appear should multiple NPs be simulated, could hinder the interpretation of the simulation results. By systematically

*The results given in this chapter were published in Molecular Systems Design & Engineering with following reference: Z. Sumer and A. Striolo, "Nanoparticles shape-specific emergent behaviour on liquid crystal droplets", Mol. Syst. Des. Eng., 2020, 5, 449-460. The original manuscript has been rearranged to conform to the format requirements of the dissertation.

investigating NPs of different shapes and chemical features (i.e., homogeneous vs. Janus), results highlight the ability of LC nanodroplets to template the preferential adsorption of particles depending on NPs size, shape, and surface properties. Details of NP models were provided in Chapter 3.2. The system containing the LC droplet immersed in water was characterised in Chapter 5.1. For the present chapter, droplets of radius $13.6 r_C$ were chosen.^{155, 156}

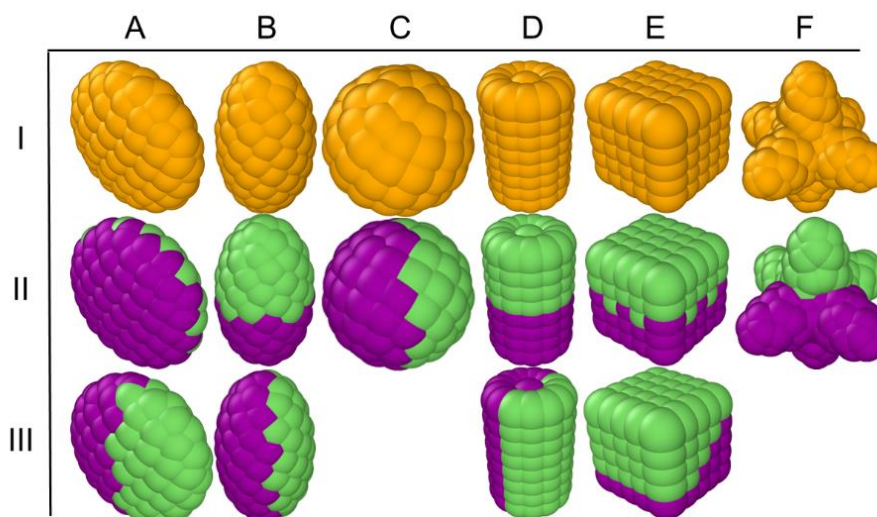


Figure 6.1. NPs simulated in this work. Homogeneous NPs are described by beads of a single type (type I NPs, top row), while Janus NPs are composed of two bead types. For several NPs it is possible to generate Janus NPs of two different structures (type II and type III, respectively, in middle and bottom row). Refer to the text for details regarding the DPD interaction parameters implemented.

The NVE ensemble was implemented, with integration time $\Delta t = 0.01 \tau$, corresponding to ~ 14.9 ps.¹⁵⁵ Each simulation run included 3×10^6 steps, the last 10^6 of which were considered part of the production run, and were used for analysis. In other words, out of the $0.447 \mu\text{s}$ of each simulation, the last $0.149 \mu\text{s}$ were considered for generating the results presented here. During the production phase, one system configuration (i.e., one frame) was recorded at $0.0149 \mu\text{s}$ intervals, yielding 100 frames for system. The protocols implemented for data collection were described in previous chapter.¹⁵⁵ For pulling/pushing of NPs (described in Chapter 6.3) the software PLUMED¹⁵⁷ was used.

The NPs considered are shown Figure 6.1, and they are named based on the row and column within which they are located in that figure. To conduct these simulations, disc (A), ellipse (B), sphere (C), rod (D), cube (E) and star (F) NPs were

added to simulation boxes in which one nanodroplet was pre-equilibrated. For each NP, homogeneous (type I) and Janus NPs were considered; in some cases, two types of Janus NPs were prepared for a given NP shape (type II and III, respectively). In total, 16 NPs of similar volumes and bead densities were prepared. The NPs shown in yellow (Row I in Figure 6.1) were described by moderate repulsive interactions with both water beads and LC beads. In this case, NP – water and NP – LC interactions were described by $\alpha_{\text{NP-LC}} = \alpha_{\text{NP-water}} = 35 \text{ k}_B\text{T}/r_c$. For Janus particles (Rows II & III in Figure 6.1), the conservative repulsive forces were increased between the medium and corresponding side of nanoparticle. Explicitly, purple (hydrophilic) NP beads interacted with water and LC beads via potentials described by $\alpha_{\text{hphillic-water}} = 25$ and $\alpha_{\text{hphillic-LC}} = 50 \text{ k}_B\text{T}/r_c$, respectively; green (hydrophobic) NP beads interacted with water and LC beads via interactions described by $\alpha_{\text{hphobic-water}} = 50$ and $\alpha_{\text{hphobic-LC}} = 10 \text{ k}_B\text{T}/r_c$, respectively. The DPD parametrization is completed by imposing $\alpha_{ij} = 50 \text{ k}_B\text{T}/r_c$ among beads of different type and $25 \text{ k}_B\text{T}/r_c$ among beads of the same type. This parameterization ensures conditions of low mutual solubility between LCs and water.¹⁵⁵ Each system was simulated three times with different initial configurations. Equilibration was considered achieved when the same density profiles on the droplet surfaces were observed.

6.1 SELF-ASSEMBLY OF SMALL NANOPARTICLES

This section covers how the collective assembly of 100 small NPs changes with respect to their shape and chemical functionality, although the size of the NPs that are shown in Figure 6.1 is similar to each other. For example, while one small spherical homogeneous particle does not show preferential adsorption on specific LC nanodroplet locations, 100 spherical nanoparticles preferentially agglomerate at the nanodroplet boojums, providing evidence of emergent behaviour. On the contrary, Janus spherical nanoparticles do not show such a strong emergent behaviour. Cylindrical NPs manifest the opposite trend: while homogeneous nano cylinders do not exhibit orientational order on the LC nanodroplet, Janus ones either locate at the LC nanodroplet boojums or orient towards the direction vector of bipolar droplets.

The system density was $3.03 \pm 0.01 \text{ bead}/r_c^3$, the temperature was between $0.62 - 0.63 \text{ k}_B\text{T}$ and the pressure was $17.10 \pm 1.17 \text{ k}_B\text{T}/r_c^3$. These small differences in temperature and pressure were caused by the difference in the rigid structures (NPs)

in the systems. In these simulations, the fluid was characterised by pressures and temperatures of $20.66 \pm 0.08 k_B T / r_c^3$ and $0.62 k_B T$, respectively.

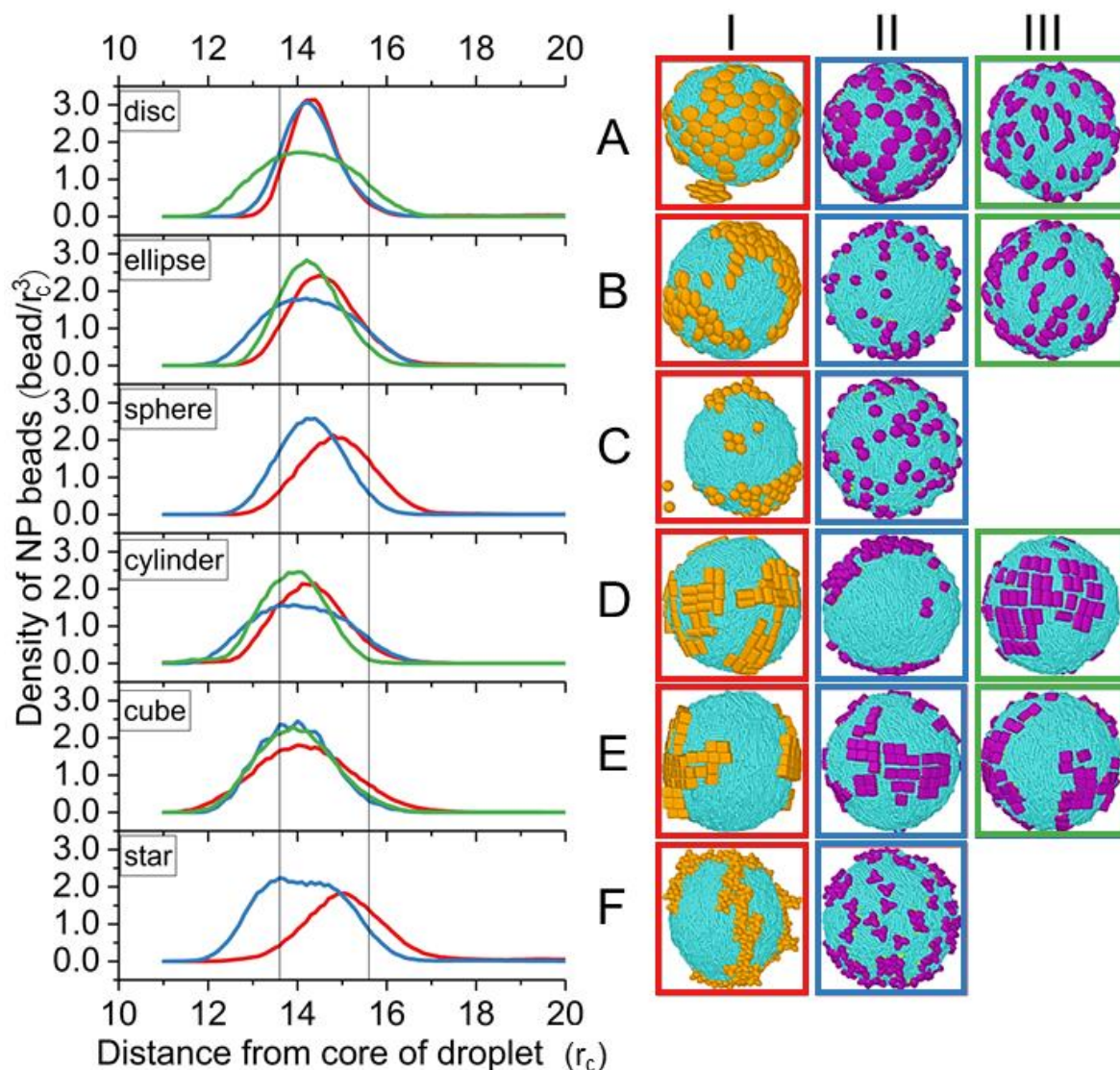


Figure 6.1.1. Left: Density profiles of NP beads with respect to distance from the droplet core. Lines in graph indicate the interface, located at radial distances in the range between $13.6 - 15.6 r_c$. Right: Corresponding snapshots of LC droplets. Coordinates for the various systems summarised in this figure were provided in Appendix B.

In Figure 6.1.1, right panels, the last frame of each simulation for each of the simulated systems were represented, to provide a visual summary of the results. To quantify the results, the density profile of the NPs centre as a function of the distance from the centre of the LC nanodroplet were computed. The results are reported on the left panel of Figure 6.1.1. In this representation, the LC nanodroplet surface is located at radial distances $13.6 - 15.6 r_c$ from the nanodroplet centre. This region is identified

in Figure 6.1.1 by two vertical lines, which allows to compare results on different systems.

6.1.1 SPHEROID NANOPARTICLES

Spheroid NPs include discs (group A in Figure 6.1) and ellipsoids (group B). Considering discs, during simulations it was observed that some A.I NPs, which were not adsorbed at the LC/water interface, assembled on top of each other and created a colloidal aggregate that then attached to the nanodroplet. The other A.I particles adsorbed homogeneously at the LC nanodroplet surface. No strong evidence of accumulation at the boojums was obtained, as perhaps the NP – NP interactions overcome the driving forces due to the LC orientation on the nanodroplet. When the discs were described as Janus NPs (A.II NPs), the behaviour was similar to that of the homogeneous NPs, except that the aggregation in solution did not occur, likely because of the preferential interactions along specific directions among such NPs. When Janus NPs of type A.III were simulated, preferential orientations were observed on the LC nanodroplet, with shape-dependent entropic forces likely causing preferential alignment among the A.III NPs.

A previous report revealed that entropic patchiness enables directional bonding on nanoparticle systems, which is coherent with findings presented here.⁴³ Packing in colloidal suspensions of anisotropic hard particles is dependent on entropic forces, for minimizing the free energy of the system.^{158, 159} The entropic patchiness, therefore, stands for the preferential direction of the particles caused by their shape.^{160, 161} A directional preference was not observed when the A.III NPs adsorbed on oil droplets, confirming that the mesogens and their ordered structure were responsible for this feature. Although the NPs in the two simulations (LC vs. oil) possess similar density profiles, the disordered oil molecular structure did not yield sufficient entropic effects to drive NPs alignment, as shown in Appendix B. The directional forces due to the LC mesogens within the nanodroplet are effective for A.III NPs because these particles penetrate deeper into the LC self-assembled structure. While chemical patchiness enabled all the NPs considered here to adsorb at the surface, the entropic patchiness caused by a combination of NP shape and LC mesogen rigidity is probably responsible for the preferential direction. These effects result in orienting almost all the A.III NPs adsorbed on the LC nanodroplets parallel to the droplet direction vector.

The results obtained for prolate ellipsoids (see group B NPs in Figure 6.1) are also shown in Figure 6.1.1. It was observed that homogenous ellipse particles (B.I) were not homogeneously distributed on the droplet surface. They rather form surface clusters within which the NPs remain parallel to the droplet direction vector. Experimental data showed that spheroids with different aspect ratios yield honeycomb structures on two-dimensional surfaces.¹⁶² Honeycomb structures were observed in simulations as well. Additionally, NPs oriented along the direction of LC molecules in the droplet. These results suggest that the orientation of the ellipsoids adsorbed on the LC nanodroplets could be manipulated by the preferred orientation of the mesogens. In the simulations, the droplet boojums function as poles and the ellipsoidal NPs are distributed on the droplet surface as compass needles. This feature, however, is lost when Janus spheroidal NPs are considered (i.e., see B.II NPs in Figure 6.1). The latter NPs were observed to be randomly distributed over the droplet surface. Since these NPs are adsorbed normal to the droplet surface, their orientation could not be quantified. Due to deeper penetration within the droplet surface, B.II NPs show a wider peak in the density profiles shown in Figure 6.1.1, because of density fluctuations in the radial direction. Ellipsoidal B.III NPs, on the other hand, manifest similar orientation as the B.I NPs, although B.III NPs do not assemble in clusters as B.I NPs tend to do. Consequently, the density profiles obtained for B.I and B.III NPs are similar, and narrower than those obtained for B.II NPs. Ellipsoidal B.III NPs are oriented parallel to the direction vector of the LC droplet, similar to the results described for A.III NPs. This is further evidence that shape dependent entropic forces yield a patterned alignment that does not exist when the B.III NPs adsorb on oil droplets.

6.1.2 SPHERICAL NANOPARTICLES

The simulations for spherical NPs (group C) yield results different compared to those described for spheroid NPs. In particular, homogeneous spherical NPs, C.I, agglomerated into clusters at the LC nanodroplet surface. When compared to the simulations obtained on oil droplets, the results in Figure 6.1.1 suggest that the LC caused the spherical NPs to accumulate within the boojums. It is also interesting to highlight that, within these clusters, the NPs are arranged hexagonally, both on the LC and on the oil nanodroplets. In fact, similar hexagonal arrangements were reported by Rahimi et al. in a previous continuum mechanics analysis of the packing of multiple spherical NPs on a LC droplet.⁴¹ Such results were explained by the expected larger

elastic energy density near the poles of the bipolar droplets. While the simulations here agree with this observation, the fact that different NPs yield different arrangements suggests that the NP morphology is also important for the NPs to accumulate in these high energy density regions. It has been proven both experimentally¹⁶³ and computationally⁹⁶ that the NP size is also an important parameter for driving the NPs to accumulate on the LC surface defects. In fact, when a single small spherical C.I NP adsorbed on one LC nanodroplet was modelled, (not shown here for brevity) did not show preferential adsorption location for the single NP on the LC nanodroplet. However, as shown in Figure 6.1.1, when 100 small spherical NPs were present, they collectively assembled on the boojums, suggesting that emerging phenomena are also important for driving the self-assembly of NPs on LC droplets. Comparing density profiles such as those shown in Figure 6.1.1, left panels, obtained on LC nanodroplets and on oil nanodroplets, differences were observed, suggesting that shape dependent forces caused C.I NPs to be located further away from the droplet core when LC molecules were present.

The simulation results in Figure 6.1.1 also show, contrary to the expectations, that for Janus spherical NPs (type C.II in Figure 6.1), neither clustering nor preferential localization at the boojums occurred. This was observed both on LC and oil droplets, in both of which the density profiles were also similar. These observations suggest that effective NP – LC interactions at the droplet could strongly affect the NPs self-assembly, perhaps overcoming the energetic and entropic advantages of accumulating on the boojums. It is perhaps interesting to observe that, for small spheroidal (discs and ellipsoids) and well as for small spherical NPs, NPs clustering was achieved when the NPs were chemically homogeneous, and that in all cases honeycomb structures were obtained, which is coherent with previous findings.^{41, 93, 162} Due to more attractive NP – LC interactions than NP – NP ones, spherical Janus NPs distributed rather uniformly on the droplet surface. In the following sections I quantified the behaviour of NPs that yield local smectic domains on the LC nanodroplet surface: cylindrical and cubic NPs.

6.1.3 NANOPARTICLES WITH FACETS

Cylindrical, rod-like, homogeneous NPs (particles D.I) adsorbed on LC nanodroplets generated smectic structures with no preferential direction, as can be seen in Figure

6.1.1. These results seem in good agreement with experimental results obtained for rod-like NPs adsorbed on a hexadecane droplet,¹⁶⁴ suggesting that the LC molecules did not exert a templating effect on these NPs. Therefore, it was anticipated that rod-like NPs would assemble yielding similar structures on both LC and oil nanodroplets. On the contrary, Janus rod-like NPs (type D.II in Figure 6.1) exhibited a different behaviour. Just like homogeneous spherical C.I NPs, D.II NPs accumulated at the LC droplet boojums. Due to their aspect ratio, cylindrical D.II NPs behave like rod – coil di-block copolymers and adsorb preferentially on high energy surface locations (i.e., the boojums). The corresponding homogenous D.I NPs, with the same aspect ratio, behave differently because they cannot penetrate the droplet surface, due to the different interaction potentials implemented. Indeed, in Chapter 5.2 it was shown that short rod – coil copolymers preferentially move towards boojums of LC droplets.¹⁵⁵

When cylindrical Janus NPs had their two faces vertically separated, as in D.III NPs, they preferentially adsorbed on the LC droplets equator, rather than the boojums. Although they have the same aspect ratio as D.II NPs, their morphology caused a much shorter attractive region on the LC nanodroplet, and the D.III NPs could not penetrate the droplet surface. In this case, the LC molecules clearly acted as templating agents, and directed the NPs to be parallel to the droplet direction vector. The templating properties of rigid LC molecules cause the preferential orientation for D.III NPs, just as they did for A.III NPs. As in the case of A.III NPs, these results were ascribed to entropic patchiness of D.III NPs. However, it should be noted that this alignment was not observed for D.I NPs. The combination of these results suggests that moderate attraction between LC mesogens and rod-like NPs (D.I) did not induce ordering, and the NPs clustered on the droplet surface with no preferential orientation. Contrarily, highly attractive interactions caused D.II NPs to penetrate through the droplet surface and accumulate at the droplet boojums. The Janus D.III NPs, on the other hand, oriented parallel to the LC molecules.

Homogeneous cubic NPs (particles E.I in Figure 6.1) yield clusters on the LC nanodroplet surface. These NP clusters preferentially locate on the equator, similarly to what was observed for cylindrical D.I NPs. However, because, as opposed to nanorods, E.I particles have equal length in all directions, the preferential orientation they exhibit cannot be ascribed to their anisotropic shape. Glotzer and co-workers reported that perfect spherical particles prefer to assemble within the fcc crystal structure,

whereas perfect cubes prefer simple cubic structures.⁴³ The same behaviour was observed on LC droplets, with cubic NPs yielding clusters on the droplet surface that arrange in a simple cubic form.

Janus cubic particles (E.II and E.III NPs) yield smaller clusters than those formed by E.I NPs, but the behaviour is similar. Although E.II NPs are cubically faceted and E.III NPs are tetrahedrally faceted once they became Janus NPs, they did not exhibit strong differences in their surface alignment. Morphological differences between E.II and E.III NPs did not cause any observable difference among the NP self-assembled structures, as can be seen in Figure 6.1.1.

The analysis reveals that NPs with facets, e.g., cylinders and cubes, achieve local smectic clusters on the LC nanodroplet surface. This is consistent with literature reports, in which experiments were conducted to study the self-assembly of gold nanorods with high aspect ratio,¹⁶² and that of 2D perovskite nanoplatelets.¹⁶⁵ In addition to what was available in the literature, the simulation results here suggest that the interactions with LC molecules, which create the driving forces, determine where NPs accumulate on the surface of LC nanodroplets. The NPs morphology on the other hand, creates the entropic forces that dictate whether NPs self-assemble yielding a directional order. As it was previously reported, entropic patchiness plays a contribution towards the preferential orientation of NPs, where the enthalpic interactions are the dominating force.⁴³ This explains why LC molecules do not always affect location and orientation of NPs, but can act as a template under specific conditions.

6.1.4 BRANCHED NANOPARTICLES

Star-shaped NPs (Group F in Figure 6.1) are the only branched NPs considered in this work. Homogeneous star-shaped particles were introduced to the LC droplet as in Figure 6.1.1, E.I. NPs. Two behaviours were observed: the particles either move towards the boojums and accumulate there or entangle with each other. E.I NPs created wire-like structures adsorbed on the LC droplet. These structures are driven by entropic forces, because the enthalpic forces such as low affinity towards LC molecules keeps the NP – LC interaction low, enabling shape dependent NP – NP interactions to be the decisive driving force for self-assembly. As a result, shape

dependent 2D wires were obtained on the LC droplet. The effect of high LC affinity is evident when Janus E.II NPs are considered in Figure 6.1.1. Due to stronger effective attraction between LC – NP, NP – NP interactions were comparatively weak, dispersing the NPs on the LC droplet surface with no preferential adsorption location. Similar results were obtained for ellipsoidal B.II and spherical C.II Janus NPs.

The results summarised in Figure 6.1.1 showed that enthalpy driven molecular mechanisms drive the NPs to be preferentially adsorbed at the LC nanodroplet boojums, or in other locations. Perhaps a quantitative validation could be made by comparing the free energy of two different systems where NP is in two different spots (preferred location and elsewhere), which is beyond the scope of this chapter. It is worth pointing out that small NPs with the same shape can yield different behaviour due to morphologically different LC-attractive regions exposed on their surface. Most homogeneous NPs considered here show similar behaviour when they are adsorbed on LC droplets as they do on flat LC interfaces. For example, they yield smectic alignment or honeycomb structures, depending on their morphology. In addition, some of the NPs considered here show preferential adsorption on the LC droplets equatorial regions and do not move towards the boojums, even though the topological defects are accumulated at the boojums. Bead-to-bead interactions between nanoparticles and LC molecules are important in determining the preferential NPs adsorption location on the droplet surface, as the NPs size and shape are. When moderate attractions are present, NPs may or may not preferentially adsorb on the droplet's tips (this is evident for homogeneous NPs). When strong attractions are present, NPs might prefer to assemble side-to-side with LC molecules, yielding parallel orientation along the LC droplets meridians. In such situations, it appears that NP – LC interactions dominate size and shape effects. Namely, once the enthalpy driven preferential adsorption occurs, entropic forces affect the NPs orientation. This effect is very distinct on elongated NPs (e.g., ellipsoidal, and cylindrical ones, as well as Janus discs), which orient along the droplets directional vector.

6.2 NPS' EFFECTS ON LC MESOGENS' SELF-ASSEMBLY

In this section, how NP assemblies affect the orientation of LC mesogens within the droplets were investigated. The properties of LCs in the absence of NPs were quantified in Chapter 5.1. In summary, LC molecules in water formed a droplet that is

bipolar and in the nematic phase. The droplet size chosen for this study was small enough to allow for meaningful simulations to be completed, yet larger than a molecular cluster. The temperature used in the present simulations was chosen so that the droplet was nematic, yet with sufficient molecular mobility to achieve equilibrated systems.¹⁵⁵

To quantify how the NPs affect the LC orientation, in Figure 6.2.1 the probability distributions of LC molecules with respect to their location within the nanodroplet and order parameters were pictorially shown. The algorithm for the calculation of the order parameter is defined in Chapter 3.3. For reference, Figure 6.2.1 reports results obtained for the LC nanodroplet with no adsorbed NPs, so that the effect of NPs adsorption can be quantified by comparison. For brevity, Figure 6.2.1 only considers NPs from group I in Figure 6.1, i.e., homogenous NPs. This is because the results are similar to those reported in Figure 6.1.1 for the correspondent homogeneous NPs and are provided in Appendix B. Analysis of the simulation results shows that the NPs have a slight impact on the order of the LC mesogens. When such effect is observed, it always remains local, specifically on the droplet surface, i.e., NPs adsorption does not affect the LC order throughout the whole droplet. At the core of the liquid droplets, almost no LC molecule show an order parameter lower than 0.4 in any of the systems considered. This indicates that all LC molecules in nematic phase almost formed smectic structures. Moving towards the nanodroplet surface, the results suggest that most of the LC mesogens remain parallel to the direction vector, although the number of LC molecules that are tilted or perpendicular increases from core to surface. These results are similar for all the nanoparticle types considered. Exceptions were observed for D.I and E.I NPs (cylinders and cubes, respectively), in which case, the results suggest that the LC – NP interaction caused formation of smectic domains of LC mesogens on the nanodroplet surface. In fact, the results in Figure 6.2.1 suggest that these NPs cause a slightly higher probability of observing the order of 1.0 near the droplet surface. As explained above, entropic effects probably cause the NPs to interact with the LC mesogens, in qualitative agreement with observations from the literature,¹⁶⁶ and the results suggest that a synergistic phenomenon is taking place, with the NPs orienting because of the LCs, but vice versa, the NPs also templating further LC alignment.

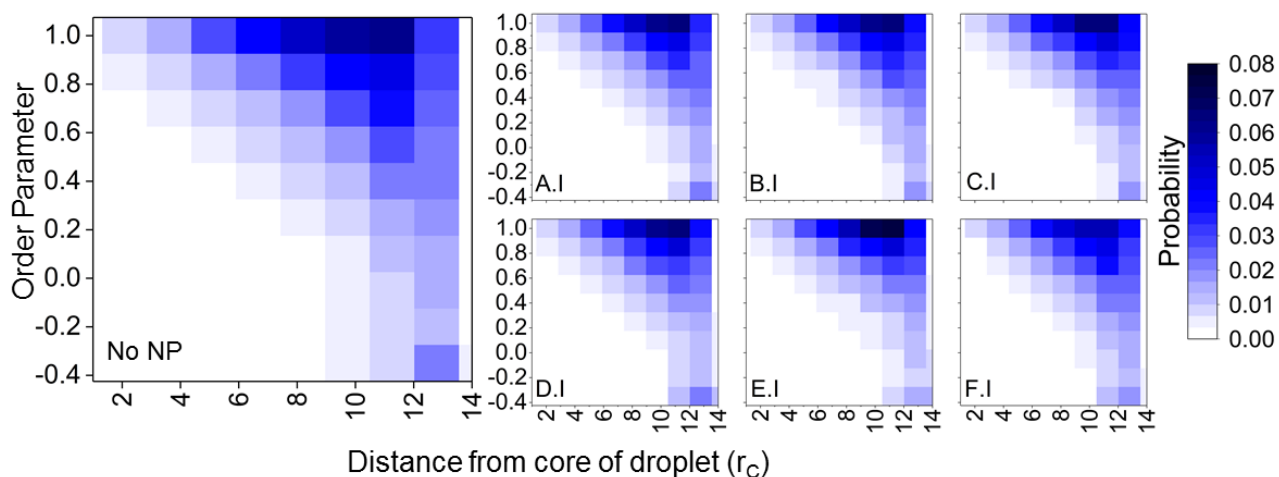


Figure 6.2.1. Probability distributions of LC mesogens with respect to their locations and order parameters, for pristine LC droplets and for LC droplets that were exposed to group I NPs, as shown in Figure 6.1.1. Similar results for group II and III NPs are provided in Appendix B.

The global orientational order for all LC droplets considered in Figure 6.2.1 varies between 0.55 – 0.63, as indicated in Figure 6.2.2(a). These results suggest that all droplets are in nematic phase. Upon NP adsorption, the LC droplets remain bipolar, although slight deformations were observed. The droplets with adsorbed NPs showed shapes ranging from perfectly spherical to slightly elongated droplets. To quantify the droplets deformation, the asphericity was calculated. The asphericity quantifies the shape deviation from a perfect sphere, with 0 denoting such a perfect sphere.¹⁵⁵ Asphericity values are given in Figure 6.2.2(a). The asphericity of the droplet with no NPs adsorbed was 0.23 ± 0.04 . The highest asphericity value was obtained for LC droplets with adsorbed E.I NPs (i.e., 0.28 ± 0.03) followed by LC droplets with adsorbed D.I NPs (i.e., 0.22 ± 0.02). For the reasons that were explained in Figure 6.2.1, the E.I and D.I NPs have stronger interactions with the LC droplets, resulting in droplets deformations. The smallest LC droplet asphericity was observed when star-shaped NPs (F.I) adsorbed, yielding an asphericity of 0.14 ± 0.03 . In general, when NPs other than those with facets adsorb, the asphericity of the LC droplet decreases compared to values obtained for the LC droplet with no NPs.

Colour-coded maps were provided in order to relate the change in order parameter with respect to the location of the LC molecules on the droplet, in Figure 6.2.2(b). The results show that by moving from the equator to the boojums of the droplets, the orientation changes from parallel to perpendicular, with respect to the

direction vector of each droplet. The red-to-yellow portion of the droplet represents the mesogens that are almost parallel to the direction vector, located in the equatorial region. The blue – purple rods, mostly located near the boojums, represent the mesogens that are almost perpendicular to the direction vector, pointing to the droplet tips. Such assembly is consistent with planar anchoring with water molecules, as reported previously.⁹⁶ Some of the results in Figure 6.2.2(b), for example those for A.I and D.I NPs, show that some LC mesogens locally changed orientation from parallel to perpendicular in the equatorial region. This is the local effect due to NP adsorption.

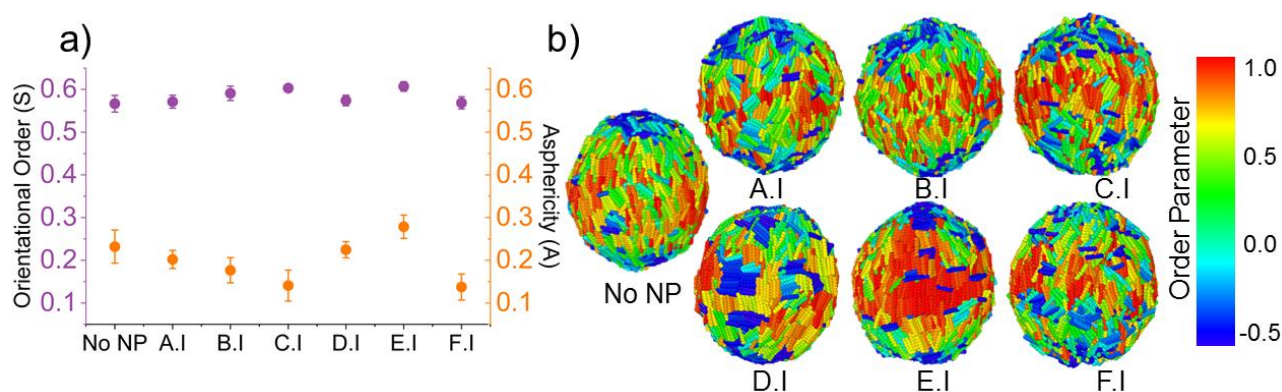


Figure 6.2.2. (a) Orientational orders (purple) and asphericity (orange) and (b) map of LCs on droplets colour-coded by their order parameter that were exposed to Group I nanoparticles. Group II and III are provided in Appendix B.

No significant change occurred in the orientation of the LC molecules upon NP adsorption, although slight shape deformations took place, as described in Figure 6.2.2(a). Li et al., surveying experimental results, suggested that often liquid crystalline ordering is insensitive to colloidal assembly, although this is not the case when the NPs are able to penetrate into LC droplets.⁹⁴ Results in this chapter are consistent with this observation, as the simulated NPs affect the orientation of LC molecules locally, but this effect is not strong enough to change the global orientational order within the droplets.

6.3 EFFECT OF NP SIZE

The results presented in Chapter 6.1 and 6.2 were obtained for NPs whose size is comparable to the length of one LC mesogen (*small* NPs in the nomenclature implemented herein, referring to Chapter 3.2). When multiple NPs adsorb on one LC

droplet, emerging phenomena can occur, depending on the NP features, with, in some cases, preferential adsorption sites and alignment between adsorbed NPs being observed. Because previous research revealed that spherical nanoparticles preferentially locate at the boojums of biaxial LC droplets if they are large enough,⁹⁶ in this section the effect of NP size was systematically investigated. NPs whose features are shown in Figure 6.1 were simulated, maintaining the same aspect ratios used to prepare the NPs simulated in Figure 6.1.1, yet increasing the NP size three times along each dimension. The results presented here were obtained for systems with density $2.85 \pm 0.002 \text{ bead}/r_c^3$, temperature $0.62 \text{ k}_B\text{T}$, and pressure $19.94 \pm 0.03 \text{ k}_B\text{T}/r_c^3$.

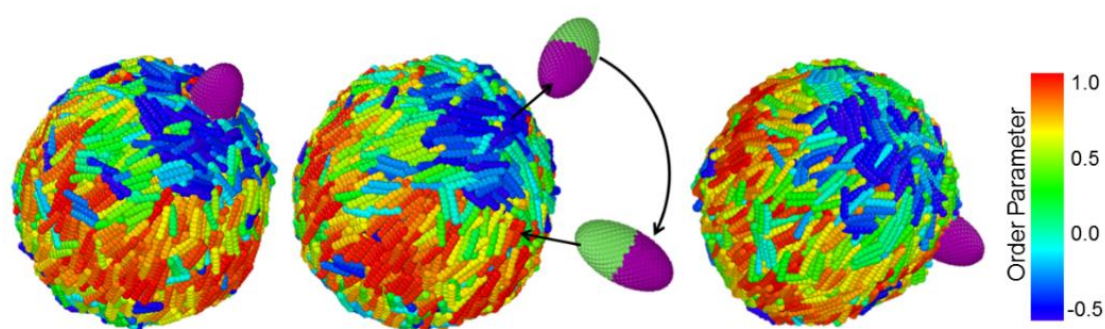


Figure 6.3.1. Schematic representation of the algorithm implemented to test whether the DPD simulations discussed below for large NPs adsorbed on LC droplets had reached equilibrium. LC molecules are colour-coded by their order parameter. Further details are provided in the Appendix B.

To ensure that the results presented are representative of truly equilibrated states, an additional analysis was conducted, which are discussed in Appendix B. The algorithm is shown schematically in Figure 6.3.1. From the final configuration obtained from one typical DPD simulation run (left in Figure 6.3.1) a pulling algorithm to desorb the Janus particle from the interface was used. Then, the NP along the aqueous phase was dislocated until it was above a different region of the LC droplet (middle panel of Figure 6.3.1), and it was allowed to adsorb again on the droplet.

Additional equilibrium simulations (3 million additional steps) were then conducted, to test whether the NP would return to the original preferential location (right panel in Figure 6.3.1). This test was conducted for Janus NPs only, and the results suggested that the simulations discussed below had indeed reached equilibrium. The reason only Janus NPs were used for this test was because only these NPs showed preferential adsorption on defined locations on the droplet surface. At the end of the

algorithm summarised in Figure 6.3.1, the NPs that had shown preferential adsorption at the droplet tips (B.II, D.II, and F.II NPs), moved back to the tips after manipulation. The NPs that moderately prefer boojums also moved back towards these locations (A.II, A.III, and C.II). The other NPs remained within the equatorial region of the LC nanodroplets (B.III, D.III, E.II and E.III).

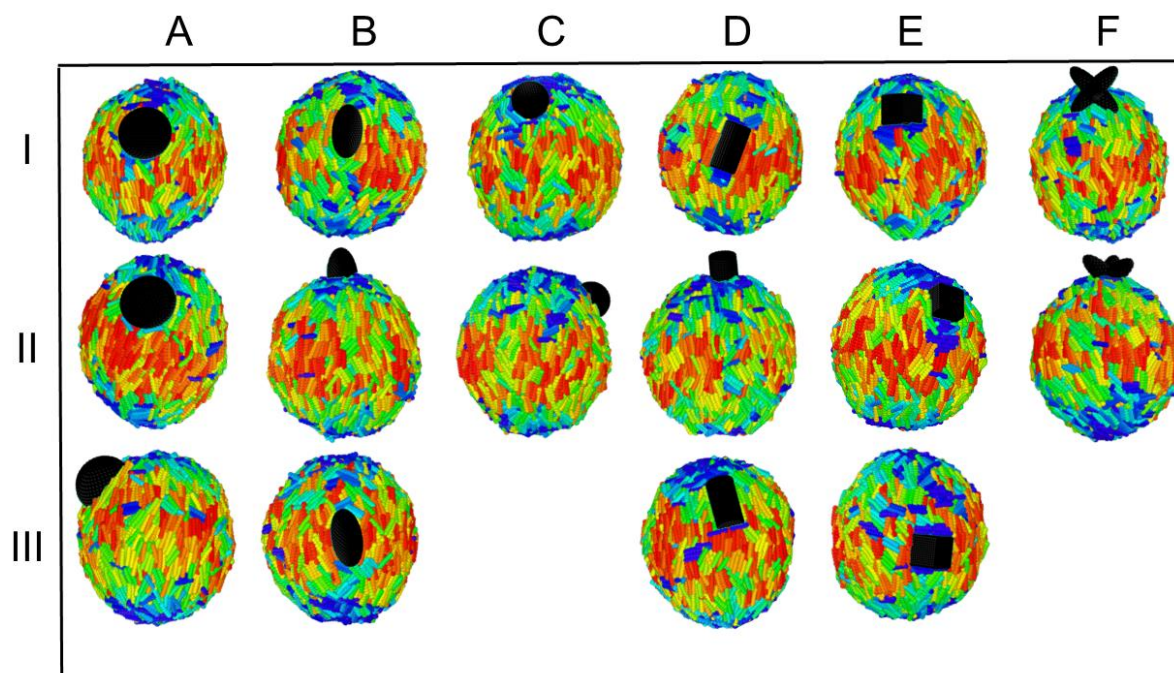


Figure 6.3.2. Simulation snapshots of droplets with large particles, colour-coded LC molecules with respect to order parameters. Each panel title represents the corresponding NP in the notation shown in Figure 6.1. Legend is the same with Figure 6.3.1 for order parameters.

In Figure 6.3.2 the results obtained for the simulation of single large NPs adsorbed on LC nanodroplets are summarised. This figure reports the last frames of simulations, row I shows homogeneous NPs' positions after 3 million steps, and rows II and III show Janus NPs' positions after the additional 3 million steps. Janus NPs moved back to their initial preferred orientation and position (if they had any), after the manipulation. In what follows the results for each NP morphological feature were discussed.

6.3.1 SPHEROIDS AND SPHERES

The simulation results shown in Figure 6.3.2 suggest that the behaviour of group A NPs (discs) strongly depends on the surface chemistry of the NPs themselves. While

homogenous A.I NPs do not show any preferential adsorption site on the LC droplet, A.II and A.III NPs migrate towards the droplet boojums. A.II and A.III NPs did not move to the droplet tips, as could have been expected based on literature observations;^{41, 96} instead, they preferentially locate within a boojum region in which the second order tensors of LC molecules was low. Using a geographical analogy, this region is referred as the arctic/antarctic circles. Such effects perhaps can be explained by the fact that the NPs considered are larger than the droplet tips, and as a result suboptimal conditions would occur should they accumulate there.⁹⁶ It is also possible that, by accumulating at the arctic/antarctic circles, these NPs allow for an optimal organisation of the LC mesogens, which they might otherwise frustrate if they were to accumulate on other regions of the droplet surface.

The results obtained for group B NPs (ellipsoids) show that B.I and B.III NPs are excluded from the polar regions, while B.II NPs preferentially assemble at the droplet tip. Homogeneous B.I and Janus B.III NPs show some preference for the droplet equators. In these positions, the templating propensity of the LC mesogens becomes evident: due to their vertical alignment with respect to the droplet poles, the mesogens contribute to align the NPs along the same direction. These results strengthen the argument of enthalpic forces being the main driving force in directing the organisation of NPs on LC nanodroplet surfaces, with entropic forces providing a contribution, not necessarily dominant, to the driving force. Bead-to-bead interactions described by the DPD parameters for B.I and B.III NPs ensure that B.I and B.III NPs remain on the equatorial region of the LC droplet, while B.II moved towards the boojums. These differences in behaviour were observed even though the NP geometry is the same for these 3 NPs. Entropic forces could not affect the position of B.I and B.III NPs, yet they could change their orientation, which is parallel to the direction vector of the droplet.

The results obtained for group C NPs (spheres) show that these NPs migrate towards the droplet boojums regardless of their surface features (i.e., homogeneous vs. Janus). It is worth noting that neither C.I nor C.II NPs adsorb at the droplet tip, unlike the ellipsoidal NPs B.II. Results indicate that the dimensions of a NP affect its alignment. Elongated particles exhibit similar behaviour as block polymers, which can penetrate through the LC droplet surface and move towards the boojums within certain ranges of attractive interactions between polymers and mesogens.¹⁵⁵ Therefore, if a

particle is long enough to penetrate the surface of a LC droplet, it likely migrates towards its tip. A large NP does not necessarily penetrate the LC surface, yet it can still migrate towards the boojums, but perhaps it remains within the artic/antartic circle rather than reaching the droplet tip.

6.3.2 CYLINDERS AND CUBES

The results obtained from the simulations of large cylindrical NPs can be seen in Figure 6.3.2, group D. Visual analysis suggests a very similar behaviour as that described for ellipsoidal NPs. When the surface properties of the cylindrical NPs were changed, yielding D.II NPs, the NPs preferentially adsorbed on the LC droplet tip. This is in contrast with results obtained for homogeneous D.I cylindrical and Janus D.III NPs, which preferentially adsorbed at the LC droplet equator, which is very similar to the results reported for ellipsoidal B.I and B.III NPs. The driving forces responsible for the behaviour of the ellipsoidal NPs remain the driving forces that drive the self-assembly of cylindrical NPs on the LC nanodroplet. If these NPs are capable of penetrating through the droplet surface, they are then capable to move towards the droplet tips. In addition, if elongated NPs such as cylindrical and ellipsoidal ones are long enough without being too strongly attracted to the LC mesogens, they then preferentially accumulate at the LC droplet equator, where they exhibit a preferential orientation parallel to the direction vector of the droplet. Entropic effects cause this preferential orientation: when enthalpic forces drive the NPs to the equator, shape-specific effects provide driving forces for preferentially orienting these NPs.

None of cube-shaped NPs, as can be seen in Figure 6.3.2, group E, manifested a distinct preferential adsorption site on the LC nanodroplet. Both homogeneous and Janus cubic NPs distributed randomly on the droplet surface. After the detachment/attachment process described in Figure 6.3.1, the cubic NPs simply stayed where they were put back on the droplet surface. Comparing these results to those obtained for elongated NPs clearly quantifies the importance of NP aspect ratio in determining preferential adsorption sites on LC droplets. The cubic NPs considered here did not have sides long enough to penetrate through the droplet surface. Which is a strong mechanism to drive the NPs towards the LC droplet tips. Being equally long in all three directions, could not show a preferential orientation either because entropic

forces were not strong enough, as opposed to results obtained for elongated NPs, just discussed.

6.3.3 BRANCHED NPS

The simulation results obtained for star-shaped NPs (group F) are shown in Figure 6.3.2. Due to the length of their branches, these star-shaped NPs effectively behaved as elongated structures, able to penetrate the LC droplet surface. Thus, these NPs preferentially adsorbed near the boojums. Homogeneous star NPs (F.I) preferentially adsorbed within the artic/antarctic region, while Janus star NPs (F.II) distinctly adsorbed on the LC droplet tip. Analysis suggests that the homogeneous star-shaped large NPs (F.I) behave like spherical NPs (C.I). However, the Janus star-shaped NP (F.II) behaved like ellipsoidal (B.II) and cylindrical (C.II) Janus NPs. Coherent with the discussion above, these results suggest that the strength of bead-to-bead interactions determines the location of the NPs on the LC droplet surface.

The results presented in this chapter suggest that parameters such as shape and attractiveness are equally important as the NP size in determining the preferential adsorption site for NPs on LC nanodroplets. As in the examples of disks (A.I), ellipsoidal (B.I) and cylindrical (D.I) NPs, not all large NPs necessarily move towards the boojums. Some prefer to locate at the equator. The results also show that entropy-driven self-assembly is only possible if enthalpic forces are also in favour of it. Chemical functionalisation yielding Janus structures, for some NPs, can alter the preferential adsorption sites for NPs on LC droplets, which could provide a useful handle to create self-assembled structures with desired morphology and size for a variety of applications.

Perhaps there are many other conditions, e.g., different LC types and confinements, different thermodynamic properties, to be discovered. For this particular modelling, however, detailed analysis of surfactants' and nanoparticles' adsorption on LC droplet surfaces brought the following questions to the attention: what is happening inside the droplet when there is a change in surface anchoring conditions? How are the defects in bulk affected? In order to elucidate LC behaviour inside the droplet, I conducted a multiscale study with different surface conditions and provided the results in the following Chapter.

CHAPTER 7

LC DROPLETS UNDER EXTREME CONFINEMENT*

In this chapter, LC droplets under extreme spherical confinement where both strong planar degenerate and strong homeotropic anchoring were applied on droplet surfaces with different surface distributions were investigated. DPD simulations are complemented by continuum calculations conducted within the Q-tensor approach, via Landau – de Gennes theory, as explained in Chapter 3.4. The combination of the two approaches allowed to map the defects generated by surface alteration and quantify the system energy as a function of the constraints imposed on the LC droplet surfaces. How elastic (splay, twist, bend) and thermotropic energies change in response to confinement were identified. As discussed in Chapter 2, such modelling is highly utilized in literature for understanding of cumulative behaviour of mesogens that form the droplet, and when the droplet formation isn't particularly of interest.^{32, 96}

At the continuum level, using the finite-element method,^{135, 136, 139} a clear map of defects within the droplet as a function of surface anchoring conditions was obtained. A very small size range was chosen to compare findings achieved by simulations (30 nm diameter) and by Q-tensor calculations (0.1 μm diameter). The anchoring was kept strong, so interfacial interactions dominate the ordering within the droplet. The findings were then compared with those obtained for droplets of 1 μm diameter. For calculations of the droplets that are 0.1 μm and 1 μm in diameter, the LC mesogens are described by a Q-tensor field, therefore losing, in part, their chemical identity. Towards the molecular level, coarse-grained DPD simulations¹²⁶ provided detailed information

*The results given in this chapter, *in part*, were published in Nanoscale with following reference: Z. Sumer, F.A. Fernandez and A. Striolo, "Engineered liquid crystal nano droplets: insights from multi-scale simulations", Nanoscale, 2020, 12, 20211-20219. The original manuscript has been rearranged to conform to the format requirements of the dissertation.

regarding the local surroundings. DPD calculations were conducted for droplets of diameter 30 nm. In Chapter 5, asphericity analysis revealed that 30 nm droplets with 16,000 rods can easily be defined as droplets rather than aggregates.¹⁵⁵ Because it was shown that the droplets that are larger than 20 nm in diameter possess acceptable orientational order and asphericity to be considered for further analysis. The aim is to bridge across the scope and capabilities of these two methods. To the best of our knowledge, this is the first time that finite element and molecular models, albeit coarse-grained, yield consistent results for LC applications within a nanocavity of spherical geometry, which will be beneficial for device miniaturization and optimization.

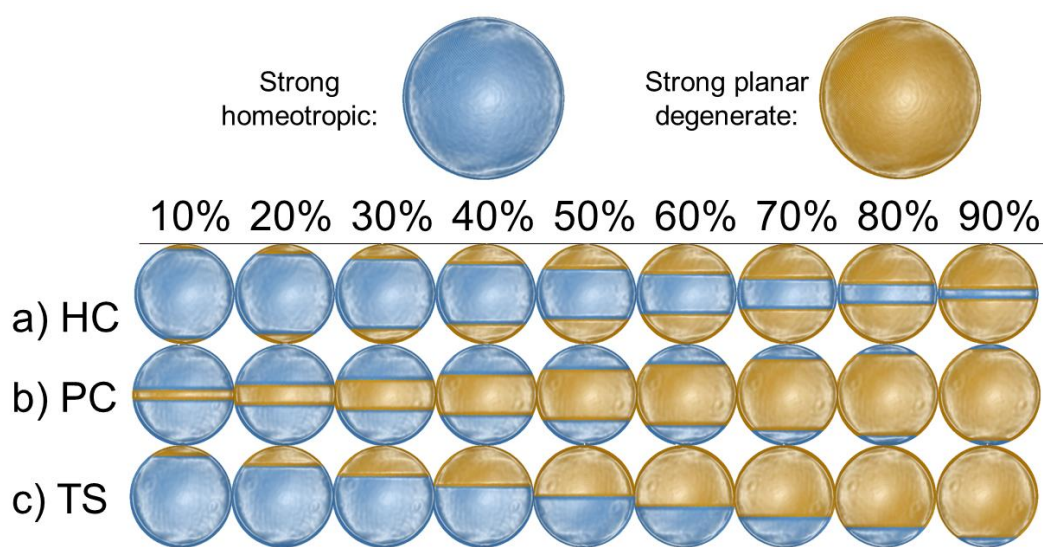


Figure 7.1. Homeotropic and planar degenerate anchoring surface distributions for (a) Homeotropic Centre (HC), (b) Planar Centre (PC) and (c) Two-Sided (TS) droplets. The percent ratios represent the amount of surface on which strong planar degenerate anchoring is enforced on the simulated LC droplets.

The droplet shells used in DPD simulations are shown in Figure 7.1. The shells are categorized based on how they enforce anchoring. In Figure 7.1(a), strong homeotropic anchoring occupies regions of decreasing size centred on the shell equator (Homeotropic Centre, HC). In Figure 7.1(b), strong planar degenerate anchoring occupies regions of decreasing size centred on the shell equator (Planar Centre, PC). In Figure 7.1(c), shells enforce planar degenerate and homeotropic anchoring from the two poles, with different size ratios (Two-Sided droplets, TS). In these simulations, the shells were forced to remain in the middle of the simulation box throughout the run, therefore periodic boundary conditions were not necessary.

For DPD simulations, each of the shells shown in Figure 7.1 contains 20,000 beads arranged in a hollow sphere formation. Inside each one of them, 5,000 inert beads, and 16,000 rods were inserted. Figure 7.2(a) shows a representative snapshot (PC type droplet with 40% planar degenerate anchoring) for the initial configurations used in the DPD simulations. The shells yield fully homeotropic anchoring (blue) or fully planar degenerate anchoring (orange). Initial configurations were created by random distribution of LC and water molecules inside the shell. No mass transfer was allowed through the shell walls. In Figure 7.2(b), corresponding mesh structure for Q-tensor calculations is shown. In order to compare DPD results with Q-tensor calculations, LC model was modified in this chapter. The tips of the rod-like structures have a different affinity toward the surrounding shell compared to the core to achieve the desired anchoring. DPD parameters for the modified model is provided in Figure 7.2(c).

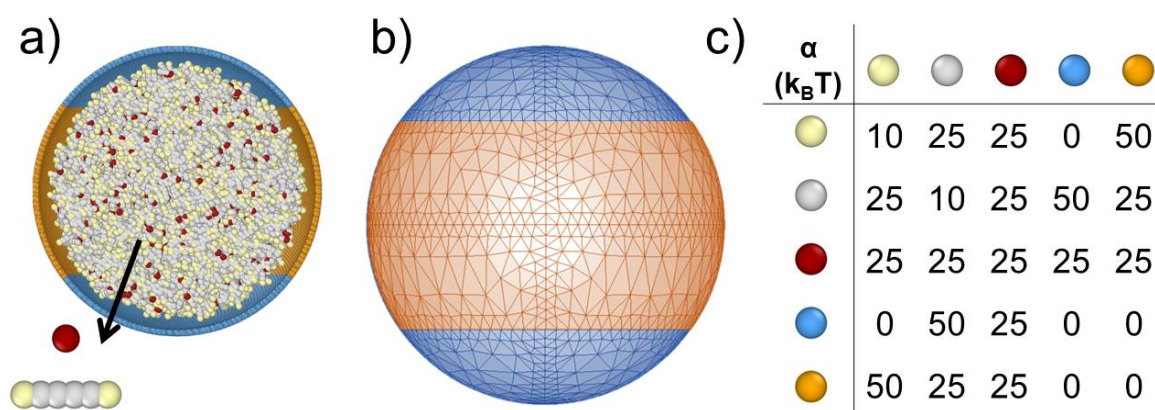


Figure 7.2. (a) Initial configuration of DPD simulations, cut through to visualise the LC mesogens inside the spherical shell. Red, yellow and light grey beads represent the inert beads, tip and body of LC molecules, respectively. (b) Schematic representation of mesh structure used in Q-tensor simulations. Both panels are for PC type droplet with 40% planar degenerate anchoring on the surface, chosen as an example. (c) DPD parameters used in this chapter.

DPD simulations were performed in the NVE ensemble. Validation simulations in Figure 7.3 are run for 6×10^6 steps, with integration time $\Delta t = 0.01 \tau$. Thus, simulations were conducted for at least $0.9 \mu s$, with the last $0.15 \mu s$ used for data analysis. To ensure reproducibility, each system was simulated three times, with different initial configurations. The rest of the simulations, provided in Figure 7.1.1, were conducted for $0.30 \mu s$, with the last $0.15 \mu s$ used for data analysis. Because the 1000 data points collected in the last $0.15 \mu s$ showed that enthalpy and the potential

energy of the systems did not change, DPD simulations were considered to be had reached equilibrium. The systems were kept at $0.5 \text{ k}_B\text{T}$. A $50 \times 50 \times 50 r_C^3$ simulation box was used where the shell has the diameter of $40 r_C$, corresponding to $\sim 30 \text{ nm}$. The Q-tensor calculations are iterated until the largest change in Q-tensor value was below five significant digits, which satisfied the minimum energy criteria.

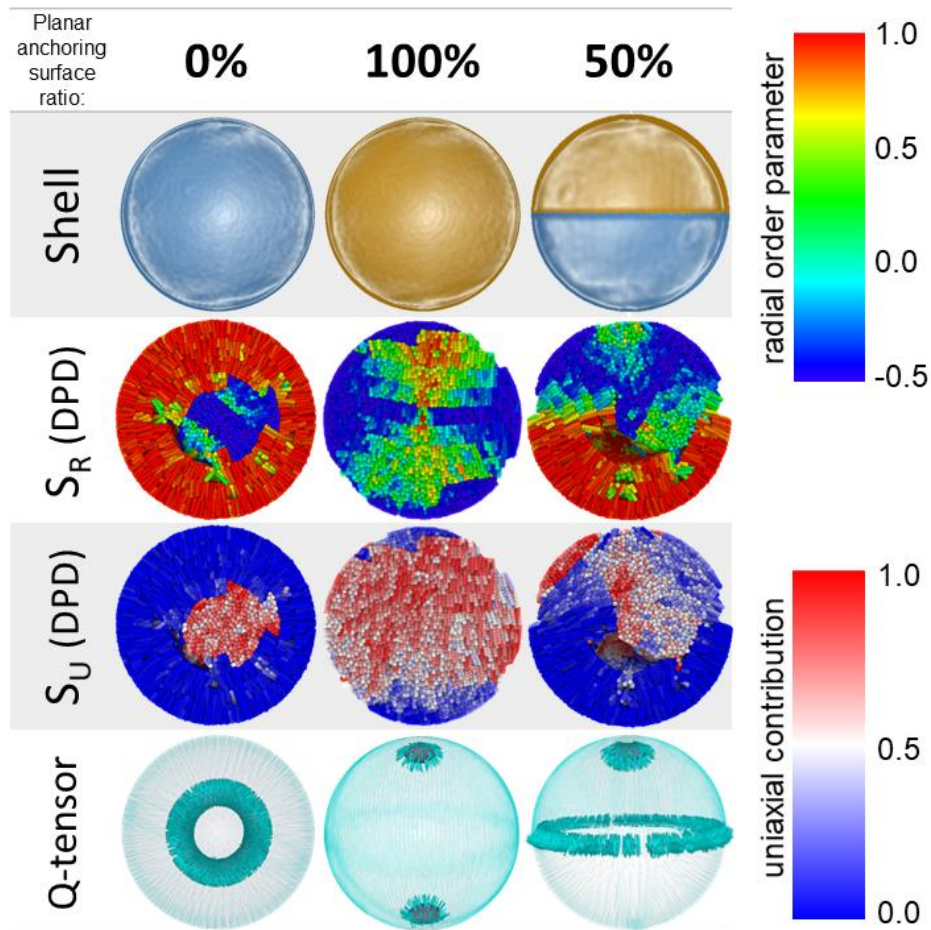


Figure 7.3. (Top) Three droplet shells with different anchoring surfaces, homeotropic (blue) and planar degenerate (orange). (Middle) Colour-coded LC molecules with respect to S_R (up) and S_U (down). (Bottom) Snapshots of simulations performed by the finite-element method with emphasis on defect structures, the images show surfaces of constant order for a low value of S (see Chapter 3 for details).

Validation of the proposed computational approach was achieved on three systems, as shown in Figure 7.3. The results in this figure are organised column by column. The first column represents the results obtained for a LC droplet on which fully homeotropic surface anchoring was imposed. The second column shows a LC droplet

on which fully planar degenerate anchoring was imposed. The results show that the former droplet assumed a radial order, while the latter assumed a bipolar order. Throughout this manuscript, the terms planar degenerate and homeotropic anchoring will be used to represent surfaces that (by itself) impose bipolar and radial configurations within the droplets, respectively, consistent with reports from the literature, in particular the pioneering work of Volovik and Lavrentovich.^{41, 167-169}

The ratio of imposed planar degenerate anchoring surfaces on the droplets were used to name their configurations. For example, 0% planar degenerate anchoring represents a droplet on which homeotropic anchoring was imposed on the entirety of its surface, whereas 50% planar degenerate anchoring represents a droplet on which homeotropic anchoring was imposed on half of its surface (the rest being planar degenerate anchoring). The third column summarises the results obtained for a LC droplet in which the two anchoring conditions are both present yet divided into two equal hemispheres. In the continuum approach, the surface of the LC droplet was represented as two different surfaces. These surfaces show strong anchoring to yield planar degenerate or homeotropic anchoring (see Chapter 3.4 for details). In the DPD simulations, a shell around the LC droplets was built, which interact with the LC mesogens via different repulsion parameters provided in Figure 7.2(c), optimised to yield anchoring consistent with the continuum model. For consistency, I refer to planar degenerate and homeotropic anchoring conditions also when discussing the DPD results.

7.1 ORIENTATIONAL ORDER ANALYSIS

For the three columns in Figure 7.3, global orientational order parameters from the DPD simulations were calculated via the protocol suggested by de Pablo and co-workers.³⁸ Radial (S_R) and uniaxial order (S_U) were distinguished, respectively, as the corresponding parameters approach unity if the system is in perfect radial or a linear arrangement. In a confined system like a droplet with planar degenerate surface anchoring, a bipolar orientation is expected. By the nature of these calculations, colour mapping of each LC coarse-grained molecule according to its order parameter is possible for S_R , but not for S_U . For definition of different order parameters refer to Chapter 3.4.

To visualise the latter results, the contribution of each molecule to the linear orientation was plotted in Figure 7.3. The DPD simulations yield for the fully homeotropic shell a global S_U value of 0.09 ± 0.01 and a global S_R value of 0.80 ± 0.003 . These results indicate that the mesogens in the LC droplet conform to a radial distribution, as expected. The colour-coded map of LC molecules for S_R results shows that the only possible defect for this system appears near the core of the droplet. The colour-coded S_U map helps understand why the correspondent order parameter was very low: the LC mesogens oriented horizontally within the droplet antagonize those oriented vertically (in the frame of Figure 7.3), decreasing the cumulative order. The continuum calculations help visualise the shape of the defect structure, a ring defect, expected to emerge clearly as the droplet size increases. This defect structure could be a hedgehog, depending on the molecular features and thermodynamic properties.^{170, 171} Note that the elastic energy and thermotropic energy parameters used in this study for finite-element method were representative of a widely used LC molecule, namely 5CB.¹³⁹ In the DPD simulations a volume based correlation was set in which each rod occupies the space equivalent to two 5CB molecules.

For the LC droplet with fully planar degenerate anchoring, both models show evidence of a bipolar alignment among the LC molecules, as expected. Consistent with expectations, the DPD simulations yield cumulative order parameters $S_U = 1.05 \pm 0.02$ and $S_R = -0.18 \pm 0.01$, while the continuum model provides evidence for two +1 splay-type boojums. By definition, $S_U \leq 1$; the results show a larger value in some cases, which is a numerical error caused by the discrete form of the scalar order parameter described in previous section.

For the LC droplet with half homeotropic and half planar degenerate anchoring, the DPD simulations yield $S_U = 0.31 \pm 0.02$ and $S_R = 0.37 \pm 0.01$. Visualisation of the DPD results in Figure 7.3 reveals that each of the two halves of the droplet possesses an ordered structure of its own, dictated by the surface conditions. The S_R map reveals that, for the conditions of strong anchoring considered in these calculations, the defects accumulate at the interface between the two halves, and that in the middle-bottom region of the droplet a possible boojum appears. The continuum method again reveals a well-defined structure of these defects, which appear in the form of a $+1/2$ ring defect at the interface between the two droplet halves, and a +1 splay-type boojum within the

half of the droplet characterised by planar degenerate anchoring, the latter being consistent with a bipolar director configuration within the droplet.¹⁴³

The analysis of the results shown in Figure 7.3 demonstrates that DPD simulations yield an accurate prediction for the alignment of coarse-grained LC molecules, with the possibility of identifying possible defect regions within the LC droplet. However, the details concerning the defect are not as easily extracted from DPD results as in the continuum model. Mapping the DPD simulation results, obtained for droplets of 30 nm diameters, on Q-tensor calculations conducted for droplets of 0.1 μm diameters is a significant step forward in modelling LC structures, because droplets in the nm scale are difficult to probe experimentally. Because numerous studies have shown that Q-tensor calculations match experimental results,¹⁷²⁻¹⁷⁴ the approach described here suggests that the positive relationship between experiments and finite-element calculations can be transferred to molecular-scale simulations. This multi-scale approach will enable the community to reliably sample LC systems, therefore underpinning future technological applications.

Moving forward from the simulations explained in Figure 7.3, investigation started with Homeotropic Centre (HC) droplets as shown in Figure 7.1.1(a). S_U increases as the portion of the droplet surface on which planar degenerate anchoring is imposed increases; correspondingly, S_R decreases. This was an expected result, as planar degenerate anchoring more strongly promotes uniaxial ordering, by definition, whereas homeotropic anchoring strongly promotes the radial distribution of the mesogens within the droplet. Therefore, HC droplets with 10% planar degenerate anchoring show high S_U and low S_R , while HC droplets with 90% planar degenerate anchoring show low S_U and high S_R . Example snapshots provided in Figure 7.1.1(a) are colour-coded to distinguish the DPD results from the continuum calculations. The examples chosen represent HC droplets whose surface anchoring is 50% planar degenerate and 50% homeotropic. To illustrate S_R order, the tensor of each mesogen within the system was plotted. A contribution factor, which ranges from 0 to 1, is employed to visualise how each individual mesogen increases, or decreases the cumulative S_U order for the droplet. Molecules in Figure 7.1.1(a) were colour-coded accordingly. Additional snapshots to illustrate the LC droplet structures are provided in Appendix C.

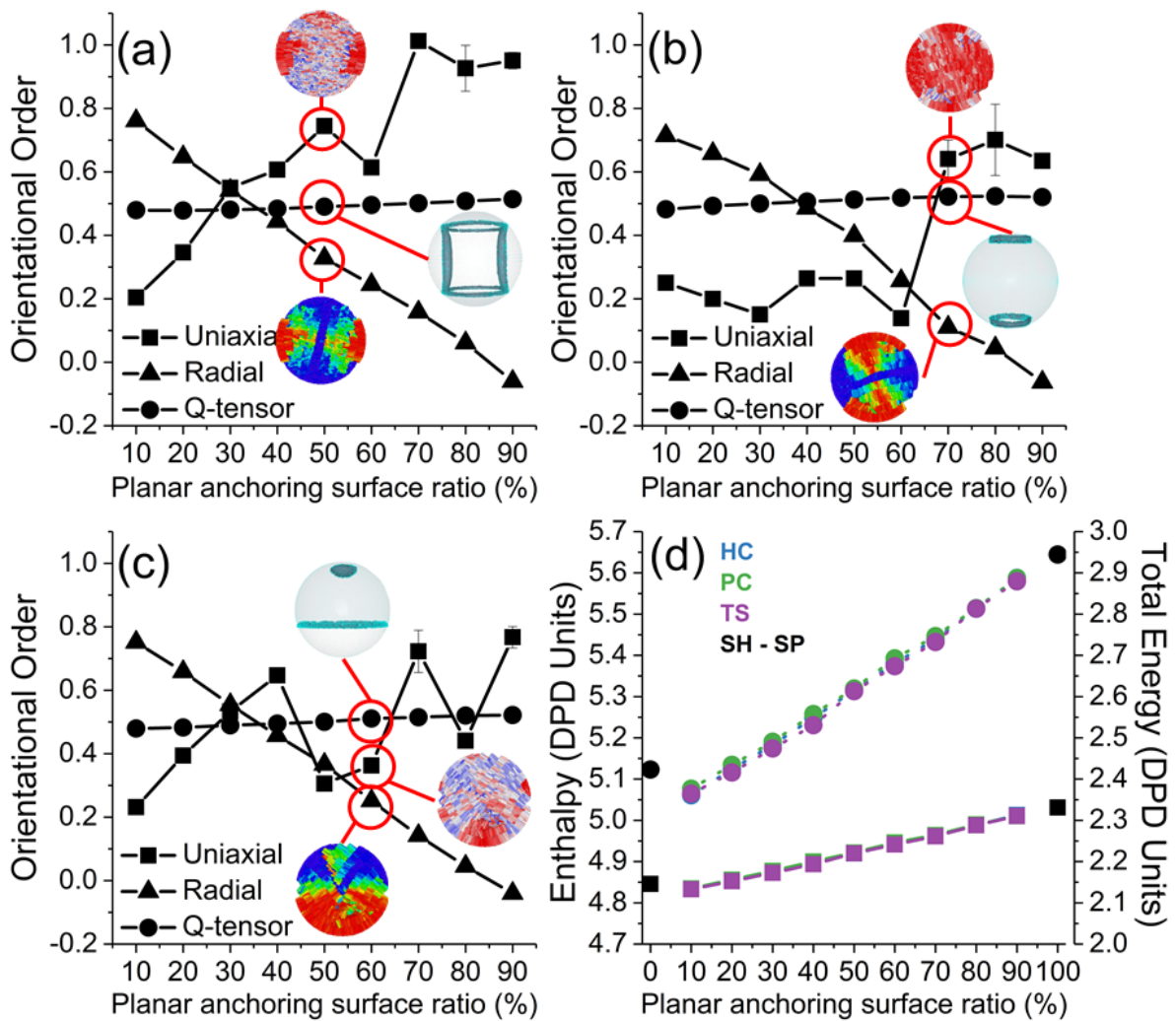


Figure 7.1.1. Orientational order as quantified by DPD simulations (S_U and S_R) and Q-tensor calculations for (a) HC (homeotropic centre), (b) PC (planar centre), and (c) TS (two-sided) type droplets. (d) Comparison of total energy (full line with square) and total enthalpy (dashed line with circle) of all droplets for DPD results; SH and SP represent fully strong homeotropic and fully strong planar degenerate anchoring, respectively.

Refined mesh structures within Q-tensor theory calculations revealed that the global order was always between 0.48 – 0.52, and the type of surface anchoring had a little impact. Presumably because of the volumetric ratio between the defects and the whole droplet, although defect types and locations change with respect to the surface anchoring conditions. While DPD was effective at mapping the defect regions within a droplet, the Q-tensor approach was essential to elucidate the defects themselves.¹⁷⁵ This situation was observed in the quantitative analysis of orientational orders, conducted for both simulation types. Having a relatively larger affected regions in DPD calculations, created a larger volume for defects that differ from the ordered

assembly of LC molecules. Whereas in Q-tensor calculations defects were confined in small volumes and did not affect the cumulative order. This complementarity yields a difference between order parameter calculations conducted via two different computational approaches.

Second set is the droplets that endorse planar degenerate anchoring in the equator and impose homeotropic anchoring towards the tips (therefore it is called Planar Centre, PC), as shown in Figure 7.1.1(b). The ratio for planar degenerate anchoring to the homeotropic anchoring in terms of surface area increases in these PC type droplets, the orientation must be almost perfectly uniaxial due to homeotropic anchoring on the boojums. As can be seen in Figure 7.1.1(b), S_U results are correlated with this estimation. Due to the configuration of PC type droplets S_U parameter has the value of approximately 0.2 for low planar degenerate anchoring ratio, and this value jumps to around 0.6, particularly after 60%. The jump in the parameter is due to the size of the rings getting smaller, enabling more molecules to be ordered towards the direction of the polar axis of the droplet. In addition, decreasing homeotropic anchoring surface area locally affects only the boojums. The example snapshot of 60% planar degenerate anchoring surface revealed that the tips of droplets endorsed uniaxiality and point defects disappeared. Instead, boojums are composed of two $+\frac{1}{2}$ ring defects. The snapshots for all droplets are provided in Appendix C. Profiles in Figure 7.1.1(b), for S_R and the Q-tensor results, are similar to that of Figure 7.1.1(a). As the homeotropic anchoring decreases in terms of surface ratio, S_R decreases due to same reasons explained for Figure 7.1.1(a). For Q-tensor calculations, volumetric ratio of the defects did not significantly affect the nematicity of LC molecules, therefore the orientational order of 0.5 was obtained for all PC type droplets.

Final set for the orientational order investigation is the two-sided (TS) droplets that are shown in Figure 7.1.1(c). S_R parameter decreases as the planar degenerate anchoring increases in surface ratio, and Q-tensor order slightly increases for the same reasons as HC and PC type droplets. S_U results are somewhat unexpected: they increase as the planar degenerate anchoring increases from 10% to 40%, to the value of from 0.23 to 0.65, and then it largely deviates between 0.3 – 0.8. Local ordering of molecules is the reason behind. By fitting the molecules in a confined area with a controlled defect (i.e. homeotropic anchoring) region, locally ordered LC molecules

may or may not be aligned with the global order of the droplet. This will cause the increase or decrease in the orientational order calculated by S_U approach.

Results discussed so far show that DPD simulations propose a similar configuration as Q-tensor calculations do, although they function with different assumptions such as individuality and chemical responses of molecules. However, the quantitative order parameters of the two approaches are not in line. Instead, individual molecules form relatively less ordered structures and as a result, low values of order were observed in DPD simulations. In Q-tensor calculations, the continuation of LC behaviour and the fact that defects occupy much smaller volumes, results with orders that are not so affected by surface conditions. Perhaps the phenomena could be better analysed with the help of experimental observations. The conclusion from these calculations is the fact that orientational order parameters would not necessarily give the same results for molecular simulations and Q-tensor calculations due to different priorities: molecular identity for the former and continuity for the latter although they visually yield similar results in terms of defect regions within the droplets.

Outcome of DPD results also include the total energy and the enthalpy of each droplet. As shown in Figure 7.1.1(d), all droplet types (HC, PC and TS), gave the same result for the same planar degenerate surface anchoring ratio. The energy of the system increased as the planar degenerate anchoring increased, so does the enthalpy. The difference in the slope shows that pressure within the system also increased with respect to planar degenerate anchoring surface. In the next section I will compare these results with the energy results of Q-tensor calculations and analyse elastic energy and thermotropic energy of the droplets in detail.

7.2 TOTAL ENERGY AND ENERGY DENSITY

The Q-tensor analysis allows to extract the various contributions to the total energy system. The results are shown in Figure 7.2.1. Figure 7.2.1(a) shows the elastic energy density of all droplets considered in this chapter. For all cases, the elastic energy increases as the planar degenerate surface anchoring ratio increases, regardless of the LC droplet type. For the PC droplets, the elastic energy increase flattens as fully planar degenerate anchoring on the surface is approached; the opposite holds for HC droplets. For TS droplets, on the other hand, the results show similarity with HC

droplets at one end of the graph, and with PC droplets at the other end, due to the structural similarities of the shells of the three droplet types. In fact, TS droplets have similar morphological properties with the HC droplets when the planar degenerate surface area ratio is low, and similar with the PC droplets when the planar degenerate surface area ratio is high. Similar results were obtained for the thermotropic energy density profiles, as shown in Figure 7.2.1(b).

The energy densities of DPD and Q-tensor calculations were fitted in Figure 7.2.1(c), using the correlation $y = 2.22 \times 10^9 x - 1.11 \times 10^6$, where x represents the energy value in reduced DPD units, obtained by DPD simulations. Comparing the energy densities instead of the total energy is more accurate due to different sizes of the droplets in DPD (30 nm) and Q-tensor (0.1 μm) calculations.

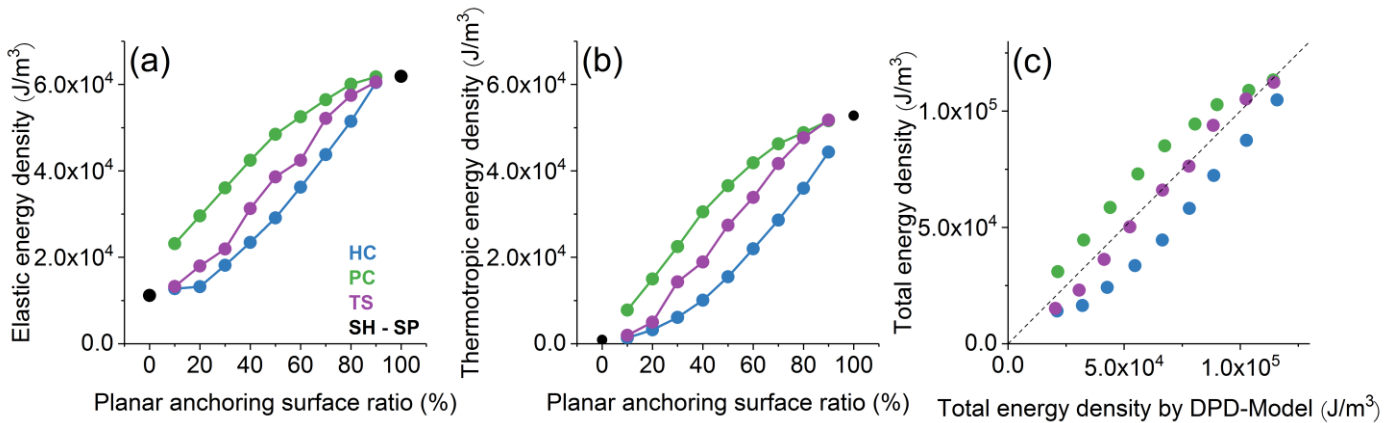


Figure 7.2.1. (a) Elastic and (b) thermotropic energy densities of droplets from Q-tensor calculations for HC (homeotropic centre), PC (planar centre) and TS (two-sided) type droplets. SH and SP represents fully strong homeotropic and fully strong planar degenerate anchoring, respectively. Legend is the same for all graphs. (c) Comparison of energy densities in Q-tensor and DPD calculations. Dashed line is the reference for $y = x$.

DPD simulations yield similar results for all droplet types (HC, PC and TS), whereas in Q-tensor calculations PC type droplets have higher energy and HC type droplets have lower energy for at a given area of planar degenerate surface anchoring. These results suggest that DPD does not reflect the changes in surface morphology on energetics. Therefore, results of PC type droplets were underestimated by DPD simulations, and it was overestimated for HC type droplets. Results for TS type droplets on the other hand, are mostly on the reference line. The numeric results derived from both simulations can be obtained in Appendix C.

7.3 EFFECT OF DROPLET SIZE IN Q-TENSOR CALCULATIONS

While for DPD simulations it would be very computationally demanding to simulate LC droplets of diameter larger than 30 nm, Q-tensor calculations could yield very large errors for droplets smaller than 0.1 μm . Because these size limits do not overlap, a discussion was not made on the effect of droplet size, on the shape of defects and on the droplet energy. However, using the Q-tensor calculations one can quantify droplet size effects for LC droplets larger than 0.1 μm . For three LC droplets (60% HC, 60% PC and 60% TS, respectively), droplet diameter was increased to 1 μm while maintaining similar surface properties.

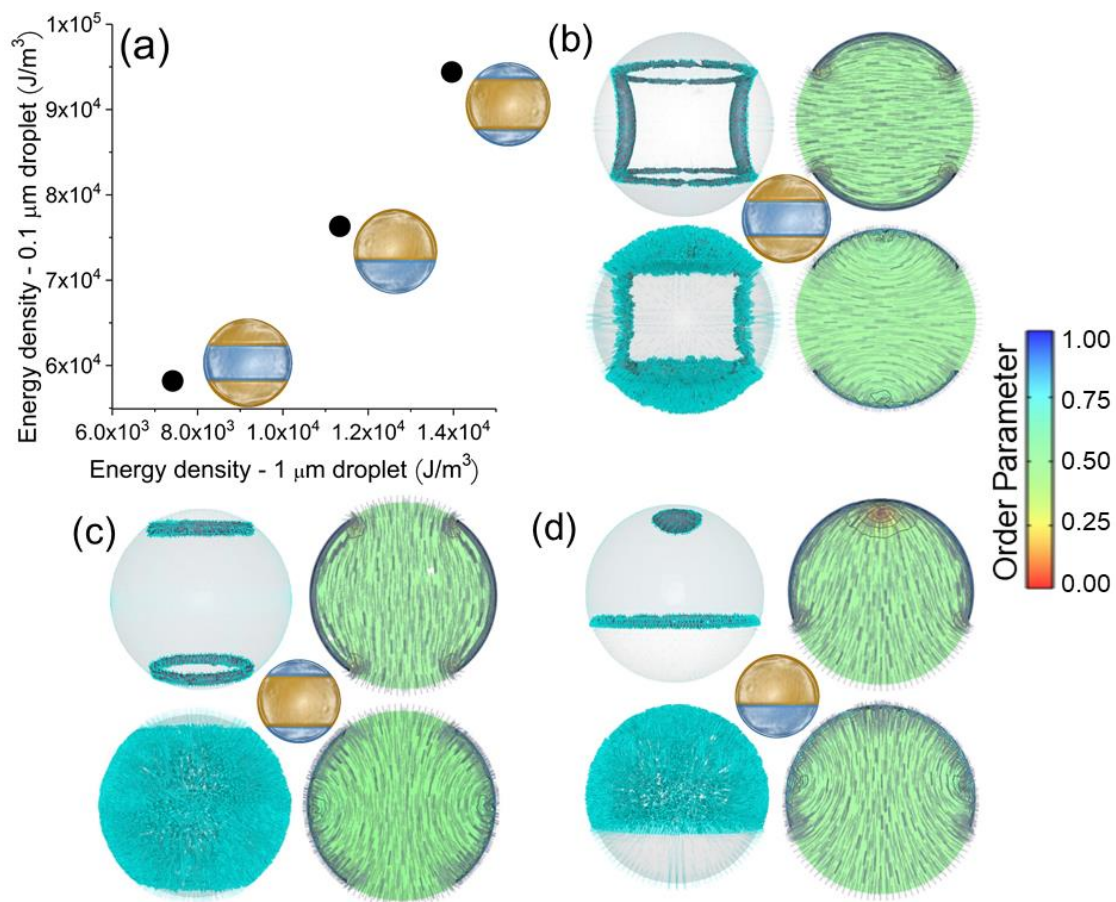


Figure 7.3.1. (a) Total energy densities for 60% HC, PC and TS type droplets with respect to droplet size. (b) 60% HC, (c) 60% PC and (d) 60% TS type droplets with defect regions highlighted (left) and color-coded by order parameter (right). For (b), (c) & (d), top rows represent 0.1 μm droplets and bottom rows represent 1.0 μm droplets. Legend in (b) is the same for (c) and (d).

Figure 7.3.1(a) shows the respective total energy densities of the droplets that are in 0.1 and 1 μm in diameter. The energy density of 0.1 μm droplets is almost one

order of magnitude higher than that for the 1 μm droplets. In both cases PC type droplets have the highest density (1.40×10^4 and $9.44 \times 10^4 \text{ J/m}^3$), followed by TS (1.13×10^4 and $7.63 \times 10^4 \text{ J/m}^3$), and HC droplets (7.42×10^3 and $5.82 \times 10^4 \text{ J/m}^3$). On Figure 7.3.1(b), HC type droplets that are 0.1 μm and 1 μm in size are presented, with 60% planar degenerate anchoring on the surface. The major difference between the two droplets is the alignment on the surface that imposes planar degenerate anchoring. Inside the 0.1 μm droplet, there is a layer of mesogens aligned parallel to the interface of planar degenerate anchoring. For the 1 μm droplet, however, only a thin surface layer of mesogens is aligned parallel to the surface, with the rest of the mesogens perpendicular to the surface; the latter configuration yields a radial alignment at the core of the droplet. Because of the strong surface anchoring, the equilibrium order distribution within droplets of different diameters changes because of different surface-to-volume ratios. For the 0.1 μm droplet, the strong anchoring dominated the alignment within the droplet while for the 1 μm droplet the bulk energy overcame the anchoring conditions and limited their effect to a thin interfacial layer.

The difference caused by surface to volume ratio is visible also in Figure 7.3.1(c) where a PC type droplet with 60% planar degenerate anchoring on the surface is shown. As stated in Figure 7.3.1(b), planar degenerate anchoring became less effective on the global order for the larger droplets, and the LCs formed two $+1/2$ defects at the centre of the planar degenerate anchoring surface, caused by the homeotropic alignment forced by the bulk within the droplet. Similar behaviour is also shown in Figure 7.3.1(d) for the TS type droplet with 60% planar degenerate anchoring. Different from 0.1 μm size droplets, I also visually observed the formation of twisted structures in 1 μm droplets although not quantitatively identified. It is anticipated that because the surface energy is less dominant as the droplet volume increases, the bulk energy dictates the LC mesogens alignment, yielding twisted structures in the LC droplets of diameter 1 μm .

It is reassuring that the change in orientation due to the droplet size has been reported previously.^{25, 77} As increasing the droplet diameter from 0.1 μm to 1 μm yield homeotropic alignment inside the droplet, a change from bipolar to radial configuration was observed as the droplet size increased. What was observed for 1 μm droplets is in line with experimental observations for 6.5 μm droplets.⁷⁷ Because of the different scales being probed, the increase in homeotropic alignment observed in this study

corresponds to the decrease observed experimentally upon an increase in LC droplet size. The overall differences are due to the contribution of the surface energy, which becomes dominant when the droplet size reduces to 0.1 μm and smaller. For droplets in this size range, the surface energy dictates the alignment within the LC droplet, a prediction which should be verified experimentally, once suitable tools are designed to conduct defect analysis within nanoscale droplets.

Overall, this study showed that droplets under extreme confinement give interesting results, but more importantly, nano-sized droplets behave different than their micrometre size counterparts. This is a significant step towards understanding nanodroplets for intensified devices.

CHAPTER 8

SUMMARY AND FUTURE WORK

8.1 SUMMARY OF ACHIEVEMENTS

Control of mesogen orientation is fundamental for further developing optical devices and sensors, among other applications that involve liquid crystals (LCs). Parametric investigations such as those considered here can be conducted to quantify the effect of many parameters on LCs anchoring, including surfactant tail-group branching, nanoparticle interactions, surface conditions, and so forth.

In this thesis, anchoring between LC molecules within a cylindrical bridge was investigated, initially (Chapter 4). It was discussed here how decreasing the soft repulsion between surfactant tail-groups and LCs prevented lateral phase separation from occurring and strongly affected LCs anchoring. LC anchoring could therefore be affected by surfactants adsorption. In particular, the effect of surfactants adsorption on LCs anchoring was quantified, simulating surfactants of three different morphologies. Three rod-coil diblock amphiphiles were modelled, which have short, moderate, and long surfactant tails, respectively.

Systems in which 55% of the surface is covered by surfactants were investigated. It was found that short surfactant tails do not significantly affect anchoring of LC molecules. On the other hand, surfactants with long tails affect LCs orientation, but only at a short range, in agreement with experiments. When the surface coverage was increased from 55% to ~ 80%, surfactants with long tail-groups had a more pronounced effect on the number of LC molecules that changed their anchoring from planar to homeotropic. If the surfactant tail length is short, increasing surfactant density at the LC – water interface did not affect LCs anchoring. For all surfactants at moderate

surface density, a lateral phase separation was observed for the surfactants at the LC – water interface, which causes effects on LCs anchoring to be non-uniform across the interface. It is seen that, within the conditions considered here, regardless of the interaction parameters chosen to describe surfactant tail – LC interactions, surfactants with longer tails were the most effective in promoting homeotropic anchoring at the LC – water interface.

Surfactants' interactions with LC nanodroplets were also investigated (Chapter 5). The results showed both size and temperature dependency on the nematic phase; droplets of similar size yield nematicity at low temperatures. At high temperature all droplets become isotropic. At a given temperature, larger droplets yield more ordered structures. At low concentration, surfactants tend to accumulate at the boojums of the droplets regardless of their tail size. However, the length of the surfactant tail group can affect the droplets asphericity. While surfactants with short or moderate tails decrease asphericity, those with long tails did not change it. As their concentration increases, surfactants distribute on the whole droplets surface. These surfactants can affect LC anchoring, but only at the outer region of the droplets, regardless of the size of droplets and morphology of the surfactants. Then, the effect of surfactants on LC droplets coalescence was observed. While increasing surfactants concentration can decrease the rate of coalescence, the results suggest that, in these systems, coalescence is inevitable. Although as coalescence progresses, the droplets increase in size and the surface density of the surfactants increases, the simulation results suggest that once the droplets become large enough, their shape tend to become spherical.

Adsorption and self-assembly of nanoparticles on liquid crystal droplets were studied using coarse-grained molecular models of NPs (Chapter 6). The results strongly suggest that several factors determine both the existence of preferential adsorption sites on LC droplets and the orientation of the adsorbed NPs. In fact, small particles that were not expected to have a preferred location on the droplet surface showed strong evidence of emergent phenomena. Additionally, the results highlighted marked changes in behaviour for Janus NPs when compared to their homogeneous counterparts. This suggests that the NP – LC molecules' interactions are also important parameters, in addition to the NPs size, in controlling the NPs self-assembly on LC droplets. Overall, for the systems considered here, the simulation results qualitatively

suggest that enthalpic forces predominantly determine the preferential adsorption location for NPs, while entropic forces affect the orientation of the NPs, when possible.

Nanoparticle adsorption on liquid crystal droplets had no significant impact on the overall LC molecules' orientation within the droplet. The reason is that the NPs considered did not penetrate through the droplet surface. Further, in the systems there are no ligands or stabilizing agents, which are often present in experimental studies.^{176, 177} Therefore, there is limited interaction between the particles and the droplet as a whole.

Increasing the nanoparticles size, simulations confirmed that the NPs must be above a certain size threshold to exhibit preferential adsorption location on, e.g., the LC droplets boojums. Results presented here conclusively showed that the NP shape is also an important parameter that can be used to control the preferential adsorption site. For example, two NPs of similar size but different shape can show different preferential adsorption sites. As was the case of small NPs, the NPs surface chemistry is also important, it was quantified by comparing the results obtained for homogeneous vs. Janus particles of the same size and shape.

After the surface anchoring analysis of surfactants and nanoparticles, I modelled 5CB liquid crystal droplets by DPD simulations and continuum approach via Landau – de Gennes theory to compare difference in two different scales (Chapter 7). DPD simulations were used to quantify molecular phenomena for 30 nm droplets, whereas Q-tensor calculations provided insights for droplets of size 0.1 μm , and for some specific cases, 1 μm . The two methodologies are complementary, with DPD providing molecular-level insights and Q-tensor defect formation and morphology. Both quantitative and qualitative agreement were observed.

It was shown that Q-tensor calculations show the same orientational order of nematic droplets (~ 0.5) under all circumstances for all 0.1 μm droplets. In DPD, these results could deviate significantly depending on the type of calculation and surface conditions on the droplets. Defect volume to the droplet volume ratio is high in DPD, and low in Q-tensor calculations. Defects are more confined in Q-tensor simulations, whereas in DPD simulations we see a broad defect area inside the droplet. As a result, these particular defect types and locations have a little effect on global orientational

order of droplets in Q-tensor simulations. Individual molecules reduce the order of droplets for which I used discretised version of tensor order calculations in DPD simulations.

Total energy profiles showed a similar trend between the two methods, in which the energy tends to increase as the area of surface that endorses planar degenerate surface anchoring increases. These energy profiles make the transition possible between the two computational methods and promises comparison in different scales. However, these results revealed that DPD could not differentiate the morphological differences on the shells with same planar degenerate anchoring ratio, for total energy calculations.

The defects and the energies of six droplets that are in three different surface conditions and the size change from 0.1 μm to 1 μm , were compared by using Q-tensor simulations only. The energy density in 0.1 μm droplet was one order of magnitude higher than 1 μm droplets, which shows the dominating effect shifting from surface to the bulk LC. Findings related to 1 μm possess similarity with other works in literature.

Consistent with both expectations from continuum theories and experimental observations, the simulation results presented here quantify the effect of changes in external stimuli on the orientation of LC molecules. The analysis presented here could help interpret experimental results and guide the design of LC-systems for applications: enhancing our quantitative understanding of self-assembly, towards designing protocols to direct the assembly of chosen particles into supra-molecular structures for advanced materials. The results presented in this thesis could guide the selection of promising material models for future computational studies on controlling LC anchoring, to clarify the effect of surface chemistry on preferential adsorption and self-assembly on LC systems.

8.2 FUTURE WORK

It must be noted that in this thesis, LC molecules were assumed to be rigid and rod-like in DPD simulations. LC molecules can vary in size, shape, and flexibility. It is likely that the results could change for different mesogens e.g. partially flexible, or disc like LC molecules. Similar to the approach implemented here, a screening study for different LC molecules could be conducted and LC behaviour dependent on LC

morphology could be analysed. It is anticipated that the response of LC system to the addition of an external chemical such as surfactants, nanoparticles, and other compounds will also depend on the structural properties of LCs. A comprehensive screening could be useful to identify the structural effects on self-assembly prior to any experimental investigation. Perhaps, systems with multiple types of LCs could be investigated since LC mixtures such as E7 is also widely used in research for sensing or display purposes. Methodology and modelling provided in this thesis could set a basis for such mixtures.

Although the focus on this thesis was LC nanodroplets, modelling represented here can guide investigation within bulk LC systems and other types of confinements. In fact, I suggest that an LC mixture in bulk would be easier to analyse than the spherical confinement, as the first step. The orientational and positional preference of different types of LCs will give a clear structure for their utilization as templating agents, which was also covered in this thesis, partially. Once their temperature dependency is set, nanoparticles must be inserted to these systems to check if the LCs guide their movement within the system. Investigation of LC templates would be significant for nanoparticle self-assembly, which is an area of importance not just for optics and sensing, also for catalysis, energy storage, drug delivery and so forth.

Surfactants and nanoparticles with different features must also be studied. Here, I investigated three different surfactants, with similar behaviour, and six different shapes of nanoparticles: particularly for their interactions with rigid LC molecules in spherical confinement. Computational tools provide an efficient way of analysing different material features, and this thesis could be a starting guide for such future work. Moreover, the standard DPD method was implemented in this thesis, because it is one of the most suitable methods for the scale in consideration and the liquid phase systems.¹⁷⁸ Yet, it was seen that other methods could also be utilized for different purposes: many-body DPD simulations¹⁷⁹ for liquid – vapor coexistence, coarse-grained Molecular Dynamics (MD) simulations by utilizing MARTINI force-fields¹⁸⁰ with predefined chemical building blocks, and so forth. Utilizing different computational tools would significantly improve the research of molecular level interactions of LC molecules.

The conditions chosen for DPD simulations in this thesis always propose strong anchoring between LC molecules and surrounding. Either the mutual solubility between LCs and water medium is low so strong planar degenerate anchoring is endorsed, or strong repulsion (attraction) is set within the LC and encapsulating shells for strong planar degenerate (homeotropic) anchoring. For Q-tensor calculations as well, parameters were chosen to be high for strong surface anchoring conditions. The conditions of both strong planar degenerate and strong homeotropic surface anchoring for a small group of droplets were investigated. In addition to strong anchoring calculations, computationally investigating the weak anchoring conditions could guide experimental search on LC-based devices. Because the behaviour under weak anchoring conditions cannot directly be estimated from the results with strong anchoring. Another set of analysis is required. Structures modelled in this thesis can be used for such study, with the change in anchoring strength. Building from those results, other types of confinements can be investigated via continuum calculations, parallel with molecular simulations.

Finally, I believe there is much more to discover: to identify the effect of LC morphology, surfactant and nanoparticle behaviour, anchoring strength, effect of ionic strength, confinement type and conditions, and so forth. If the number of calculations for such correlations were increased, ultimately an empirical equation could be derived that is computationally less demanding, and a road map for experimental studies could be created for LC utilization. LCs are an exciting class of chemicals for what they are proposing with their structural and optical properties. Data provided in this thesis can guide both computational and experimental efforts for the most efficient use of this material in many industrial applications.

APPENDICES

APPENDIX A – SUPPLEMENTARY FOR NANODROPLET SIMULATIONS

In Figure A.1 and A.2, simulations were conducted for 3×10^6 steps and configurations were recorded for last 10^6 steps (last 0.149 μ s). Within these 10^6 steps of simulation production, data are collected in every 10^4 steps and averages of 100 frames are used for quantitative analysis. Last frames of each simulations are used for visuals.

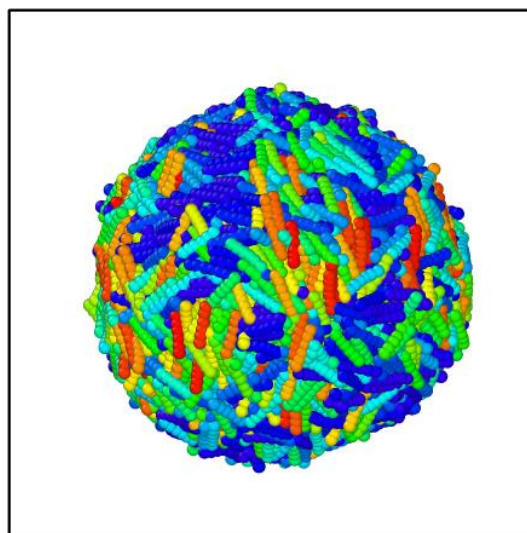


Figure A. 1. Snapshot of the simulation conducted at 1.0 $k_B T$ where repulsion coefficient between water/LC beads was 50 $k_B T/r_c$. Orientational order (S) was calculated as 0.01 ± 0.01 .

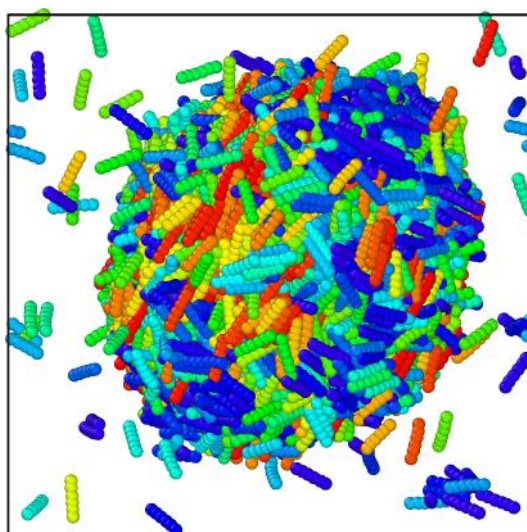


Figure A. 2. Snapshot of the simulation conducted at 0.62 $k_B T$ where repulsion coefficient between water/LC beads was 30 $k_B T/r_c$.

APPENDIX B – SUPPLEMENTARY FOR NANOPARTICLE SIMULATIONS

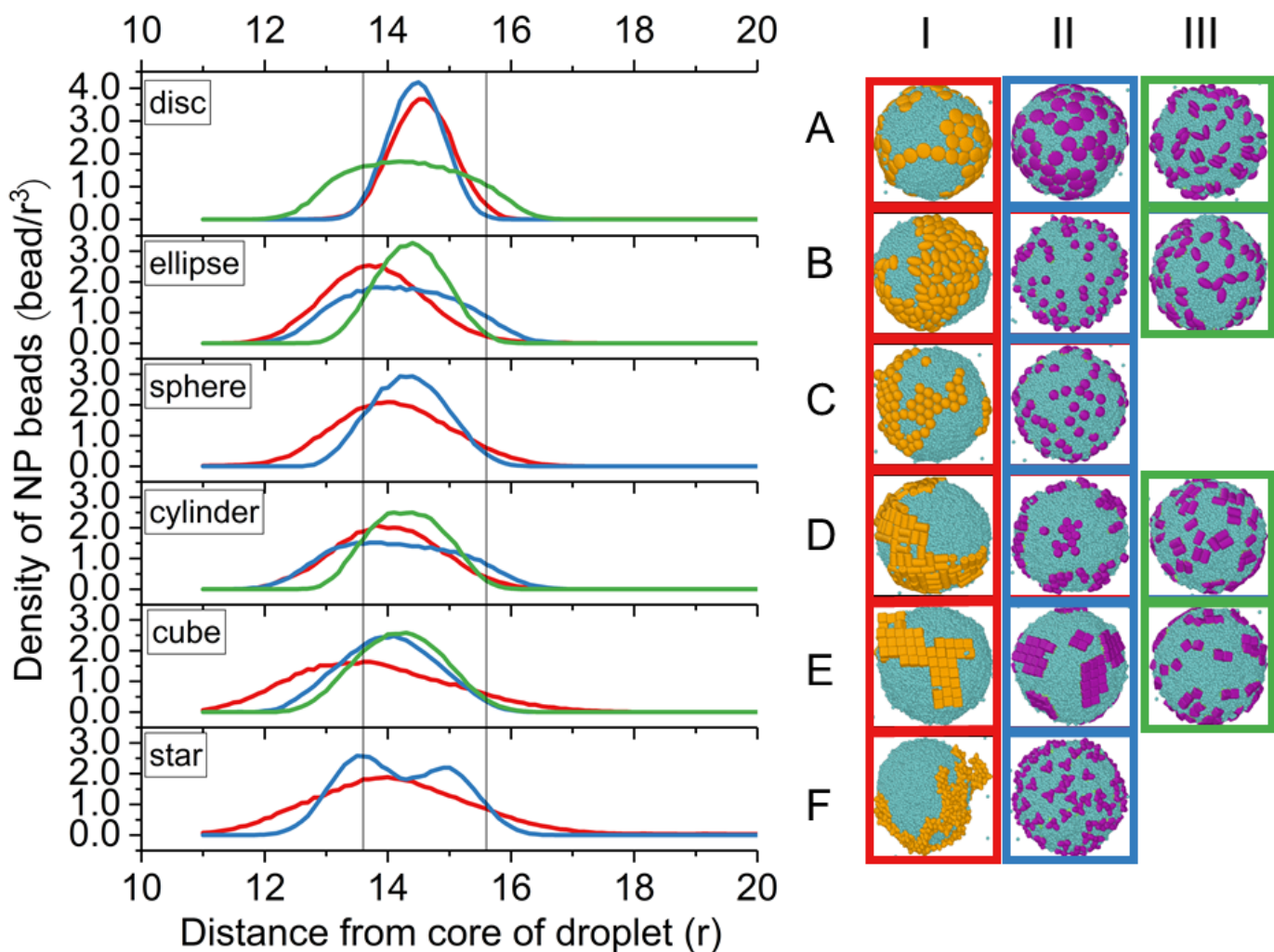


Figure B. 1. Left: Density profiles of NP beads with respect to distance from the oil droplet core. Lines in graph indicate the area between $13.6 - 15.6 r_c$ radii. Right: Corresponding snapshots of oil droplets.

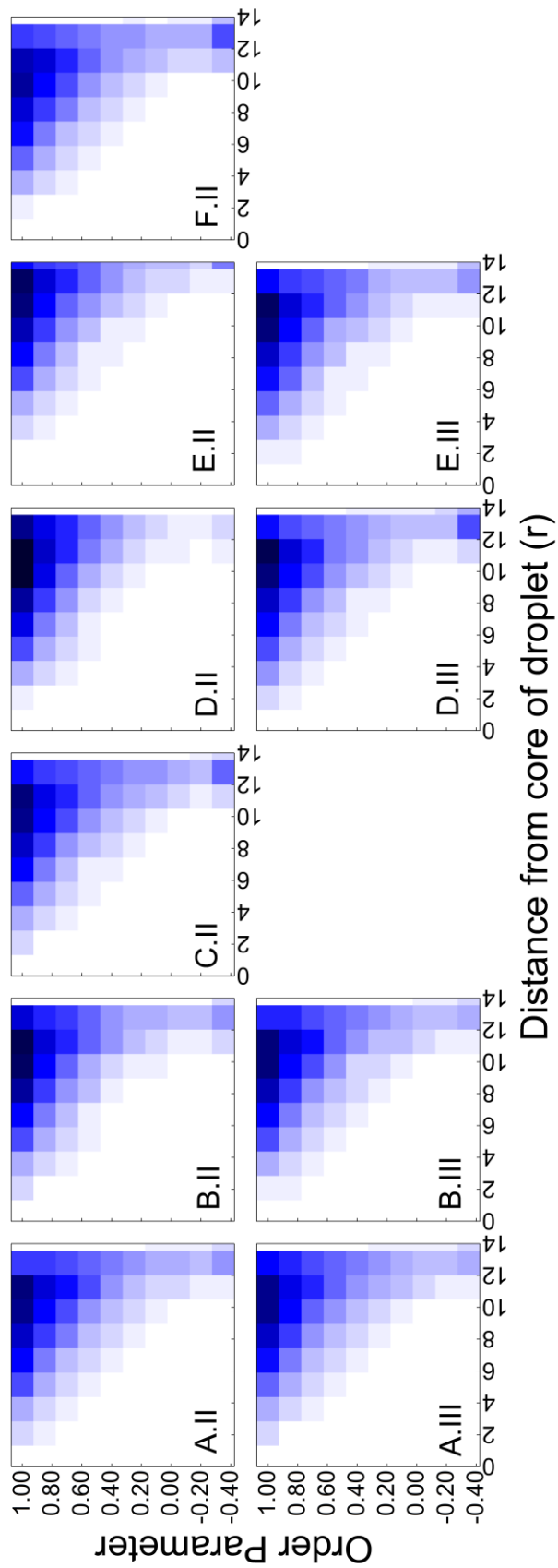


Figure B. 2. Probability distributions of LC mesogens with respect to their locations and second order tensors, for droplets that were exposed to Group II and Group III nanoparticles that were described in Chapter 6.

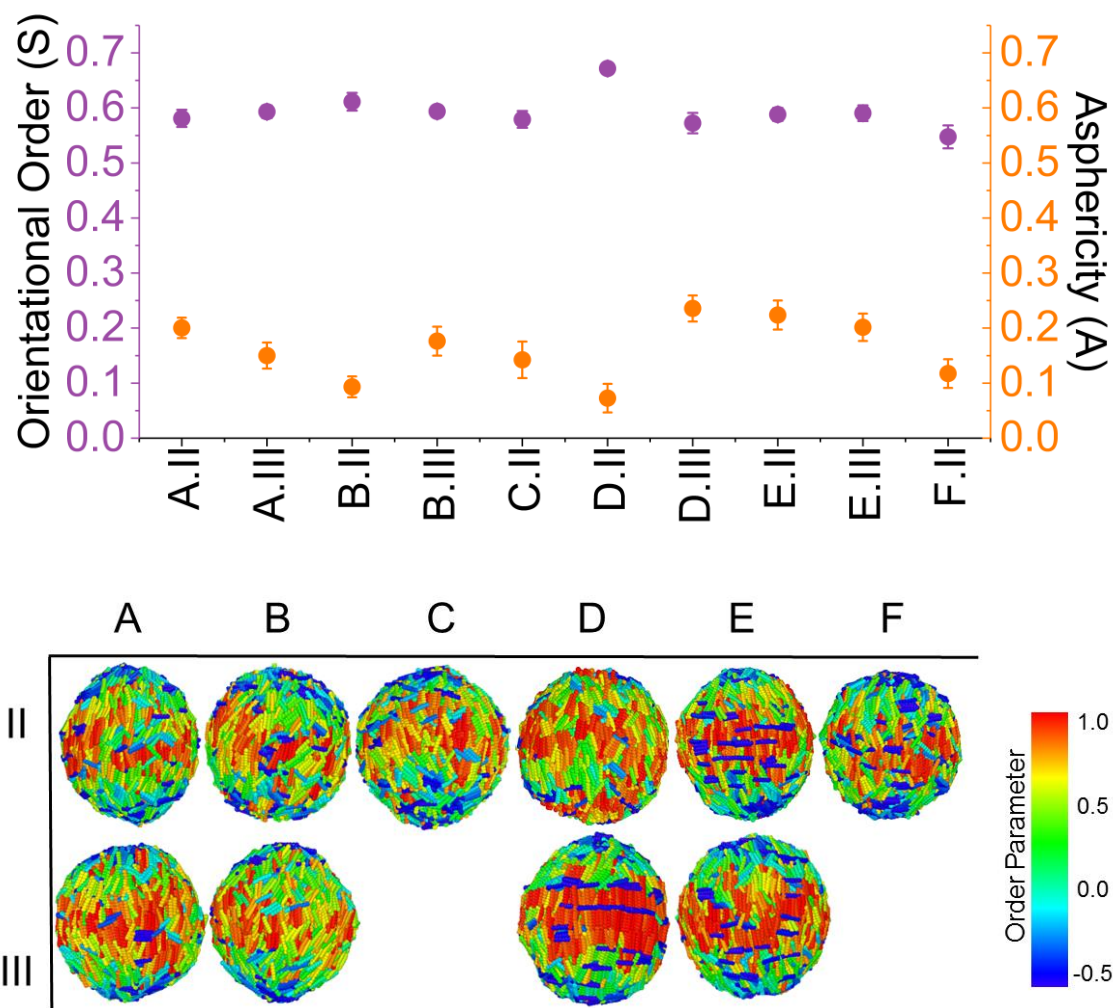


Figure B. 3. (top) Orientational orders (purple) and asphericity (orange) and (bottom) map of LCs on droplets color-coded by their order parameter that were exposed to Group II and Group III nanoparticles.

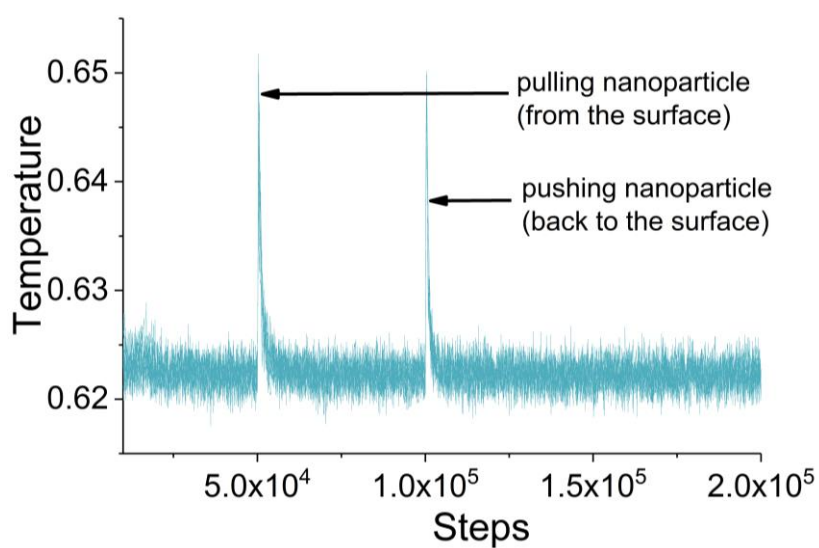


Figure B. 4. Temperature oscillation during the manipulation of the particles. Graph contains all 10 Janus particles.

APPENDIX C – SUPPLEMENTARY FOR Q-TENSOR SIMULATIONS

C.I. THERMOTROPIC PARAMETER CHANGE

Q-tensor simulations, described in Chapter 7, were conducted by using the parameters provided in Table C.1. The temperature dependent parameter, A , was kept as $A = 0$, so that the simulations can be generalized for a wide range of LC molecules.

Table C. 1. Parameters for the Q-tensor calculations implemented in Appendix C.

<i>Calculation</i>	<i>Parameter</i>	<i>Units</i>	<i>Value</i>
F_B	A	N/m ²	0
	B		-2.26×10^6
	C		1.73×10^6
F_D	K ₁₁	pN	6.2
	K ₂₂		3.9
	K ₃₃		8.2
F_s	homeotropic	-	strong
	planar degenerate		strong

In these calculations, the DPD data was taken from Chapter 7, and the energy profile analysis and order parameter calculations were conducted based on the parameters in Table C. 1. For comparison, droplets shown in Figure 7.3, and additional six TS type droplets were chosen. In Figure C.1(a), shells modelled for DPD simulations were shown, alongside the colour-coded representations for S_U and S_R values of each droplet. The quantitative results for DPD simulations are provided in both Figure C.1(b) and (c). Figure C.1(b) shows the results of Q-tensor simulations for which $A = 0$ was implemented. It is revealed that the order parameter estimation in Figure C.1(b) is a better fit than C.1(c), particularly the low values for the droplet that have low to moderate planar degenerate anchoring on the surface. This is caused by larger defects formed, than that of droplets with $A = -1.27 \times 10^6$, as in the main content and Figure C.1(c).

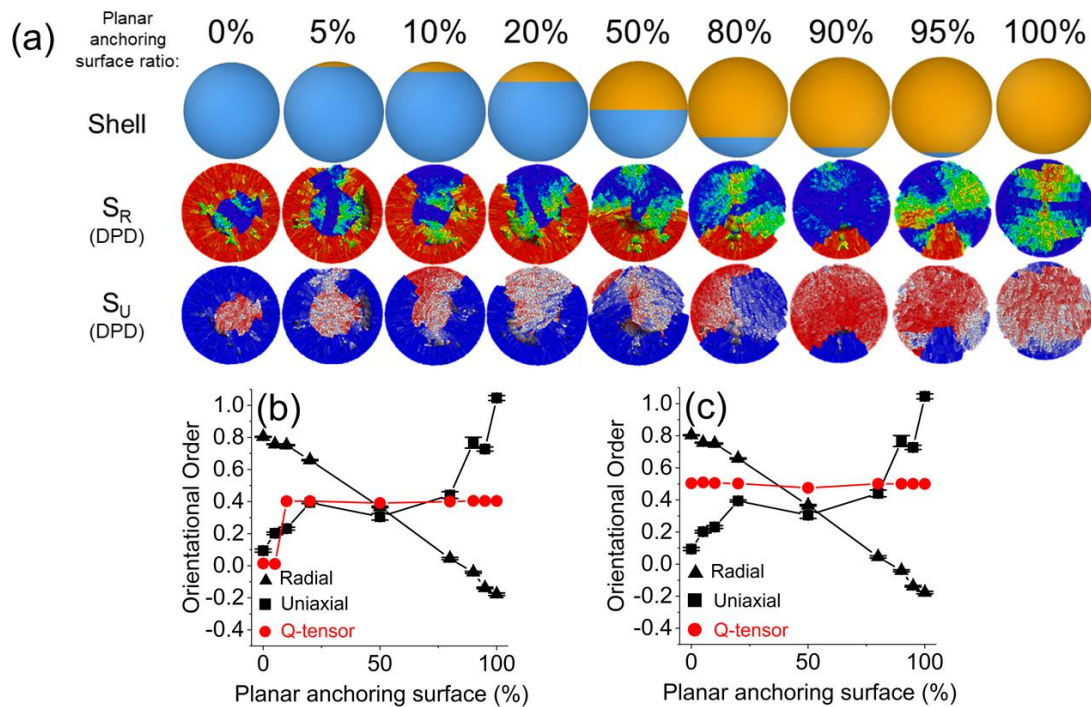


Figure C. 1. (a) Droplets selected for thermotropic coefficient analysis. Orientational order parameters (S) for all droplets simulated based on parameters in (b) Table C.1 and (c) Table 3.4.1. For the colour-coding see main content.

It is estimated that the generalized parameters result in larger defects, which directly affects the order parameter. In Figure C.2, more detailed analysis of Q-tensor simulations was compared, to understand the difference in defect structures.

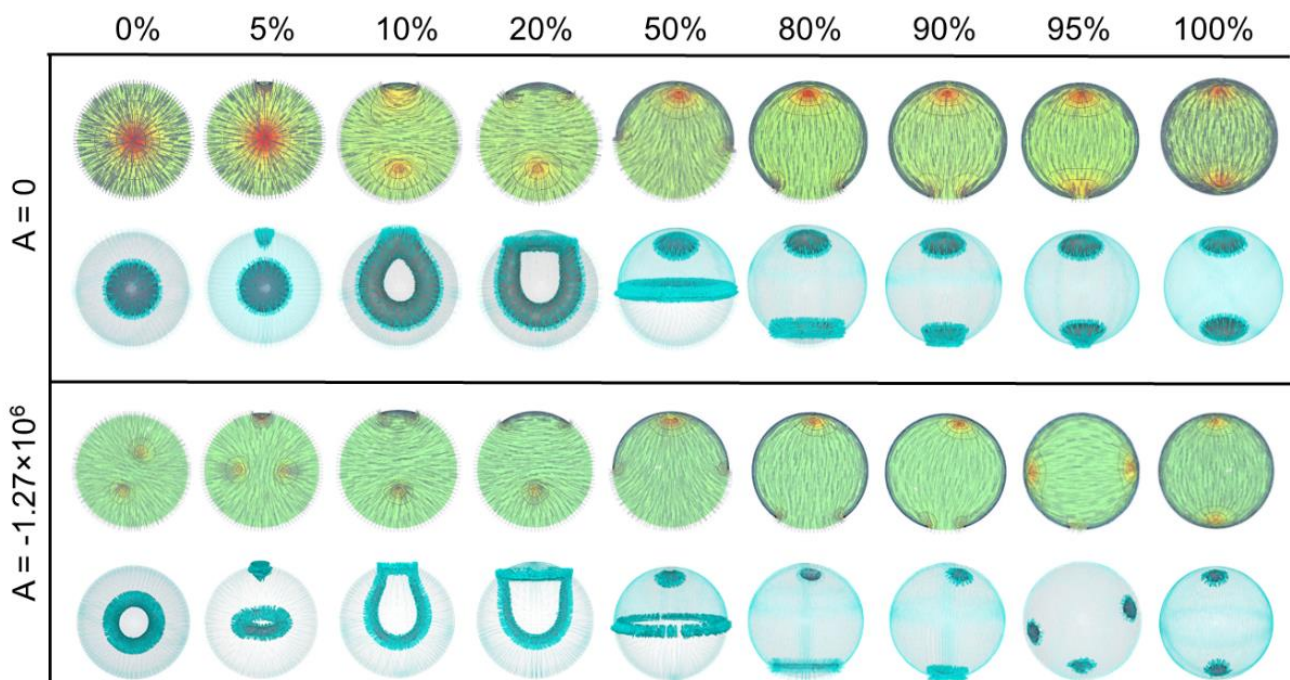


Figure C. 2. Snapshots of simulations by finite-element method with emphasis on defect structures, the images show surfaces of constant order for a low value of S . (top) Calculations with thermotropic parameter $A = 0$, (bottom) $A = -1.27 \times 10^6$.

C.II. SUPPLEMENTARY FOR CHAPTER 7.1

Table C. 2. Simulation results obtained for the total energy densities of the droplets. Results shown here were divided into droplet volume.

	DPD Total Energy Density (DPD Units)	Q-tensor Total Energy Density (J/m³)	DPD Model (J/m³) ($y=2.22 \times 10^9 -$ 1.11×10^6)
HC			
10%	5.10×10^{-4}	1.41×10^4	2.12×10^4
20%	5.14×10^{-4}	1.64×10^4	3.20×10^4
30%	5.19×10^{-4}	2.42×10^4	4.27×10^4
40%	5.25×10^{-4}	3.35×10^4	5.47×10^4
50%	5.30×10^{-4}	4.46×10^4	6.64×10^4
60%	5.35×10^{-4}	5.82×10^4	7.80×10^4
70%	5.40×10^{-4}	7.23×10^4	8.86×10^4
80%	5.46×10^{-4}	8.74×10^4	1.03×10^5
90%	5.52×10^{-4}	1.05×10^5	1.16×10^5
PC			
10%	5.10×10^{-4}	3.09×10^4	2.14×10^4
20%	5.15×10^{-4}	4.45×10^4	3.26×10^4
30%	5.20×10^{-4}	5.86×10^4	4.40×10^4
40%	5.25×10^{-4}	7.30×10^4	5.60×10^4
50%	5.30×10^{-4}	8.50×10^4	6.75×10^4
60%	5.36×10^{-4}	9.44×10^4	8.05×10^4
70%	5.41×10^{-4}	1.03×10^5	9.00×10^4
80%	5.47×10^{-4}	1.09×10^5	1.04×10^5
90%	5.51×10^{-4}	1.13×10^5	1.14×10^5
TS			
10%	5.09×10^{-4}	1.52×10^4	2.04×10^4
20%	5.14×10^{-4}	2.30×10^4	3.07×10^4
30%	5.19×10^{-4}	3.62×10^4	4.14×10^4
40%	5.24×10^{-4}	5.02×10^4	5.25×10^4
50%	5.30×10^{-4}	6.61×10^4	6.65×10^4
60%	5.35×10^{-4}	7.63×10^4	7.79×10^4
70%	5.40×10^{-4}	9.38×10^4	8.83×10^4
80%	5.46×10^{-4}	1.05×10^5	1.02×10^5
90%	5.52×10^{-4}	1.12×10^5	1.14×10^5
0%	5.12×10^{-4}	1.21×10^4	2.73×10^4
100%	5.56×10^{-4}	1.15×10^5	1.25×10^5

Table C. 3. Droplets with homeotropic-centre (HC), with respect to their surface anchoring conditions, defects obtained by Q-tensor calculations (0.1 μm diameter), and colour-coded LC molecules by DPD simulations with respect to S_U and S_R type orientational orders (30 nm diameter). For the colour-coding see main text.


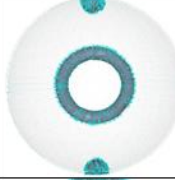
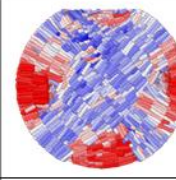
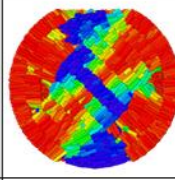
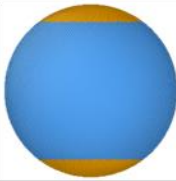

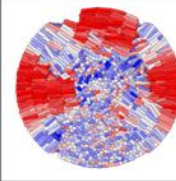
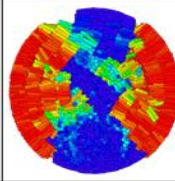
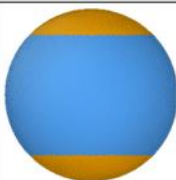

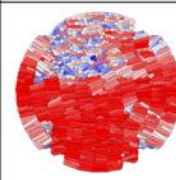
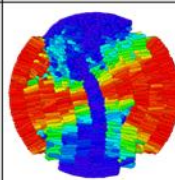
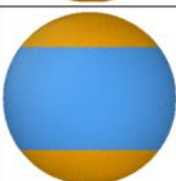

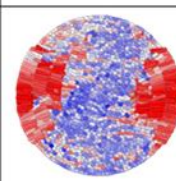
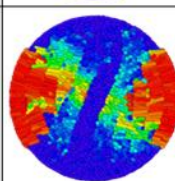
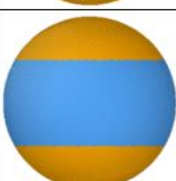
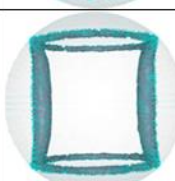
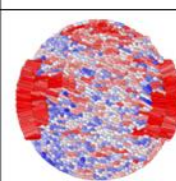
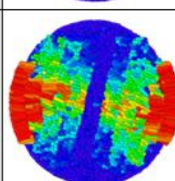
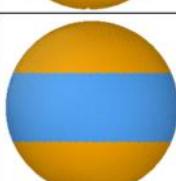

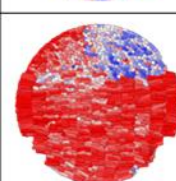
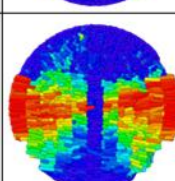
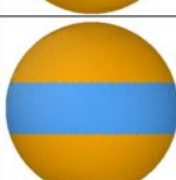

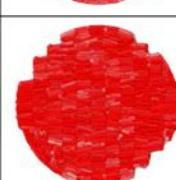
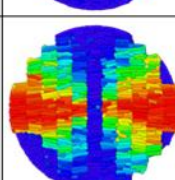
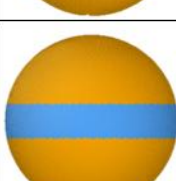

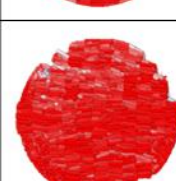
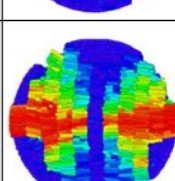
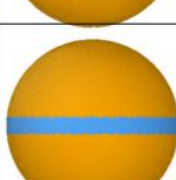
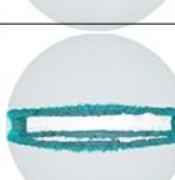
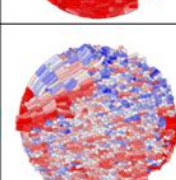
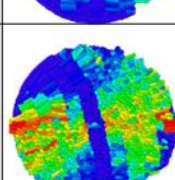
Planar deg. ratio	Shell	Q-Tensor	S_U	S_R
HC 10%				
HC 20%				
HC 30%				
HC 40%				
HC 50%				
HC 60%				
HC 70%				
HC 80%				
HC 90%				

Table C. 4. Droplets with planar-centre (PC), with respect to their surface anchoring conditions, defects obtained by Q-tensor calculations (0.1 μm diameter), and colour-coded LC molecules by DPD simulations with respect to S_U and S_R type orientational orders (30 nm diameter). For the colour-coding see main text.

Planar deg. ratio	Shell	Q-Tensor	S_U	S_R
PC 10%				
PC 20%				
PC 30%				
PC 40%				
PC 50%				
PC 60%				
PC 70%				
PC 80%				
PC 90%				

Table C. 5. Droplets with two-sided surfaces (TS), with respect to their surface anchoring conditions, defects obtained by Q-tensor calculations (0.1 μm diameter), and colour-coded LC molecules by DPD simulations with respect to S_U and S_R type orientational orders (30 nm diameter). For the colour-coding see main text.

Planar deg. ratio	Shell	Q-Tensor	S_U	S_R
TS 10%				
TS 20%				
TS 30%				
TS 40%				
TS 50%				
TS 60%				
TS 70%				
TS 80%				
TS 90%				

BIBLIOGRAPHY

- 1) Dienerowitz, M.; Mazilu, M.; Dholakia, K., Optical manipulation of nanoparticles: a review. *Journal of Nanophotonics* **2008**, 2 (1), 021875.
- 2) Dizaj, S. M.; Lotfipour, F.; Barzegar-Jalali, M.; Zarrintan, M. H.; Adibkia, K., Antimicrobial activity of the metals and metal oxide nanoparticles. *Materials Science and Engineering: C* **2014**, 44, 278-284.
- 3) Glotzer, S. C., Some assembly required. *Science* **2004**, 306 (5695), 419-420.
- 4) Crawford, G.; Zumer, S., Historical perspective of liquid crystals confined to curved geometries. In *Liquid Crystals in Complex Geometries*, Taylor & Francis: 1996; pp 1-19.
- 5) Urbanski, M.; Reyes, C. G.; Noh, J.; Sharma, A.; Geng, Y.; Jampani, V. S. R.; Lagerwall, J. P., Liquid crystals in micron-scale droplets, shells and fibers. *Journal of Physics: Condensed Matter* **2017**, 29 (13), 133003.
- 6) Vertogen, G.; de Jeu, W. H., *Thermotropic Liquid Crystals, Fundamentals*. Springer Science & Business Media: 2012; Vol. 45.
- 7) Sun, S. F., *Physical Chemistry of Macromolecules: Basic Principles and Issues*. John Wiley & Sons: 2004.
- 8) Yang, D.-K.; Wu, S.-T., *Fundamentals of liquid crystal devices*. John Wiley & Sons: 2014.
- 9) Carlton, R. J.; Hunter, J. T.; Miller, D. S.; Abbasi, R.; Mushenheim, P. C.; Tan, L. N.; Abbott, N., Chemical and biological sensing using liquid crystals. *Liquid crystals reviews* **2013**, 1 (1), 29-51.
- 10) Chen, C. P.; Kim, D. S.; Jhun, C. G., Electro-Optical Effects of a Color Polymer-Dispersed Liquid Crystal Device by Micro-Encapsulation with a Pigment-Doped Shell. *Crystals* **2019**, 9 (7), 364.
- 11) Kemiklioglu, E.; Chien, L.-C., Polymer encapsulated and stabilised blue-phase liquid crystal droplets. *Liquid Crystals* **2017**, 44 (4), 722-728.
- 12) Reyes, C. G.; Lagerwall, J. P., Advancing flexible volatile compound sensors using liquid crystals encapsulated in polymer fibers. *Emerging Liquid Crystal Technologies XIII* **2018**, 10555, 1055500.
- 13) Feller, M.; Chen, W.; Shen, Y., Investigation of surface-induced alignment of liquid-crystal molecules by optical second-harmonic generation. *Physical Review A* **1991**, 43 (12), 6778.
- 14) Gibbons, W. M.; Shannon, P. J.; Sun, S.-T.; Swetlin, B. J., Surface-mediated alignment of nematic liquid crystals with polarized laser light. *Nature* **1991**, 351 (6321), 49.
- 15) Vaz, N. A.; Smith, G. W.; Montgomery Jr, G. P., A light control film composed of liquid crystal droplets dispersed in a UV-curable polymer. *Molecular Crystals and Liquid Crystals* **1987**, 146 (1), 1-15.
- 16) Serrano, L. A.; Fornerod, M. J.; Yang, Y.; Gaisford, S.; Stellacci, F.; Guldin, S., Phase behaviour and applications of a binary liquid mixture of methanol and a thermotropic liquid crystal. *Soft Matter* **2018**, 14, 4615-4620.
- 17) Shen, T.-Z.; Hong, S.-H.; Song, J.-K., Electro-optical switching of graphene oxide liquid crystals with an extremely large Kerr coefficient. *Nature materials* **2014**, 13 (4), 394.
- 18) Mertelj, A.; Lisjak, D.; Drofenik, M.; Čopič, M., Ferromagnetism in suspensions of magnetic platelets in liquid crystal. *Nature* **2013**, 504 (7479), 237.
- 19) Brake, J. M.; Mezera, A. D.; Abbott, N. L., Effect of surfactant structure on the orientation of liquid crystals at aqueous- liquid crystal interfaces. *Langmuir* **2003**, 19 (16), 6436-6442.
- 20) Patel, J.; Yokoyama, H., Continuous anchoring transition in liquid crystals. *Nature* **1993**, 362 (6420), 525.
- 21) Lockwood, N. A.; de Pablo, J. J.; Abbott, N. L., Influence of surfactant tail branching and organization on the orientation of liquid crystals at aqueous- liquid crystal interfaces. *Langmuir* **2005**, 21 (15), 6805-6814.
- 22) Feng, P.; Bu, X.; Pine, D. J., Control of pore sizes in mesoporous silica templated by liquid crystals in block copolymer- cosurfactant- water systems. *Langmuir* **2000**, 16 (12), 5304-5310.
- 23) Lopatina, L. M.; Selinger, J. V., Theory of ferroelectric nanoparticles in nematic liquid crystals. *Physical review letters* **2009**, 102 (19), 197802.
- 24) Lavrentovich, O. D.; Pasini, P.; Zannoni, C.; Zumer, S., *Defects in liquid crystals: Computer simulations, theory and experiments*. Springer Science & Business Media: 2012; Vol. 43.
- 25) Gupta, J. K.; Sivakumar, S.; Caruso, F.; Abbott, N. L., Size-Dependent Ordering of Liquid Crystals Observed in Polymeric Capsules with Micrometer and Smaller Diameters. *Angewandte Chemie International Edition* **2009**, 48 (9), 1652-1655.
- 26) Gupta, J. K.; Zimmerman, J. S.; de Pablo, J. J.; Caruso, F.; Abbott, N. L., Characterization of adsorbate-induced ordering transitions of liquid crystals within monodisperse droplets. *Langmuir* **2009**, 25 (16), 9016-9024.
- 27) De Gennes, P.-G.; Prost, J., *The physics of liquid crystals*. Oxford university press: 1993; Vol. 83.
- 28) Virga, E. G., *Variational theories for liquid crystals*. CRC Press: 1995; Vol. 8.

- 29) Mur, U.; Čopar, S.; Ravnik, M.; Čančula, M.; Žumer, S., Unveiling details of defect structures in chiral and achiral nematic droplets by improving simulations of optical images. *Liquid Crystals XX* **2016**, *9940*, 99400V.
- 30) Rey, A. D., Liquid crystal models of biological materials and processes. *Soft Matter* **2010**, *6* (15), 3402-3429.
- 31) Sahu, D. K.; Anjali, T. G.; Basavaraj, M. G.; Aplinc, J.; Čopar, S.; Dhara, S., Orientation, elastic interaction and magnetic response of asymmetric colloids in a nematic liquid crystal. *Scientific Reports* **2019**, *9* (1), 1-10.
- 32) Moreno-Razo, J.; Sambriski, E.; Abbott, N.; Hernández-Ortiz, J.; De Pablo, J., Liquid-crystal-mediated self-assembly at nanodroplet interfaces. *Nature* **2012**, *485* (7396), 86-89.
- 33) Guzmán, O.; Kim, E.; Grollau, S.; Abbott, N.; de Pablo, J., Defect structure around two colloids in a liquid crystal. *Physical Review Letters* **2003**, *91* (23), 235507.
- 34) AlSunaidi, A.; den Otter, W. K.; Clarke, J., Liquid–crystalline ordering in rod–coil diblock copolymers studied by mesoscale simulations. *Philosophical Transactions of the Royal Society of London. Series A: Mathematical, Physical & Engineering Sciences* **2004**, *362* (1821), 1773-1781.
- 35) Levine, Y. K.; Gomes, A. E.; Martins, A. F.; Polimeno, A., A dissipative particle dynamics description of liquid-crystalline phases. I. Methodology and applications. *The Journal of chemical physics* **2005**, *122* (14), 144902.
- 36) AlSunaidi, A.; den Otter, W. K.; Clarke, J., Microphase separation and liquid-crystalline ordering of rod-coil copolymers. *The Journal of chemical physics* **2009**, *130* (12), 124910.
- 37) Inokuchi, T.; Arai, N., Liquid-crystal ordering mediated by self-assembly of surfactant solution confined in nanodroplet: a dissipative particle dynamics study. *Molecular Simulation* **2017**, *43* (13-16), 1218-1226.
- 38) Hernández, S.; Moreno-Razo, J.; Ramírez-Hernández, A.; Díaz-Herrera, E.; Hernández-Ortiz, J.; de Pablo, J. J., Liquid crystal nanodroplets, and the balance between bulk and interfacial interactions. *Soft Matter* **2012**, *8* (5), 1443-1450.
- 39) Tomar, V.; Hernandez, S.; Abbott, N. L.; Hernández-Ortiz, J. P.; De Pablo, J., Morphological transitions in liquid crystal nanodroplets. *Soft Matter* **2012**, *8* (33), 8679-8689.
- 40) Liu, Q.; Senyuk, B.; Tasinkevych, M.; Smalyukh, I. I., Nematic liquid crystal boojums with handles on colloidal handlebodies. *Proceedings of the National Academy of Sciences* **2013**, *110* (23), 9231-9236.
- 41) Rahimi, M.; Roberts, T. F.; Armas-Pérez, J. C.; Wang, X.; Bukusoglu, E.; Abbott, N. L.; de Pablo, J. J., Nanoparticle self-assembly at the interface of liquid crystal droplets. *Proceedings of the National Academy of Sciences* **2015**, *112* (17), 5297-5302.
- 42) Glotzer, S. C.; Solomon, M. J., Anisotropy of building blocks and their assembly into complex structures. *Nature materials* **2007**, *6* (8), 557.
- 43) van Anders, G.; Ahmed, N. K.; Smith, R.; Engel, M.; Glotzer, S. C., Entropically patchy particles: engineering valence through shape entropy. *Acs Nano* **2013**, *8* (1), 931-940.
- 44) Walther, A.; Müller, A. H., Janus particles. *Soft Matter* **2008**, *4* (4), 663-668.
- 45) Demus, D.; Goodby, J. W.; Gray, G. W.; Spiess, H. W.; Vill, V., *Handbook of Liquid Crystals, Volume 2A: Low Molecular Weight Liquid Crystals I: Calamitic Liquid Crystals*. John Wiley & Sons: 2011.
- 46) Lai, Y.-T.; Kuo, J.-C.; Yang, Y.-J., A novel gas sensor using polymer-dispersed liquid crystal doped with carbon nanotubes. *Sensors and Actuators A: Physical* **2014**, *215*, 83-88.
- 47) Sen, A.; Kupcho, K. A.; Grinwald, B. A.; VanTreeck, H. J.; Acharya, B. R., Liquid crystal-based sensors for selective and quantitative detection of nitrogen dioxide. *Sensors and Actuators B: Chemical* **2013**, *178*, 222-227.
- 48) Hartono, D.; Xue, C. Y.; Yang, K. L.; Yung, L. Y. L., Decorating Liquid Crystal Surfaces with Proteins for Real-Time Detection of Specific Protein–Protein Binding. *Advanced Functional Materials* **2009**, *19* (22), 3574-3579.
- 49) Sivakumar, S.; Wark, K. L.; Gupta, J. K.; Abbott, N. L.; Caruso, F., Liquid crystal emulsions as the basis of biological sensors for the optical detection of bacteria and viruses. *Advanced Functional Materials* **2009**, *19* (14), 2260-2265.
- 50) Bao, P.; Paterson, D. A.; Harrison, P. L.; Miller, K.; Peyman, S.; Jones, J. C.; Sandoe, J.; Evans, S. D.; Bushby, R. J.; Gleeson, H. F., Lipid coated liquid crystal droplets for the on-chip detection of antimicrobial peptides. *Lab on a Chip* **2019**, *19* (6), 1082-1089.
- 51) Khan, M.; Khan, A. R.; Shin, J.-H.; Park, S.-Y., A liquid-crystal-based DNA biosensor for pathogen detection. *Scientific reports* **2016**, *6*, 22676.
- 52) Haseloh, S.; van der Schoot, P.; Zentel, R., Control of mesogen configuration in colloids of liquid crystalline polymers. *Soft Matter* **2010**, *6* (17), 4112-4119.

- 53) Amundson, K. R.; Srinivasarao, M., Liquid-crystal-anchoring transitions at surfaces created by polymerization-induced phase separation. *Physical Review E* **1998**, *58* (2), R1211.
- 54) Alino, V. J.; Pang, J.; Yang, K.-L., Liquid crystal droplets as a hosting and sensing platform for developing immunoassays. *Langmuir* **2011**, *27* (19), 11784-11789.
- 55) Erdmann, J. H.; Žumer, S.; Doane, J. W., Configuration transition in a nematic liquid crystal confined to a small spherical cavity. *Physical review letters* **1990**, *64* (16), 1907.
- 56) Lin, I.-H.; Miller, D. S.; Bertics, P. J.; Murphy, C. J.; De Pablo, J. J.; Abbott, N. L., Endotoxin-induced structural transformations in liquid crystalline droplets. *Science* **2011**, *332* (6035), 1297-1300.
- 57) Manna, U.; Zayas-Gonzalez, Y. M.; Carlton, R. J.; Caruso, F.; Abbott, N. L.; Lynn, D. M., Liquid crystal chemical sensors that cells can wear. *Angewandte Chemie International Edition* **2013**, *52* (52), 14011-14015.
- 58) Peddireddy, K.; Kumar, P.; Thutupalli, S.; Herminghaus, S.; Bahr, C., Solubilization of thermotropic liquid crystal compounds in aqueous surfactant solutions. *Langmuir* **2012**, *28* (34), 12426-12431.
- 59) Wang, X.; Zhou, Y.; Kim, Y.-K.; Miller, D. S.; Zhang, R.; Martinez-Gonzalez, J. A.; Bukusoglu, E.; Zhang, B.; Brown, T. M.; de Pablo, J. J., Patterned surface anchoring of nematic droplets at miscible liquid-liquid interfaces. *Soft Matter* **2017**, *13* (34), 5714-5723.
- 60) Feng, X.; Mourran, A.; Möller, M.; Bahr, C., Surface ordering and anchoring behaviour at liquid crystal surfaces laden with semifluorinated alkane molecules. *Soft Matter* **2012**, *8* (37), 9661-9668.
- 61) Gupta, J. K.; Meli, M.-V.; Teren, S.; Abbott, N. L., Elastic energy-driven phase separation of phospholipid monolayers at the nematic liquid-crystal-aqueous interface. *Physical Review Letters* **2008**, *100* (4), 048301.
- 62) Ouyang, Y.-t.; Guo, H.-x., Phase behavior of amphiphiles at liquid crystals/water interface: A coarse-grained molecular dynamics study. *Chinese Journal of Polymer Science* **2014**, *32* (10), 1298-1310.
- 63) Zhang, Z.; Guo, H., A computer simulation study of the anchoring transitions driven by rod-coil amphiphiles at aqueous-liquid crystal interfaces. *Soft Matter* **2012**, *8* (19), 5168-5174.
- 64) Crawford, G. P.; Doane, W.; Zumer, S., Captured orientational order in polymer network assemblies. *Liquid Crystals Today* **1995**, *5* (1), 8-11.
- 65) Ellis, P. W.; Huang, S.; Klaneček, S.; Vallamkondu, J.; Dannemiller, E.; Vernon, M.; Chang, Y.-w.; Goldbart, P. M.; Fernandez-Nieves, A., Defect transitions in nematic liquid-crystal capillary bridges. *Physical Review E* **2018**, *97* (4), 040701.
- 66) Kim, Y.-K.; Senyuk, B.; Shin, S.-T.; Kohlmeier, A.; Mehl, G. H.; Lavrentovich, O. D., Surface alignment, anchoring transitions, optical properties, and topological defects in the thermotropic nematic phase of organo-siloxane tetrapodes. *Soft Matter* **2014**, *10* (3), 500-509.
- 67) Wang, X.; Kim, Y.-K.; Bukusoglu, E.; Zhang, B.; Miller, D. S.; Abbott, N. L., Experimental insights into the nanostructure of the cores of topological defects in liquid crystals. *Physical review letters* **2016**, *116* (14), 147801.
- 68) Wang, X.; Miller, D. S.; Bukusoglu, E.; De Pablo, J. J.; Abbott, N. L., Topological defects in liquid crystals as templates for molecular self-assembly. *Nature materials* **2016**, *15* (1), 106-112.
- 69) Williams, C.; Cladis, P.; Kleman, M., Screw disclinations in nematic samples with cylindrical symmetry. *Molecular Crystals and Liquid Crystals* **1973**, *21* (3-4), 355-373.
- 70) Williams, C.; Pierański, P.; Cladis, P., Nonsingular $S=+1$ screw disclination lines in nematics. *Physical Review Letters* **1972**, *29* (2), 90.
- 71) Crawford, G. P.; Zumer, S., *Liquid Crystals in Complex Geometries Formed by Polymer and Porous Networks*. Taylor and Francis: New York, 1996.
- 72) Meyer, R. B., Point disclinations at a nematic-Isotropic liquid interface. *Molecular Crystals and Liquid Crystals* **1972**, *16* (4), 355-369.
- 73) Meyer, R. B., On the existence of even indexed disclinations in nematic liquid crystals. *Philosophical Magazine* **1973**, *27* (2), 405-424.
- 74) Busch, M.; Kityk, A. V.; Piecek, W.; Hofmann, T.; Wallacher, D.; Całus, S.; Kula, P.; Steinhart, M.; Eich, M.; Huber, P., A ferroelectric liquid crystal confined in cylindrical nanopores: reversible smectic layer buckling, enhanced light rotation and extremely fast electro-optically active Goldstone excitations. *Nanoscale* **2017**, *9* (48), 19086-19099.
- 75) Ondris-Crawford, R.; Crawford, G.; Doane, J.; Žumer, S.; Vilfan, M.; Vilfan, I., Surface molecular anchoring in microconfined liquid crystals near the nematic-smectic-A transition. *Physical Review E* **1993**, *48* (3), 1998.
- 76) Bera, T.; Fang, J., Polyelectrolyte-coated liquid crystal droplets for detecting charged macromolecules. *Journal of Materials Chemistry* **2012**, *22* (14), 6807-6812.
- 77) Miller, D. S.; Abbott, N., Influence of droplet size, pH and ionic strength on endotoxin-triggered ordering transitions in liquid crystalline droplets. *Soft Matter* **2013**, *9* (2), 374-382.

- 78) Tongcher, O.; Sigel, R.; Landfester, K., Liquid crystal nanoparticles prepared as miniemulsions. *Langmuir* **2006**, *22* (10), 4504-4511.
- 79) Bačová, P.; Glynos, E.; Anastasiadis, S. H.; Harmandaris, V., Nanostructuring Single-Molecule Polymeric Nanoparticles via Macromolecular Architecture. *ACS Nano* **2019**, *13* (2), 2439-2449.
- 80) Borówko, M.; Rżysko, W.; Sokołowski, S.; Staszewski, T., Self-assembly of hairy disks in two dimensions—insights from molecular simulations. *Soft matter* **2018**, *14* (16), 3115-3126.
- 81) Hansoge, N. K.; Huang, T.; Sinko, R.; Xia, W.; Chen, W.; Keten, S., Materials by design for stiff and tough hairy nanoparticle assemblies. *ACS Nano* **2018**, *12* (8), 7946-7958.
- 82) Harper, E. S.; Waters, B.; Glotzer, S. C., Hierarchical self-assembly of hard cube derivatives. *Soft matter* **2019**, *15* (18), 3733-3739.
- 83) Pawar, A. B.; Kretschmar, I., Fabrication, assembly, and application of patchy particles. *Macromolecular rapid communications* **2010**, *31* (2), 150-168.
- 84) Zhang, Z.; Horsch, M. A.; Lamm, M. H.; Glotzer, S. C., Tethered nano building blocks: Toward a conceptual framework for nanoparticle self-assembly. *Nano Letters* **2003**, *3* (10), 1341-1346.
- 85) Zhang, Y.; Cao, M.; Han, G.; Guo, T.; Ying, T.; Zhang, W., Topology affecting block copolymer nanoassemblies: linear block copolymers versus star block copolymers under PISA conditions. *Macromolecules* **2018**, *51* (14), 5440-5449.
- 86) Huang, F.; Lv, Y.; Wang, L.; Xu, P.; Lin, J.; Lin, S., An insight into polymerization-induced self-assembly by dissipative particle dynamics simulation. *Soft matter* **2016**, *12* (30), 6422-6429.
- 87) Li, Q.; Wang, Z.; Yin, Y.; Jiang, R.; Li, B., Self-assembly of giant amphiphiles based on polymer-tethered nanoparticle in selective solvents. *Macromolecules* **2018**, *51* (8), 3050-3058.
- 88) Yan, Y.-D.; Xue, Y.-H.; Zhao, H.-Y.; Liu, H.; Lu, Z.-Y.; Gu, F.-L., Insight into the Polymerization-Induced Self-Assembly via a Realistic Computer Simulation Strategy. *Macromolecules* **2019**, *52* (16), 6169-6180.
- 89) Pickering, S. U., Emulsions. *Journal of the Chemical Society, Transactions* **1907**, *91*, 2001-2021.
- 90) Ning, Y.; Meldrum, F. C.; Armes, S. P., Efficient occlusion of oil droplets within calcite crystals. *Chemical Science* **2019**, *10*, 8964-8972.
- 91) Sicard, F.; Striolo, A., Computational simulations for particles at interfaces. In *Anisotropic Particle Assemblies*, Elsevier: 2018; pp 167-200.
- 92) Zhao, X.; Yu, G.; Li, J.; Feng, Y.; Zhang, L.; Peng, Y.; Tang, Y.; Wang, L., Eco-friendly Pickering emulsion stabilized by silica nanoparticles dispersed with high-molecular-weight amphiphilic alginate derivatives. *ACS Sustainable Chemistry & Engineering* **2018**, *6* (3), 4105-4114.
- 93) Ruhland, T. M.; Gröschel, A. H.; Ballard, N.; Skelton, T. S.; Walther, A.; Müller, A. H.; Bon, S. A., Influence of Janus particle shape on their interfacial behavior at liquid-liquid interfaces. *Langmuir* **2013**, *29* (5), 1388-1394.
- 94) Li, Y.; Khoo, N.; Prince, E.; Alizadehgiashi, M.; Galati, E.; Lavrentovich, O. D.; Kumacheva, E., Nanoparticle-laden droplets of liquid crystals: Interactive morphogenesis and dynamic assembly. *Science advances* **2019**, *5* (7), eaav1035.
- 95) Li, Y.; Suen, J. J.-Y.; Prince, E.; Larin, E. M.; Klinkova, A.; Thérien-Aubin, H.; Zhu, S.; Yang, B.; Helmy, A. S.; Lavrentovich, O. D., Colloidal cholesteric liquid crystal in spherical confinement. *Nature communications* **2016**, *7*, 12520.
- 96) Whitmer, J. K.; Wang, X.; Mondiot, F.; Miller, D. S.; Abbott, N. L.; de Pablo, J. J., Nematic-field-driven positioning of particles in liquid crystal droplets. *Physical review letters* **2013**, *111* (22), 227801.
- 97) Chu, G.; Vasilyev, G.; Vilensky, R.; Boaz, M.; Zhang, R.; Martin, P.; Dahan, N.; Deng, S.; Zussman, E., Controlled Assembly of Nanocellulose-Stabilized Emulsions with Periodic Liquid Crystal-in-Liquid Crystal Organization. *Langmuir* **2018**, *34* (44), 13263-13273.
- 98) Mundoor, H.; Park, S.; Senyuk, B.; Wensink, H. H.; Smalyukh, I. I., Hybrid molecular-colloidal liquid crystals. *Science* **2018**, *360* (6390), 768-771.
- 99) Munir, S.; Park, S.-Y., Liquid-crystal droplets functionalized with a non-enzymatic moiety for glucose sensing. *Sensors and Actuators B: Chemical* **2018**, *257*, 579-585.
- 100) Perju, E.; Paslaru, E.; Marin, L., Polymer-dispersed liquid crystal composites for bio-applications: thermotropic, surface and optical properties. *Liquid Crystals* **2015**, *42* (3), 370-382.
- 101) Liu, Y.; Sun, X.; Elim, H.; Ji, W., Gain narrowing and random lasing from dye-doped polymer-dispersed liquid crystals with nanoscale liquid crystal droplets. *Applied physics letters* **2006**, *89* (1), 011111.
- 102) Gupta, J. K.; Sivakumar, S.; Caruso, F.; Abbott, N. L., Size-Dependent Ordering of Liquid Crystals Observed in Polymeric Capsules with Micrometer and Smaller Diameters. *Angewandte Chemie* **2009**, *121* (9), 1680-1683.
- 103) Cladis, P.; Kleman, M., Non-singular disclinations of strength $S=+1$ in nematics. *Journal de Physique* **1972**, *33* (5-6), 591-598.

- 104) Wei, X.; Hooper, J. B.; Bedrov, D., Influence of electrostatic interactions on the properties of cyanobiphenyl liquid crystals predicted from atomistic molecular dynamics simulations. *Liquid Crystals* **2017**, *44* (2), 332-347.
- 105) Peroukidis, S. D.; Vanakaras, A. G.; Photinos, D. J., Molecular simulation study of polar order in orthogonal bent-core smectic liquid crystals. *Physical Review E* **2015**, *91* (6), 062501.
- 106) Gürbulak, O.; Cebe, E., Molecular dynamics study of 5CB at the air-water interface: From gas to beyond the monolayer collapse. *Journal of Molecular Liquids* **2018**, *256*, 611-619.
- 107) Brown, W. M.; Petersen, M. K.; Plimpton, S. J.; Grest, G. S., Liquid crystal nanodroplets in solution. *The Journal of chemical physics* **2009**, *130* (4), 044901.
- 108) Tsujinoue, H.; Inokuchi, T.; Arai, N., Polymorphic transitions mediated by surfactants in liquid crystal nanodroplet. *Liquid Crystals* **2019**, *46* (9), 1428-1439.
- 109) Zhang, J.; Su, J.; Ma, Y.; Guo, H., Coarse-grained molecular dynamics simulations of the phase behavior of the 4-cyano-4'-pentylbiphenyl liquid crystal system. *The Journal of Physical Chemistry B* **2012**, *116* (7), 2075-2089.
- 110) Hoogerbrugge, P.; Koelman, J., Simulating microscopic hydrodynamic phenomena with dissipative particle dynamics. *EPL (Europhysics Letters)* **1992**, *19* (3), 155.
- 111) Koelman, J.; Hoogerbrugge, P., Dynamic simulations of hard-sphere suspensions under steady shear. *EPL (Europhysics Letters)* **1993**, *21* (3), 363.
- 112) Lin, Y.-L.; Chang, H.-Y.; Sheng, Y.-J.; Tsao, H.-K., Photoresponsive polymersomes formed by amphiphilic linear-dendritic block copolymers: generation-dependent aggregation behavior. *Macromolecules* **2012**, *45* (17), 7143-7156.
- 113) Wang, Z.; Wang, H.; Cheng, M.; Li, C.; Faller, R.; Sun, S.; Hu, S., Controllable Multi-Geometry Nanoparticles via Cooperative Assembly of Amphiphilic Diblock Copolymer Blends with Asymmetric Architectures. *ACS Nano* **2018**.
- 114) Yamamoto, S.; Maruyama, Y.; Hyodo, S.-a., Dissipative particle dynamics study of spontaneous vesicle formation of amphiphilic molecules. *The Journal of Chemical Physics* **2002**, *116* (13), 5842-5849.
- 115) Fan, H.; Striolo, A., Mechanistic study of droplets coalescence in Pickering emulsions. *Soft Matter* **2012**, *8* (37), 9533-9538.
- 116) Sicard, F.; Striolo, A., Buckling in armored droplets. *Nanoscale* **2017**, *9* (25), 8567-8572.
- 117) Yang, Z.; Xin-Ping, L.; Qing-Xuan, Z., Dissipative particle dynamics studies on the interface of incompatible A/B homopolymer blends in the presence of nanorods. *Polymer* **2011**, *52* (26), 6110-6116.
- 118) Dong, F.-L.; Li, Y.; Zhang, P., Mesoscopic simulation study on the orientation of surfactants adsorbed at the liquid/liquid interface. *Chemical physics letters* **2004**, *399* (1-3), 215-219.
- 119) Groot, R. D.; Rabone, K., Mesoscopic simulation of cell membrane damage, morphology change and rupture by nonionic surfactants. *Biophysical journal* **2001**, *81* (2), 725-736.
- 120) Prinsen, P.; Warren, P.; Michels, M., Mesoscale simulations of surfactant dissolution and mesophase formation. *Physical Review Letters* **2002**, *89* (14), 148302.
- 121) Shi-Ling, Y.; Zheng-Ting, C.; Gui-Ying, X., Mesoscopic simulation of aggregates in surfactant/oil/water systems. *Chinese Journal of Chemistry* **2003**, *21* (2), 112-116.
- 122) Suttipong, M.; Grady, B. P.; Striolo, A., Surfactants adsorption on crossing stripes and steps. *Soft Matter* **2017**, *13* (4), 862-874.
- 123) AlSunaidi, A.; den Otter, W. K.; Clarke, J., Liquid-crystalline ordering in rod-coil diblock copolymers studied by mesoscale simulations. *Philosophical Transactions - Royal Society of London Series A Mathematical Physical and Engineering Sciences* **2004**, *362*, 1773-1782.
- 124) Espanol, P.; Warren, P. B., Perspective: Dissipative particle dynamics. *The Journal of Chemical Physics* **2017**, *146* (15), 150901.
- 125) Espanol, P.; Warren, P., Statistical mechanics of dissipative particle dynamics. *EPL (Europhysics Letters)* **1995**, *30* (4), 191.
- 126) Groot, R. D.; Warren, P. B., Dissipative particle dynamics: Bridging the gap between atomistic and mesoscopic simulation. *The Journal of Chemical Physics* **1997**, *107* (11), 4423-4435.
- 127) Andersen, H. C., Rattle: A "velocity" version of the shake algorithm for molecular dynamics calculations. *Journal of Computational Physics* **1983**, *52* (1), 24-34.
- 128) Plimpton, S., Fast parallel algorithms for short-range molecular dynamics. *Journal of Computational Physics* **1995**, *117* (1), 1-19.
- 129) Stukowski, A., Visualization and analysis of atomistic simulation data with OVITO—the Open Visualization Tool. *Modelling & Simulation in Materials Science & Engineering* **2009**, *18* (1), 015012.
- 130) Humphrey, W.; Dalke, A.; Schulten, K., VMD: visual molecular dynamics. *Journal of molecular graphics* **1996**, *14* (1), 33-38.
- 131) Fan, H.; Striolo, A., Nanoparticle effects on the water-oil interfacial tension. *Physical Review E* **2012**, *86* (5), 051610.

- 132) Khedr, A.; Striolo, A., Self-assembly of mono-and poly-dispersed nanoparticles on emulsion droplets: antagonistic vs. synergistic effects as a function of particle size. *Physical Chemistry Chemical Physics* **2020**, *22* (39), 22662-22673.
- 133) Jerome, B., Surface effects and anchoring in liquid crystals. *Reports on Progress in Physics* **1991**, *54* (3), 391.
- 134) Greschek, M.; Melle, M.; Schoen, M., Isotropic–nematic phase transitions in confined mesogenic fluids. The role of substrate anchoring. *Soft Matter* **2010**, *6* (9), 1898-1909.
- 135) Willman, E. J. Three dimensional finite element modelling of liquid crystal electro-hydrodynamics. University College London, 2009.
- 136) James, R.; Willman, E.; Fernandez, F.; Day, S. E., Finite-element modeling of liquid-crystal hydrodynamics with a variable degree of order. *IEEE Transactions on Electron Devices* **2006**, *53* (7), 1575-1582.
- 137) Willman, E.; Fernández, F. A.; James, R.; Day, S. E., Modeling of weak anisotropic anchoring of nematic liquid crystals in the Landau–de Gennes theory. *IEEE Transactions on Electron Devices* **2007**, *54* (10), 2630-2637.
- 138) Mottram, N. J.; Newton, C. J., Introduction to Q-tensor theory. *arXiv preprint arXiv:1409.3542*. **2014**.
- 139) Willman, E.; Seddon, L.; Osman, M.; Bulak, A.; James, R.; Day, S.; Fernandez, F., Liquid crystal alignment induced by micron-scale patterned surfaces. *Physical Review E* **2014**, *89* (5), 052501.
- 140) Toledano, P.; Toledano, J.-c., *Landau Theory Of Phase Transitions, The: Application To Structural, Incommensurate, Magnetic And Liquid Crystal Systems*. World Scientific Publishing Company: 1987; Vol. 3.
- 141) de Gennes, P. G., An analogy between superconductors and smectics A. *Solid State Communications* **1972**, *10* (9), 753-756.
- 142) Mori, H.; Gartland Jr, E. C.; Kelly, J. R.; Bos, P. J., Multidimensional director modeling using the Q tensor representation in a liquid crystal cell and its application to the π cell with patterned electrodes. *Japanese journal of applied physics* **1999**, *38* (1R), 135.
- 143) Lopez-Leon, T.; Fernandez-Nieves, A., Drops and shells of liquid crystal. *Colloid and Polymer Science* **2011**, *289* (4), 345-359.
- 144) Mahajan, M. P., Liquid crystal bridges. *Liquid crystals* **1999**, *26* (3), 443-448.
- 145) Gupta, J. K.; Abbott, N. L., Principles for manipulation of the lateral organization of aqueous-soluble surface-active molecules at the liquid crystal– aqueous interface. *Langmuir* **2009**, *25* (4), 2026-2033.
- 146) Binnemans, K., Ionic liquid crystals. *Chemical Reviews* **2005**, *105* (11), 4148-4204.
- 147) Faul, C. F.; Antonietti, M., Ionic self-assembly: Facile synthesis of supramolecular materials. *Advanced Materials* **2003**, *15* (9), 673-683.
- 148) Zhang, Z.; Guo, H., The phase behavior, structure, and dynamics of rodlike mesogens with various flexibility using dissipative particle dynamics simulation. *The Journal of chemical physics* **2010**, *133* (14), 144911.
- 149) Zhao, T.; Wang, X., Phase behavior of lyotropic rigid-chain polymer liquid crystal studied by dissipative particle dynamics. *The Journal of chemical physics* **2011**, *135* (24), 244901.
- 150) Sumer, Z.; Striolo, A., Manipulating molecular order in nematic liquid crystal capillary bridges via surfactant adsorption: guiding principles from dissipative particle dynamics simulations. *Physical Chemistry Chemical Physics* **2018**, *20* (48), 30514-30524.
- 151) Striolo, A.; Prausnitz, J. M.; Bertuccio, A., Osmotic second virial coefficient, intrinsic viscosity and molecular simulation for star and linear polystyrenes. *Macromolecules* **2000**, *33* (26), 9583-9586.
- 152) Rudnick, J.; Gaspari, G., The asphericity of random walks. *Journal of Physics A: Mathematical and General* **1986**, *19* (4), L191.
- 153) Espanol, P.; Warren, P., Statistical mechanics of dissipative particle dynamics. *Europhysics Letters* **1995**, *30* (4), 191.
- 154) Lavrentovich, O. D., Topological defects in dispersed words and worlds around liquid crystals, or liquid crystal drops. *Liquid crystals* **1998**, *24* (1), 117-126.
- 155) Sumer, Z.; Striolo, A., Effects of droplet size and surfactants on anchoring in liquid crystal nanodroplets. *Soft Matter* **2019**, *15* (19), 3914-3922.
- 156) Sumer, Z.; Striolo, A., Nanoparticles shape-specific emergent behaviour on liquid crystal droplets. *Molecular Systems Design & Engineering* **2020**, *5* (2), 449-460.
- 157) Tribello, G. A.; Bonomi, M.; Branduardi, D.; Camilloni, C.; Bussi, G., PLUMED 2: New feathers for an old bird. *Computer Physics Communications* **2014**, *185* (2), 604-613.
- 158) Petukhov, A. V.; Tuinier, R.; Vroege, G. J., Entropic patchiness: Effects of colloid shape and depletion. *Current opinion in colloid & interface science* **2017**, *30*, 54-61.
- 159) Manoharan, V. N., Colloidal matter: Packing, geometry, and entropy. *Science* **2015**, *349* (6251).

- 160) Avendaño, C.; Escobedo, F. A., Packing, entropic patchiness, and self-assembly of non-convex colloidal particles: A simulation perspective. *Current Opinion in Colloid & Interface Science* **2017**, *30*, 62-69.
- 161) Damasceno, P. F.; Engel, M.; Glotzer, S. C., Crystalline assemblies and densest packings of a family of truncated tetrahedra and the role of directional entropic forces. *ACS Nano* **2012**, *6* (1), 609-614.
- 162) Jana, N. R., Shape Effect in Nanoparticle Self-Assembly. *Angewandte Chemie International Edition* **2004**, *43* (12), 1536-1540.
- 163) Škarabot, M.; Muševič, I., Direct observation of interaction of nanoparticles in a nematic liquid crystal. *Soft Matter* **2010**, *6* (21), 5476-5481.
- 164) Lewandowski, E. P.; Cavallaro Jr, M.; Botto, L.; Bernate, J. C.; Garbin, V.; Stebe, K. J., Orientation and self-assembly of cylindrical particles by anisotropic capillary interactions. *Langmuir* **2010**, *26* (19), 15142-15154.
- 165) Bi, C.; Wang, S.; Kershaw, S. V.; Zheng, K.; Pullerits, T.; Gaponenko, S.; Tian, J.; Rogach, A. L., Spontaneous Self-Assembly of Cesium Lead Halide Perovskite Nanoplatelets into Cuboid Crystals with High Intensity Blue Emission. *Advanced Science* **2019**, 1900462.
- 166) Damasceno, P. F.; Engel, M.; Glotzer, S. C., Crystalline assemblies and densest packings of a family of truncated tetrahedra and the role of directional entropic forces. *ACS Nano* **2011**, *6* (1), 609-614.
- 167) Rofouie, P.; Pasini, D.; Rey, A. D., Morphology of elastic nematic liquid crystal membranes. *Soft matter* **2017**, *13* (32), 5366-5380.
- 168) Wang, D.; Park, S.-Y.; Kang, I.-K., Liquid crystals: emerging materials for use in real-time detection applications. *Journal of Materials Chemistry C* **2015**, *3* (35), 9038-9047.
- 169) Volovik, G.; Lavrentovich, O., Topological dynamics of defects: boojums in nematic drops. *Zh Eksp Teor Fiz* **1983**, *85* (6), 1997-2010.
- 170) Schopohl, N.; Sluckin, T., Hedgehog structure in nematic and magnetic systems. *Journal de Physique* **1988**, *49* (7), 1097-1101.
- 171) Gartland Jr, E.; Mkaddem, S., Instability of radial hedgehog configurations in nematic liquid crystals under Landau–de Gennes free-energy models. *Physical Review E* **1999**, *59* (1), 563.
- 172) Guzman, O.; Abbott, N. L.; de Pablo, J. J., Quenched disorder in a liquid-crystal biosensor: Adsorbed nanoparticles at confining walls. *The Journal of Chemical Physics* **2005**, *122* (18), 184711.
- 173) Lee, G.-d.; Bos, P. J.; Ahn, S. H.; Kim, K. H., Fast Q-tensor method for modeling the dynamics of defects in a liquid crystal director field. *Physical Review E* **2003**, *67* (4), 041715.
- 174) Wincure, B. M.; Rey, A. D., Nanoscale analysis of defect shedding from liquid crystal interfaces. *Nano Letters* **2007**, *7* (6), 1474-1479.
- 175) Sumer, Z.; Fernandez, A.; Striolo, A., Engineered Liquid Crystal Nano Droplets: Insights from Multi-Scale Simulations. *Nanoscale* **2020**, *12*, 20211-20219.
- 176) Feng, W.; Sun, L.-D.; Yan, C.-H., Role of surface ligands in the nanoparticle assemblies: a case study of regularly shaped colloidal crystals composed of sodium rare earth fluoride. *Langmuir* **2011**, *27* (7), 3343-3347.
- 177) Rossi, L. M.; Fiorio, J. L.; Garcia, M. A.; Ferraz, C. P., The role and fate of capping ligands in colloidally prepared metal nanoparticle catalysts. *Dalton Transactions* **2018**, *47* (17), 5889-5915.
- 178) Taddese, T.; Anderson, R. L.; Bray, D. J.; Warren, P. B., Recent advances in particle-based simulation of surfactants. *Current Opinion in Colloid Interface Science* **2020**.
- 179) Warren, P. B., Hydrodynamic bubble coarsening in off-critical vapor-liquid phase separation. *Physical Review Letters* **2001**, *87* (22), 225702.
- 180) Marrink, S. J.; Risselada, H. J.; Yefimov, S.; Tieleman, D. P.; De Vries, A. H., The MARTINI force field: coarse grained model for biomolecular simulations. *The journal of physical chemistry B* **2007**, *111* (27), 7812-7824.